Coincidence Electroproduction of Charged Pions and the Pion Form Factor*†

C. N. Brown, C. R. Canizares,‡ W. E. Cooper,§ A. M. Eisner,|| G. J. Feldman,** C. A. Lichtenstein, L. Litt††, W. Lockeretz‡‡, V. B. Montana,§§ and F. M. Pipkin
Cyclotron Laboratory, Harvard University, Cambridge, Massachusetts 02138
(Received 15 January 1973)

We report measurements of the electroproduction reaction $e^- + p \to e^- + \pi^+ + n$ carried out at the Cambridge Electron Accelerator by observing the final electron and pion in coincidence. The apparatus consisted of two focusing magnetic spectrometers equipped with wire spark chambers for determining the trajectories of the particles and with Čerenkov counters for particle identification. Data were collected in three scans which varied in turn one of the three variables: the photon mass squared k^2, the virtual photon-hadron center-of-mass energy W, or the angle θ between the virtual photon and the electroproduced pion in the virtual-photon–hadron center-of-mass system. The k^2-scan central settings were $k^2 = -0.18$, -0.30, -0.40, -0.80, and -1.20 GeV^2 for $W = 2.15$ GeV and $\theta = 0°$; the W-scan central settings were $W = 1.85$, 2.05, 2.15, and 2.50 GeV for $k^2 = -0.30$ GeV^2 and $\theta = 0°$; the central settings for the θ scan were $\theta = 0°$, 7°, and 15° for $\phi = 0°$ and 180° and for $k^2 = -0.40$ GeV^2 and $W = 2.15$ GeV. The data are analyzed to determine the longitudinal-transverse interference term and are compared with the predictions of a dispersion-theory calculation by Berends. The dispersion-theory model is used to extract the pion electromagnetic form factor. The result is consistent with $F_\pi = F_1^V$, but a simple ρ-pole form factor cannot be ruled out.

I. INTRODUCTION

One of the most interesting aspects of electroproduction is that it can be used to measure photoproduction amplitudes as functions of the mass of the photon. This degree of freedom is not accessible to hadron-induced reactions. It is partially the weakness of the electromagnetic interaction that makes it possible to treat electron-induced reactions in the one-photon-exchange approximation as virtual photoproduction by spacelike photons. The electroproduction reactions can be described in terms of form factors which are generalizations of the form factors observed in elastic electron-proton scattering or in terms of cross sections which are extensions of the photoproduction cross sections.

The most extensive study of electroproduction has been made by the SLAC-MIT group.[1] They measured the total virtual-photoproduction cross sections for both neutrons and protons as a function of energy and photon mass. They found that the cross section remains surprisingly large as the photon becomes massive, and that when properly expressed the cross section scales and becomes a universal function of the ratio of the virtual-photon laboratory energy to its mass squared. The magnitude of the cross section suggests that the interior of the proton contains pointlike objects; the scaling suggests that there is no fundamental unit of mass. There is no real understanding of this phenomenon.[2] Coincidence electroproduction extends these studies to specific virtual-photoproduction channels.[3]

One particularly interesting reaction is single-pion electroproduction

$$e^- + p \to e^- + \pi^+ + n\,.$$

This reaction is the generalization to electroproduction of the photoproduction reaction

$$\gamma + p \to \pi^+ + n\,.$$

It was suggested many years ago that measurements of this process could be used to determine the pion form factor.[4] This possibility rests on the assumption that there is a large contribution from the one-pion-exchange diagram. The forward peak observed in photoproduction indicates that there is a large contribution from this diagram and thus leads one to expect such a contribution in electroproduction.[5-7]

Pion electroproduction was studied by a Cornell group[8] and a Harvard group[9] in an effort to measure the pion form factor. They worked in the energy region where the cross section is dominated by the first pion-nucleon resonance. The pion form factor enters mainly through the interference between the pion-pole diagram and the dominant resonance amplitude. Both groups made a determination of the form factor but the results were very dependent upon the theory used to analyze the data.[10-14]

In this paper we report a study of single-pion electroproduction in the energy range above the pion-nucleon resonances. We describe in succession the electroproduction kinematics and phenomenology, the scope of the experiment, theoretical ideas concerning the process studied, the

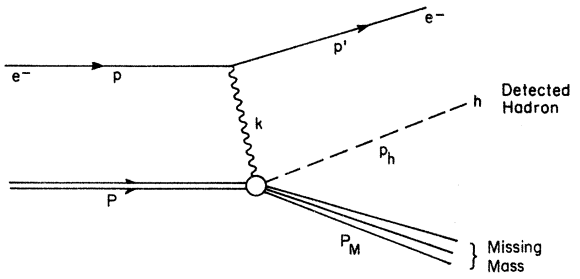

FIG. 1. The assumed dominant diagram for the description of the reaction $e^- + p \rightarrow e^- + \pi^+ + M_M$.

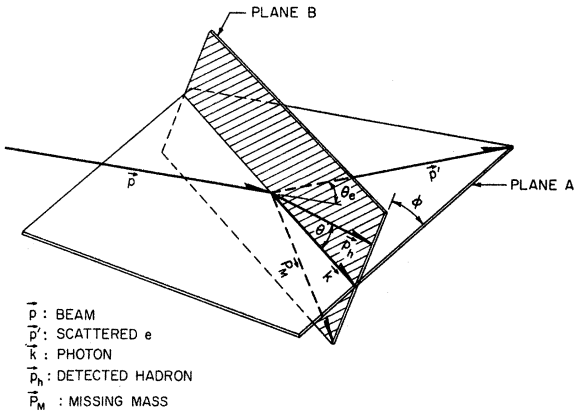

FIG. 2. A diagram showing the laboratory kinematic variables and reaction planes for description of the reaction $e^- + p \rightarrow e^- + \pi^+ + M_M$.

apparatus, the data-taking procedure, the data-reduction procedure and the results of the experiment. This paper is a more complete account of data reported earlier.[15,16] In the period since this work was first reported, measurements in a similar kinematic region have been reported by a DESY group[17] and a Manchester-Lancaster group.[18,19] Independent analyses of the data to determine the pion form factor have been reported by Berends and Gastmans,[20] Devenish and Lyth,[21] and Schmidt.[22]

II. KINEMATICS AND PHENOMENOLOGY

The conventional diagram of the electroproduction reaction

$$e^- + p \rightarrow e^- + h + M_M \tag{1}$$

is shown in Fig. 1. This diagram assumes that the one-photon-exchange approximation is valid. In this approximation electroproduction can be treated as virtual photoproduction by a spacelike photon whose mass, energy, direction, and polarization density matrix are tagged by the scattered electron.[23-25] To describe the virtual photoproduction, we will use a right-handed coordinate system with the 3 axis along the direction of the virtual photon, the 2 axis perpendicular to the electron scattering plane, and the 1 axis in the electron scattering plane pointing from the virtual-photon direction to the direction of the scattered electron. Figures 1 and 2 together with Table I summarize the notation that will be used to describe reaction (1). We will use a metric such that

$$p^2 = p_0{}^2 - \vec{p}\cdot\vec{p} = m_e{}^2 . \tag{2}$$

The virtual photon is characterized by its mass squared

$$k^2 = (p - p')^2 \tag{3a}$$

which in the approximation where the electron mass is neglected is given by

$$k^2 = -4EE'\sin^2(\tfrac{1}{2}\theta_e) \tag{3b}$$

and an invariant equal to the laboratory energy of the virtual photon

$$\nu = \frac{k\cdot P}{M} = k_0 . \tag{4a}$$

An alternate variable is W, the invariant mass of the virtual-photon–target-proton system.

$$W^2 = k^2 + 2M\nu + M^2 . \tag{4b}$$

Different reactions with the same detected hadron may be distinguished by the missing mass squared

$$(M_M)^2 = (k + P - p_h)^2 . \tag{5}$$

The virtual photon is in general polarized. In addition to two transverse polarization states, there is a third component which can be taken as scalar (with only a time component) or as longitudinal (with only a component along the direction of the virtual photon). We will use the formulation with a scalar component. In the virtual-photon–hadron center-of-momentum system and in the approximation in which the electron mass is neglected the density matrix for the virtual photon is

$$\rho = \begin{bmatrix} \frac{1}{2}(1+\epsilon) & 0 & -\left[\frac{1}{2}\frac{-k^2}{|\vec{k}|_{c.m.}{}^2}\epsilon(1+\epsilon)\right]^{1/2} \\ 0 & \frac{1}{2}(1-\epsilon) & 0 \\ -\left[\frac{1}{2}\frac{-k^2}{|\vec{k}|_{c.m.}{}^2}\epsilon(1+\epsilon)\right]^{1/2} & 0 & \frac{-k^2}{|\vec{k}|_{c.m.}{}^2}\epsilon \end{bmatrix} . \tag{6}$$

TABLE I. Kinematics notation and definitions.

Quantity	Definition
p	Incident electron 4-momentum
p'	Outgoing electron 4-momentum
P	Target nucleon 4-momentum
p_h	Detected hadron 4-momentum
P_M	4-momentum of missing mass
k	Virtual-photon 4-momentum
m_e	Electron mass
M	Nucleon mass
m_h	Detected hadron mass
k^2	Virtual-photon mass-squared
M_M	Missing mass
W	Virtual-photoproduction c.m. energy
s	W^2
ν	$(k \cdot P)/M$
t	Momentum transfer squared of virtual photoproduction
E	Beam energy (lab)
E'	Scattered electron energy (lab)
k_0	Virtual-photon energy (lab)
$\vec{k}$	Virtual-photon 3-momentum (lab unless specified)
E_h	Detected hadron energy (lab unless specified)
$\vec{p}_h$	Detected hadron 3-momentum (lab unless specified)
θ_e	Scattered electron angle (lab)
θ_k	Virtual-photon angle (lab)
θ	Virtual-photoproduction polar angle (c.m. unless specified)
ϕ	Virtual-photoproduction azimuthal angle
Ω_e	Electron solid angle (lab)
Ω_h	Hadron solid angle (c.m. unless specified)
ϵ	Polarization parameter

Here

$$\epsilon = [1 + 2(1 - \nu^2/k^2)\tan^2(\tfrac{1}{2}\theta_e)]^{-1}, \tag{7}$$

and the three basis states are linearly polarized along the 1 axis, linearly polarized along the 2 axis, and scalar. This density matrix is applicable to any experiment in which one averages over electron polarization. As is conventional, it is properly normalized only in the photoproduction limit. Equation (6) shows that the virtual photons are in a mixture of a state with polarization perpendicular to the electron scattering plane and a state which is a coherent superposition of transverse polarization in the electron scattering plane and the scalar polarization.

For a coincidence experiment in which the scattered electron and an electroproduced π^+ are detected, the differential cross section can be expressed as a known electrodynamic factor times a "virtual-photoproduction cross section."

$$\frac{d\sigma}{dE'd\Omega_e d\Omega_\pi} = \Gamma \frac{d\sigma}{d\Omega_\pi} \ . \tag{8}$$

Γ can be interpreted as the number of virtual photons per detected electron and is given by[25]

$$\Gamma = \frac{\alpha}{2\pi^2}\left(\frac{E'}{E}\right)\left(\frac{W^2 - M^2}{2M}\right)\left(\frac{1}{-k^2}\right)\frac{1}{1-\epsilon}. \tag{9}$$

If the density matrix given by Eq. (6) is rewritten in a photon-helicity basis, it is easily seen that the virtual-photoproduction cross section has the

TABLE II. Nominal central settings for the data points. All energies are in GeV; all angles are in degrees; all momenta are in GeV/c. p_h for π^+n is the pion momentum for scattered electrons with the central momentum. p_R is the central momentum for the hadron arm, θ_R is the central angle for the hadron arm.

Points	k^2	W	E	E'	θ_e	θ_h	θ_R	p_h for π^+n	p_R	ϵ	Γ
1	−0.30	2.05	5.716	3.786	6.75	12.81	12.81	1.920	1.728	0.92	0.0169
2	−0.30	1.85	5.470	3.955	6.75	16.78	16.78	1.500	1.500	0.94	0.0213
3a	−0.30	2.15	5.852	3.698	6.75	11.28	11.28	2.145	1.958	0.90	0.0151
3b	−0.30	2.15	5.455	3.301	7.40	11.08	11.03	2.145	1.958	0.88	0.0123
4	−0.18	2.15	4.820	2.730	6.69	8.61	8.61	2.082	1.900	0.86	0.0157
5	−0.30	2.50	5.460	2.439	8.61	6.83	6.83	3.015	2.833	0.75	0.006 00
6	−0.40	2.15	5.460	3.253	8.61	12.24	6.83	2.168	1.979	0.87	0.008 46
7	−0.40	2.15	5.460	3.253	8.61	12.24	12.24	2.195	2.004	0.87	0.008 46
8	−0.40	2.15	5.460	3.253	8.61	12.24	17.65	2.168	1.979	0.87	0.008 46
9	−0.81	2.15	5.460	3.034	12.69	14.94	14.94	2.403	2.194	0.83	0.002 98
10	−0.40	2.15	5.460	3.253	8.61	12.24	9.54	2.188	2.004	0.87	0.008 46
11	−0.40	2.15	5.460	3.253	8.61	12.24	14.94	2.188	2.004	0.87	0.008 46
12	−1.20	2.15	5.460	2.826	16.03	15.88	15.88	2.594	2.368	0.79	0.001 50

form

$$\frac{d\sigma}{d\Omega_\pi} = A(k^2, W, \theta) + B(k^2, W, \theta)\epsilon \cos 2\phi + C(k^2, W, \theta)\epsilon + D(k^2, W, \theta)\left(\frac{\epsilon(1+\epsilon)}{2}\right)^{1/2} \cos\phi. \quad (10)$$

A, B, C, and D are linear combinations of products of virtual-photoproduction helicity amplitudes. The four terms refer respectively to unpolarized transverse production, interference between the two transverse helicity states, purely scalar production and transverse-scalar interference. For small k^2 the terms C and D are proportional to $-k^2$ and $(-k^2)^{1/2}$, respectively, and consequently vanish in the photoproduction limit. Helicity conservation for forward scattering requires that B and D vanish at $\theta = 0$. The first two terms are related to the cross sections for linearly polarized transverse photons through the equations

$$A = \frac{1}{2}\left(\frac{d\sigma_\parallel}{d\Omega_\pi} + \frac{d\sigma_\perp}{d\Omega_\pi}\right), \quad (11)$$

$$B = \frac{1}{2}\left(\frac{d\sigma_\parallel}{d\Omega_\pi} - \frac{d\sigma_\perp}{d\Omega_\pi}\right). \quad (12)$$

The subscripts $\parallel$ and $\perp$ signify directions with respect to the virtual-photoproduction plane rather than the electron scattering plane.

III. SCOPE OF THE EXPERIMENT

Data were collected in three scans. In each scan we varied the central setting of the apparatus for one of the three variables, k^2, W, and θ, and kept the remaining two fixed. The k^2 scan consisted of central settings of $k^2 = -0.18$, -0.30, -0.40, -0.80, and -1.20 GeV^2 for $W = 2.15$ GeV and $\theta = 0°$; the W scan central settings were $W = 1.85$, 2.05, 2.15, and 2.50 GeV for $k^2 = -0.30$ GeV^2 and $\theta = 0°$; and the central settings for the θ scan were $\theta = 0°$, 7°, and 15° for $\phi = 0°$ and 180° and for $k^2 = -0.40$ GeV^2 and $W = 2.15$ GeV. A list of data points and the corresponding spectrometer settings are given in Table II.

The apparatus (which will be described in Sec. V) consisted of two focusing spectrometers. Each has a large momentum acceptance ($\approx \pm 30\%$) and a small angular acceptance ($\approx \pm 1°$ vertically and $\approx \pm \frac{1}{2}°$ horizontally). For each setting of the spectrometers, electrons were accepted within a wide range of momentum. Conservation of transverse momentum required then that the virtual photons be emitted over a large angular range and that W, ϵ, θ, and, to a lesser extent, k^2 be highly correlated.

In principle, the four terms of Eq. (10) can be separated experimentally by their characteristic dependence upon ϵ and ϕ. In this experiment ϵ was not varied for any set of k^2, W, and θ settings, so the unpolarized transverse term, A, could not be separated from the scalar term, ϵC. The apparatus was capable of pion detection only near the electron scattering plane. Thus we could measure the scalar-transverse interference term, $[\epsilon(1+\epsilon)/2]^{1/2} D \cos\phi$, which changed sign in the electron scattering plane from one side of the virtual-photon beam to the other. The transverse polarization term, $\epsilon B \cos 2\phi$, was separable only at small values of θ because its measurement required pion detection above or below the electron scattering plane.

The apparatus detected the scattered electron in coincidence with a positive hadron. Thus the general reactions studied were

$$e^- + p \rightarrow e^- + \pi^+ + M_M \tag{13}$$

and

$$e^- + p \rightarrow e^- + p + M_M\,, \tag{14}$$

where M_M represents the missing mass. A limited amount of data was also collected detecting both positively and negatively charged pions from a deuterium target and detecting negatively charged pions from a hydrogen target.[26] This paper will treat only reaction (1) for the special case of the missing particle being a neutron.[27-29]

IV. THE DYNAMICS OF $\pi^+ n$ VIRTUAL PHOTOPRODUCTION

A. Characteristics of Real Photoproduction

The salient features of near-forward $\pi^+ n$ photoproduction at $W \gtrsim 2$ GeV have been frequently described.[5-7] Most conspicuous are the strong forward peak in the region $-t < m_\pi^2$; and the fact that (for $W \gtrsim 2.5$ GeV) $s\,d\sigma/d\Omega$ is approximately independent of s for $-t \lesssim 1.0$ GeV^2. The small-t cross section is qualitatively described by the "generalized Born approximation," consisting of s- and u-channel nucleon poles and the t-channel pion pole. Diagrams for these pole terms resemble those of lowest-order perturbation theory, but must be evaluated with full mass-shell vertex functions. The diagrams are shown in Fig. 3. The generalized Born approximation has the correct energy dependence for $\pi^+ n$ photoproduction.

Engels, Schwiderski, and Schmidt[30] have shown that agreement with the data is improved by including contributions from fixed-t dispersion integrals. A more recent but related approach is the "pseudomodel" of Jackson and Quigg.[31] Utilizing finite-energy sum rules and observed low-energy cross sections, and with no free parameters, they obtain excellent agreement with both unpolarized and polarized photoproduction data. Jackson and Quigg conclude that the low-energy data determine the high-energy behavior without the need for a specific dynamical model. Various Regge models have been proposed for real photoproduction.[5-7] However, they involve many-parameter fits, and there is no reason to suppose that they can be extended to virtual photoproduction.

B. Berends' Fixed-t Dispersion Model

The fixed-t dispersion approach has been extended to virtual photoproduction by Berends.[32] Similar models were later independently proposed by Manweiler and Schmidt[33] and by Devenish and Lyth.[21] The pole terms and subtractions of this model are the simplest gauge-invariant form of the generalized Born approximation.[34] Electromagnetic form factors are used at the photon vertices of the Born terms.

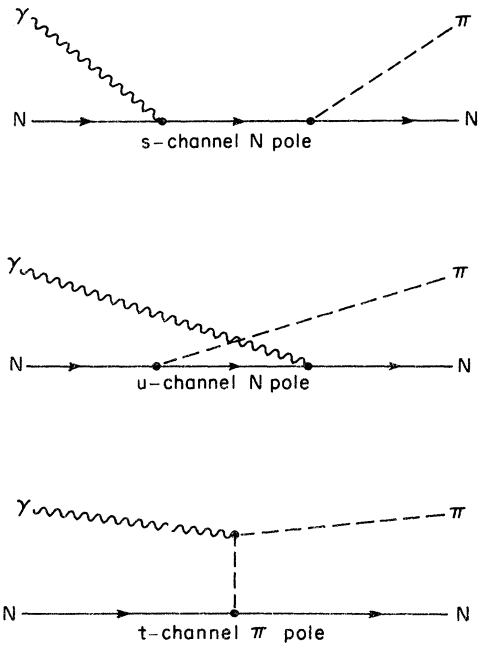

FIG. 3. The Feynman diagrams for the description of real and virtual photoproduction of pions.

The basic assumption of the model is that the imaginary parts of all invariant amplitudes can be ignored above the major resonances. The success of Jackson and Quigg's model supports the validity of this assumption for photoproduction. The Born terms alone are purely real. Only the M_{1+}^3 multipole of the 3-3 resonance is included in the dispersion integrals. No contributions from isoscalar photons are included. Electroproduction data from a deuterium target[26] indicate that such contributions could lead to ≈6% corrections to the cross sections. This gives some justification for leaving out the isoscalar terms. For $-t < 3m_\pi^2$ and $W > 2$ GeV, Berends' model agrees reasonably well with the real photoproduction data of Buschhorn *et al.*[35]

For virtual-photoproduction, the only free parameter in Berends' model is $F_\pi(k^2)$, the charge form factor of the pion. Figure 4 shows the predictions of the model with $F_\pi = F_1^V$ (Ref. 36) for angular distributions at $k^2 = -0.396$ GeV^2 and $W = 2.15$ GeV, the central values for our angular scan. The four terms of Eq. (10) are plotted separately. Figure 5 shows the k^2 dependence of the forward cross section at $W = 2.15$ GeV and $\epsilon = 0.85$. From Eq. (10), this cross section equals $A + C\epsilon$; A and $C\epsilon$ are also plotted separately. The curve showing the transverse cross section (A) predicted from Born terms alone provides a rough

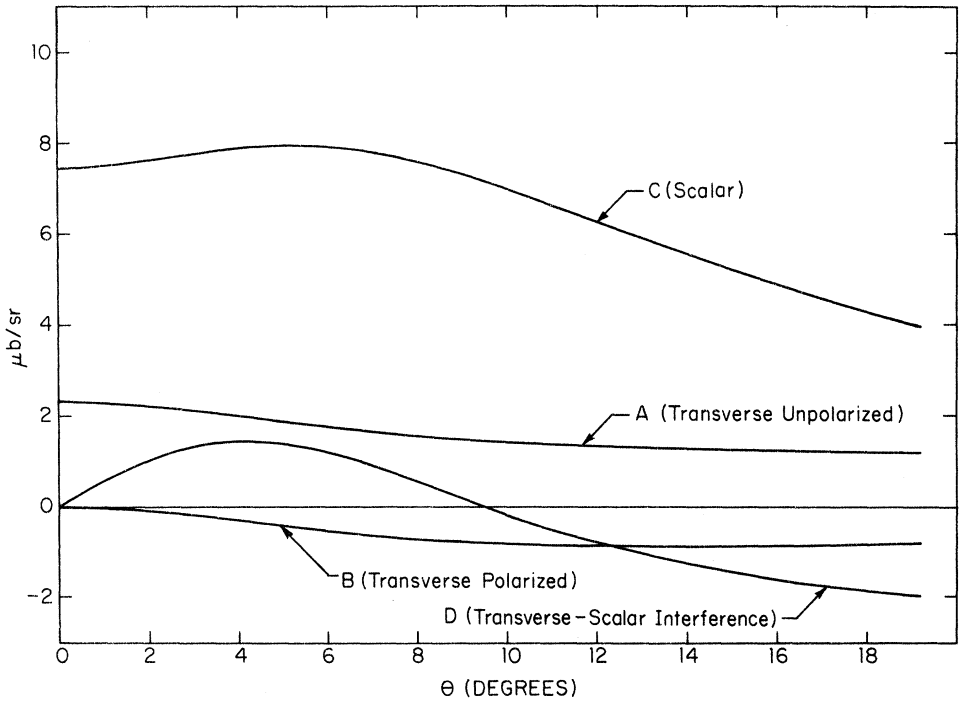

FIG. 4. The predictions of Berends' theory with $F_\pi = F_1^V$ for the components of the virtual-photoproduction cross section $d\sigma/d\Omega_\pi$ for $W = 2.15$ GeV and $k^2 = -0.396$ GeV^2.

indication of the magnitude of dispersion corrections.

The large scalar cross section (C) is due mainly to the Born terms. It is dominated by the pion-pole term, the amplitude of which is proportional to the pion form factor F_π. Thus, if Berends' model is correct, the k^2-scan data provide a way to determine the pion form factor. The scans at fixed k^2 provide tests of the dynamical assumptions of this or any other model. In particular, any such model must successfully fit the angular distributions before a determination of F_π can be believed.

As a test of the sensitivity of the predictions to other multipoles, theoretical estimates of the E_{1+}^3 and S_{1+}^3 multipoles were inserted in the integrals.[37] Cross sections for $\theta = 0°$ typically decreased by ≈5%. For the angular distributions plotted in Fig. 4, $\phi = 0°$ cross sections decreased by ≈7%, while the effect at $\phi = 180°$ tended to be much smaller. Devenish and Lyth[21] made a similar calculation in which they included the higher resonances in a simple way with no scalar couplings (except for the P_{33}) and dipole form factors (except for P_{33}, D_{13}, and F_{15}). They conclude that the higher resonances increase the forward cross section by a small amount (≈7%) which is not a strong function of k^2. The largest effect is that the zero in the scalar-transverse interference term is pushed to larger angles as k^2 increases. All these calculations provide a measure of theoretical uncertainties, assuming the validity of the whole approach. They should not be taken seriously as corrections.

Recently Kellett and Verzegnassi[38] and Dombey and Read[39] have questioned the determination of the pion form factor using the theoretical models

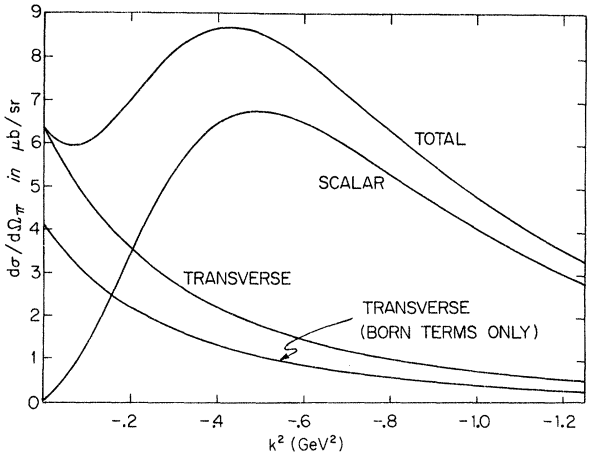

FIG. 5. The predictions of Berends' theory with $F_\pi = F_1^V$ for the scalar and transverse components of the electroproduction cross section for $W = 2.15$ GeV, $\epsilon = 0.85$, $0° \le \theta \le 2.4°$, $0° \le |\phi| \le 180°$ as a function of k^2.

of Berends and Devenish and Lyth. Kellett and Verzegnassi claim that the subtraction constant required in one of the dispersion relations in general involves an unknown function of t and k^2 which introduces an ambiguity in the determination of the pion form factor. Further data and analysis are required to separate out the background function from the pion form factor.

Dombey and Read approach the problem from the standpoint of PCAC (partially conserved axial-vector current) and the current-algebra treatment of pion photoproduction and electroproduction. They claim that the theory in general involves terms depending on the axial-vector form factor and that the Berends and Devenish-Lyth models do not take this into account. In their model also, further data and analysis are required to separate out the pion form factor.

Since our purpose in this paper is to report the data rather than to present a definitive analysis, we have elected to use the simple Berends model which takes into account only the $\Delta(1236)$ in the dispersion relations. A refined theory can be used to correct the simple Berends theory and hence to determine from the results presented here an improved value for the pion form factor.

V. THE APPARATUS

A. General Description

The experiment was performed in an external electron beam at the Cambridge Electron Accelerator (CEA). An over-all view of the experimental layout is shown in Fig. 6. The electron beam entered the experimental hall through a special vacuum system that contained the liquid hydrogen target. The beam emerged from the vacuum system three feet downstream of the target, and then continued mostly through helium, to a Faraday cup. The scattered electron and electroproduced hadron were detected, identified, and momentum analyzed in focusing magnetic spectrometers located on either side of the incident beam. The two spectrometers were essentially mirror images of each other. Each consisted of three magnets—a half-quadrupole, a bending magnet, and a second half-quadrupole—followed by detection equipment. The latter consisted of scintillation counters, wire spark chambers with magnetostrictive readouts, a scintillation counter hodoscope, a threshold Čerenkov counter, and a shower counter.

Two sets of fast electronics were used. The first set, which was located in the experimental hall, provided a trigger for the spark chambers. The second set, which was located in the counting room, generated analog and digital information for each event. The data were logged and processed by an on-line computer system consisting of an XDS-92 and an IBM 360/65.

B. The External Electron Beam

The external electron beam at the CEA [40] was focused on a surveyed mark on a fluorescent

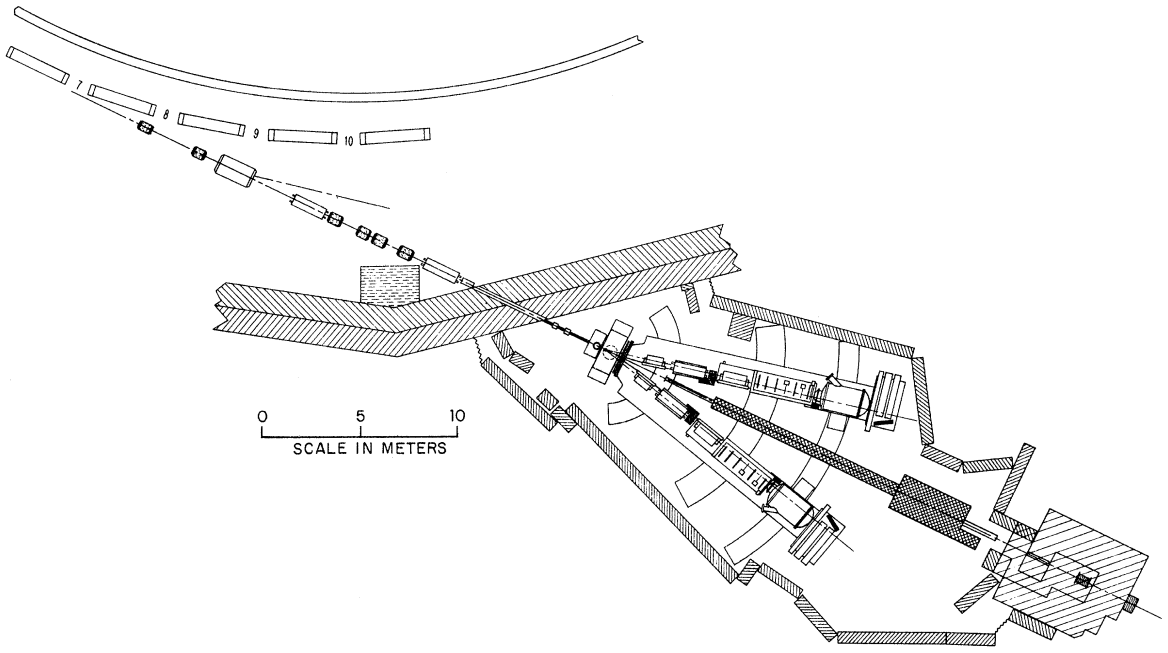

FIG. 6. An over-all view of the experimental layout showing the relationship of the apparatus to the accelerator.

screen located just downstream of the target vacuum chamber. Typical beam spots were 1 cm wide and 1 mm tall. The Faraday cup was located approximately 23 m downstream of the target. A second fluorescent screen was located just in front of the Faraday cup.

The collector of the Faraday cup had a diameter of 22 cm. The beam spot at the Faraday cup was typically a 4-cm-diameter circle. Beam pictures and simple scattering calculations showed that no significant fraction of the beam went uncollected. Minor problems with the Faraday-cup calibration and the operation of the integrator contributed 1.3% and 1%, respectively, to the over-all normalization uncertainty.

The frequency of the accelerating rf and the maximum ring-magnet field were recorded for each data run. The cosine variation of the machine energy within the 600–1000 μsec beam spill was corrected for by recording the field in one of the ring magnets for every event. This magnetic field was measured with a CEA constructed device called the Field Sampling Unit (FSU).

C. Hydrogen Target

The target container consisted of two concentric Mylar cylinders with diameters of 5.1 cm and 6.35 cm. The outer cylinder was capped with 0.094-mm-thick aluminum end windows. Hydrogen entered between the two cylinders and flowed around the inner cylinder in order to reach the used region. This arrangement prevented bubbling. Figure 7 shows the target and surrounding hardware.

The effective target length was determined by measuring the distance between beam marks on the end windows. This was done with a slight excess pressure inside the target; we typically ran with <10.3 torr above 1 atmosphere. The length was 15.9 cm with a $\frac{1}{2}$% uncertainty; this uncertainty allows for possible temperature effects, since the measurement was made at room temperature. For the density of liquid hydrogen, we use the standard value of 0.0708 g/cm^3. The small pressure variations have no significant effect on this number.

D. Spectrometers

1. *The Magnet System*

Each of the spectrometers consisted of three magnets—a horizontally focusing half-quadrupole, a vertically deflecting bending magnet, and a vertically focusing half-quadrupole. The magnets for each spectrometer were located on a movable arm. On each arm an inclined plane supported the detection equipment. Figure 8 is a schematic diagram of a side view of one arm. Each arm could be rotated independently about its own adjustable pivot, which was located beneath the hy-

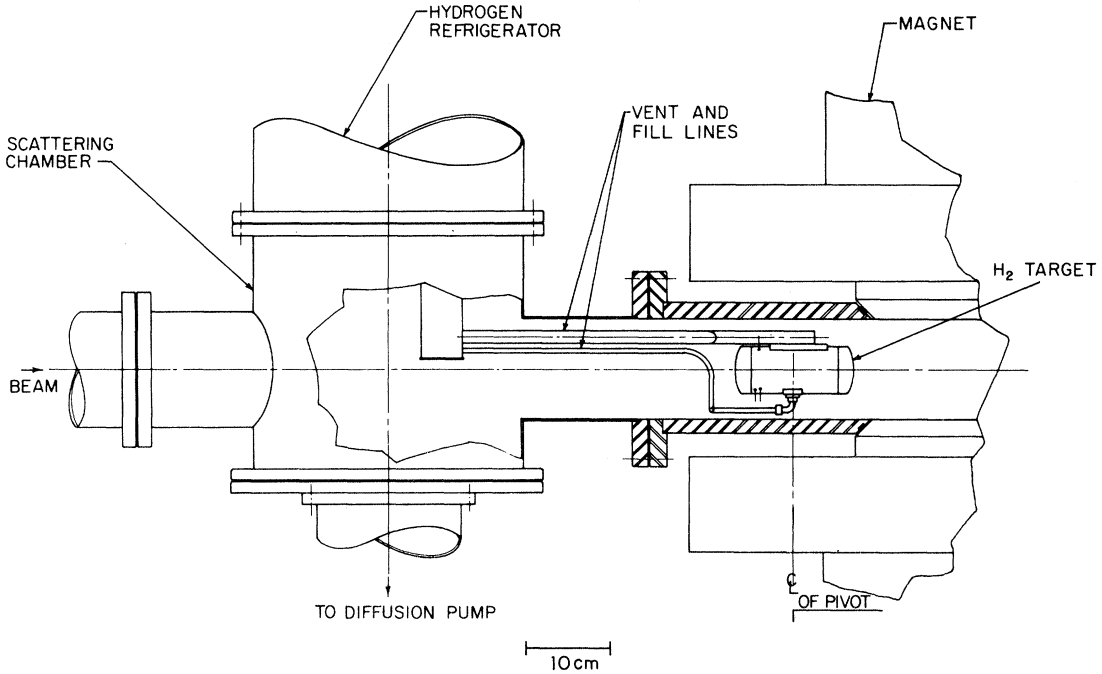

FIG. 7. A diagram of the hydrogen target. The magnet containing the hydrogen target was not used during this experiment and served only to shield the apparatus.

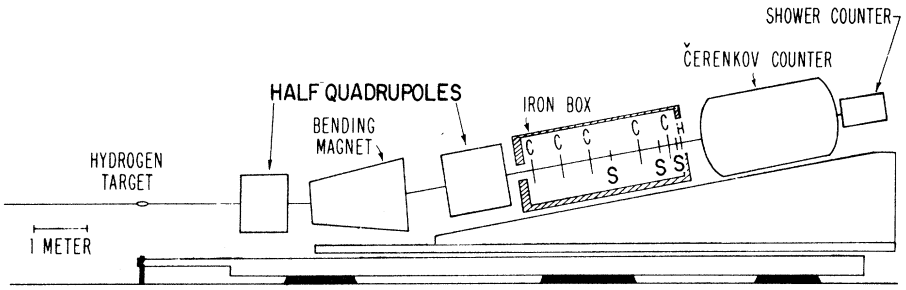

FIG. 8. A schematic diagram showing a side view of the right spectrometer arm. *C* is a spark-chamber module, *S* a scintillator counter, and *H* a scintillation counter hodoscope.

drogen target. Except during testing and calibration, the left arm (looking downstream along the incident beam) was used to analyze the scattered electron and the right arm was used to measure the emergent hadron.

The spectrometers were point to point focusing in the vertical, momentum defining plane and line to point focusing in the horizontal plane. The vertical bend angle for the central momentum rays was 10.4° and the image of the target (momentum focus) for the central momentum was located approximately 2.6 m past the exit of the second quadrupole. The locus of target images for the various momenta was a plane which made an angle of 4.8° relative to the central ray. The momentum dispersion along the locus of images was approximately 0.24%/cm.

The largest contribution to the momentum resolution was multiple scattering. A helium bag ran through all the magnets for each spectrometer, and particles passed through the first three spark chamber modules before meeting the first scintillation counter.

Elastic electron scattering data were used to determine the effective lengths of the magnets as functions of current. Nuclear resonance, Hall probe, and rotating coil techniques were used to determine the magnetization curves.

2. *Scintillation Counters and Spark Chambers*

Immediately following the second quadrupole on each arm was an iron box whose front and beam-side walls were 15 cm thick. This box, which had one wall missing on the side away from the electron beam, contained a long, flat, jig plate on which the spark-chamber modules and scintillation counters were mounted. Coordinate systems were accurately inscribed on each steel jig plate before installation.

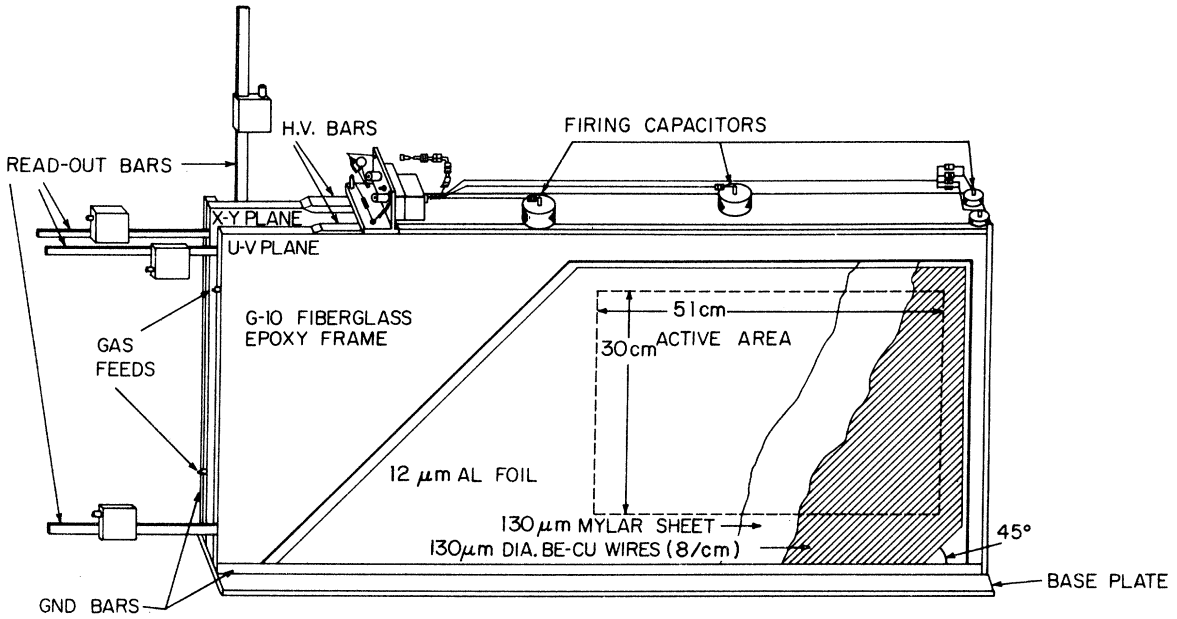

FIG. 9. A drawing showing the construction of a typical spark-chamber module.

Within each shielding box there were five wire spark-chamber modules, three scintillation counters, and a horizontal-angle hodoscope. The arrangement is shown in Fig. 8. An additional scintillation counter in the front of the shielding box was present for data point 1. Each of the scintillation counters was 3-mm-thick Pilot B scintillator. The horizontal hodoscopes were used mainly for eliminating two-track ambiguities that appeared because of the 1-μsec chamber live time. About two-thirds of such otherwise ambiguous events, typically 3–5% of the data, were rescued.

Each spark-chamber module consisted of two high-voltage gaps, one having xy planes and the other having uv planes. The y coordinate was normal to the jig plate; the u and v were rotated from x and y by 45°. Figure 9 shows the assembly of one module. The chambers used magnetostrictive readouts. A pickup coil on the readout wire fed pulses which were typically 4 mV into a dc-coupled amplifier with a gain of about 500. Output signals from the amplifier were processed in the counting room by a data-handling system built by Science Accessories Corporation.

3. Čerenkov Counters

A large threshold Čerenkov counter using Freon 12 (CCl_2F_2) as the radiator was immediately downstream of each shielding box. The electron-arm counter detected electrons and rejected pions; it was set at a pressure of 0.82 atm. The hadron arm counter detected pions and rejected kaons and protons; it was set at a pressure of 6.46 atm. In order to prevent condensation in the hadron-arm counter it was necessary to heat it.

In each tank a large parabolic mirror focused the light onto the 12.7-cm-diameter photocathode of a photomultiplier. The photomultipliers were enclosed in protective vessels with UVT Lucite windows. The electron arm counter used an Amperex 58 AVP; the hadron-arm counter used an Amperex 58 DVP. The temperature and pressure of each tank were monitored in the counting room. The pressure transducers were calibrated with a dead-weight pressure tester.

4. Shower Counter

The last element on each spectrometer arm was a lead sandwich shower counter. The electron arm counter consisted of eight pieces of 1.25-cm-thick scintillator separated by 7 pieces of lead each of which was 0.63 cm thick; the hadron arm counter had the same lead arrangement together with 8 pieces of 2.54-cm-thick UVT Lucite. These shower counters were left over from an earlier experiment and did not cover the full aperture of the spectrometer. They were used primarily for diagnostic studies.

5. Electronics

The trigger counter signals were passively split in the experimental area and sent to two independent sets of electronics. The first set, which was in the experimental area, triggered the spark chambers and gated the area electronics off until the chamber system recovered. The dead time of the spark-chamber trigger was usually set between 60 and 128 msec. The second set of circuitry was located in the counting room and was separated from the apparatus by nearly 200 nsec of cabling. The counting room circuitry independently processed signals from the trigger counters. Figure 10 shows a diagram of the trigger formation logic used in both sets of circuitry.

The floor trigger signal for a pair coincidence (FTRIG) was brought to the counting room and put into coincidence with a corresponding trigger signal (TRIG) that was made in the counting room using high-quality discriminators and coincidence circuits. There was a small dead time in TRIG introduced by gating off the counting room electronics for 6 μsec during the arrival of spark-chamber noise. Unlike FTRIG the counting room electronics was not otherwise gated off during the spark chamber recovery time. Thus the ratio of TRIG to TRIG·FTRIG coincidences could be used

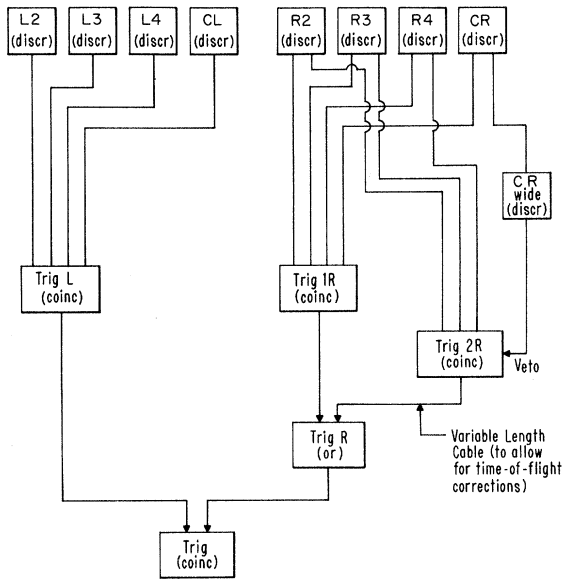

FIG. 10. The counter trigger logic used both in the area and in the counting room. L2 through R4 are scintillation counters; CL and CR are Čerenkov counters.

as a normalization factor to correct for spark-chamber dead time.

The TRIG·FTRIG coincidence was used to trigger the computer interface and initiate the transfer of information to the on-line computer system. For each event we recorded the spark coordinates, the synchrotron magnetic field, the shower-counter pulse heights, the time difference between signals in the first scintillator on each arm and the status of bit gates which contained information on which counters and coincidences had fired. Figure 11 is a diagram of the data-logging system.

VI. DATA-TAKING PROCEDURE

A full survey of each spectrometer arm (including magnet and jig plate positions) was made every time it was moved. For each running period, a beam-monitoring fluorescent screen was also surveyed into position. This screen and a beam spill signal (from a small scintillation counter placed near the beam pipe) were continuously monitored during data taking. Together they provided sensitive indications of any changes in accelerator operating conditions. Glass slides were exposed to obtain a precise measure of the beam size near the focus.

Data taking was organized into "runs" lasting on the order of an hour. For each run, we recorded accelerator parameters, magnet currents, the reading on the Field Sampling Unit for maximum synchrotron magnetic field, and Čerenkov counter temperatures and pressures. Scaler numbers

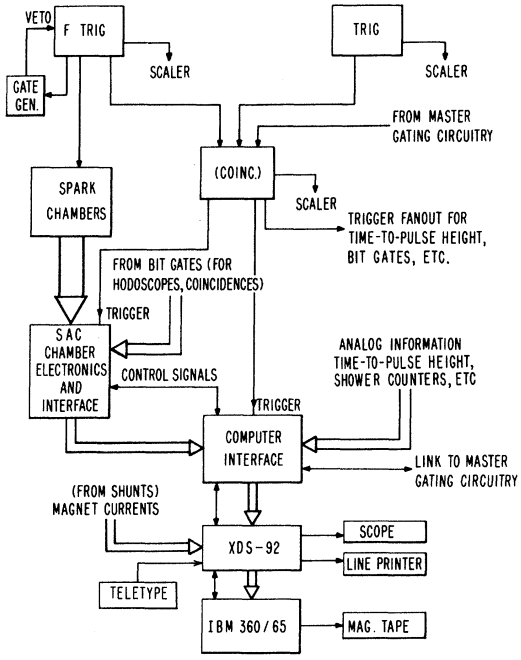

FIG. 11. A simplified logic diagram of the system used to trigger the spark chambers and log the data.

were recorded and photographed at the end of each run; they included all single counter rates, as well as coincidence and several accidental coincidence signals.

Before each running period, important parameters of the electronics were rechecked and, if necessary, adjusted. No significant variations

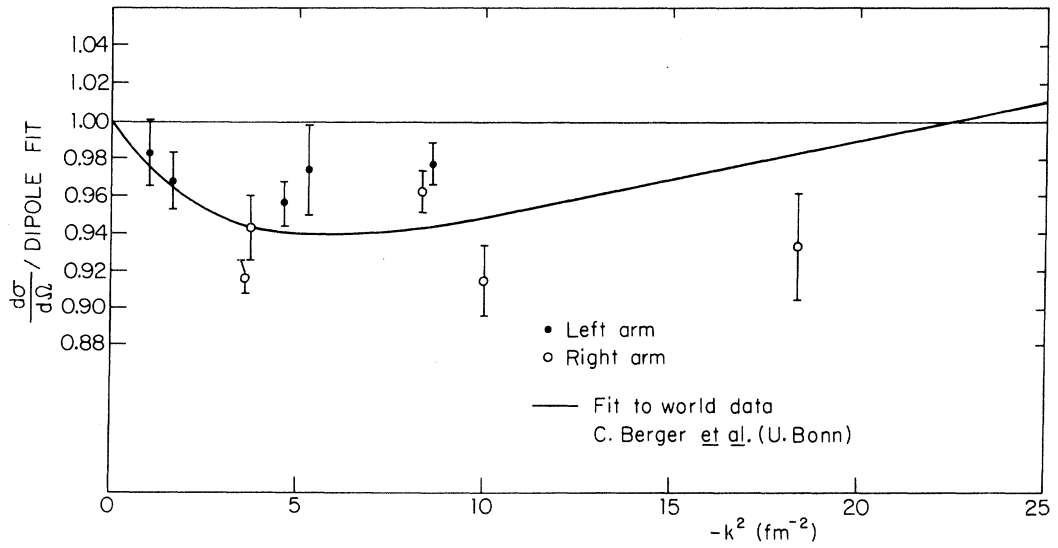

FIG. 12. The ratio of the measured electron scattering cross sections to the dipole fit. Also shown as a solid line is the ratio of the world data to the dipole fit. The errors are the statistical errors. There is, in addition, an estimated systematic error of ± 2%.

occurred. The polarities of all six magnets were checked with a compass. While running, periodic checks were made of counter voltages, helium bag inflation, Faraday-cup pressure, and chamber gas supplies and flow rates.

The on-line program provided time-to-pulse height spectra for electron-hadron arm coincidences, spectra of the beam energy for the coincidence events, and shower-counter spectra; bit-gate summaries; magnet-current readings (and a message immediately indicating any drifts); and an approximate $e\pi$ missing-mass spectrum. Most important, it provided rapid feedback on the operation of the spark chambers. Displays were available of efficiencies, resolution curves, and numbers of second fiducials missed for each chamber plane; the number of sparks per plane and number of lines fit per arm were also histogrammed. Thus problems could be corrected before any data were significantly affected. Moreover, we were able to ensure that the beam intensity was not too high for the chambers to operate efficiently. A second limit on beam intensity was the percentage of arm-to-arm accidental coincidences, which we tried to keep $\lesssim 70\%$ of total triggers. These intensity limits varied between 10^{12} and 2×10^{12} electrons/sec corresponding to circulating beam currents of 7 to 14 mA.

Trigger counters were timed by running delay curves. Voltages were set about 50–100 volts above the plateau knees of counter efficiency curves. Timing counters were set 100 volts still higher in order to reduce time-slewing with pulse height. Plateaus were flat and were checked several times during the experiment.

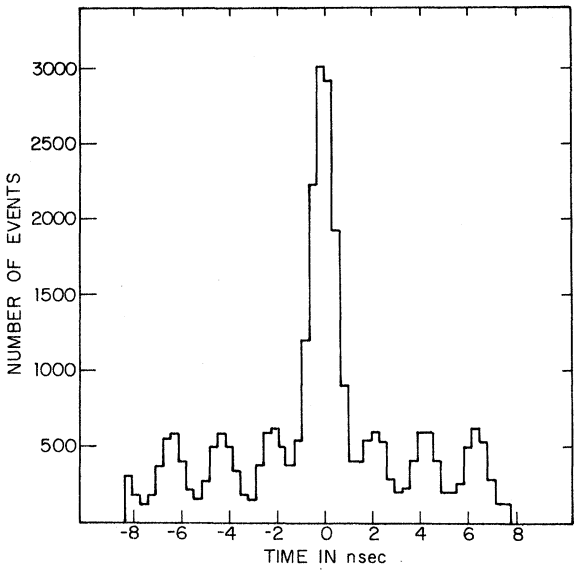

FIG. 13. A typical corrected $e\pi^+$ timing spectrum.

The accelerator duty cycle was monitored during data taking by scaling arm-to-arm accidental coincidences; it was typically 0.02–0.03. Instantaneous rates in the trigger counters were generally 0.2–1.0 MHz. Single-counter accidental rates and dead-time corrections to coincidence rates could be computed from these instantaneous rates (on a run-by-run basis) once the relevant resolving times and dead times were measured.

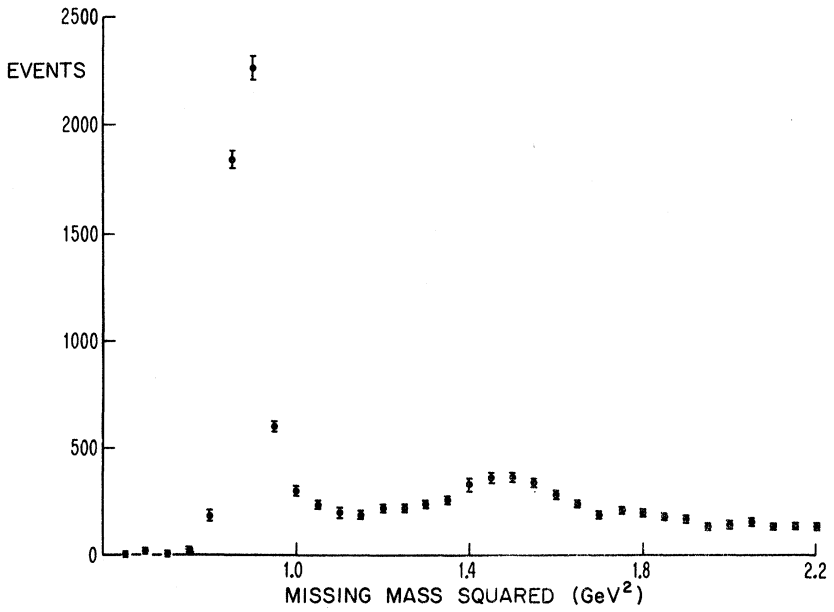

FIG. 14. A typical missing-mass-squared spectrum for the reaction $e^- + p \rightarrow e^- + \pi^+ + M_M$.

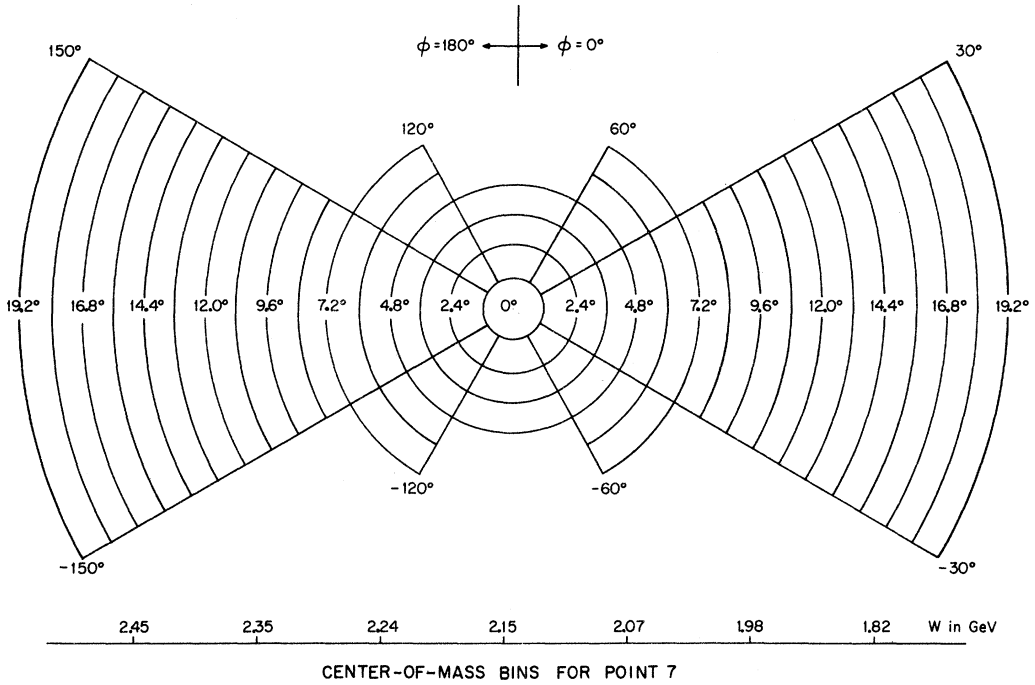

FIG. 15. A diagram showing the center-of-mass angular intervals used to bin the data. Also shown for point 7 is the correlation between center-of-mass angle and the total center-of-mass energy.

The former were measured by scaling selected accidental coincidences. Dead times were determined from a special series of runs at varying beam intensities, and came to 4.0 ± 1.3 nsec for each counter in a single-arm coincidence. Corrections for single-counter accidentals and dead times were usually small (no greater than 2–3%). The far more important arm-to-arm accidentals were treated by the time-to-height analysis described below.

Measurements of the Čerenkov counter efficiencies were made with electron scattering and π^- photoproduction runs. For relativistic electrons the Čerenkov cone angle θ_c in a medium with index of refraction n is approximately $[2(n-1)]^{1/2}$. The cone angle determines the number of photoelectrons emitted by the photocathode, since the number of photons produced is proportional to θ_c^2. In a series of electron scattering runs in which the tank pressure was changed from 0.2 to 1.16 atm, we measured the dependence of the efficiency of the counters on cone angle from 20 mrad to 50 mrad. A series of π photoproduction runs were taken in which the particle momentum and the Čerenkov counter pressure were varied in order to keep θ_c in the range of interest. The pion data were used to verify that the efficiency was a function of cone angle alone and did not depend on the momentum relative to central momentum or on the position of the particle in the aperture.

The index of refraction of Freon 12 has been determined by Hayes *et al.*[41] to be

$$n - 1 = 0.2173d, \tag{15}$$

where d is the density in g/cm^3. Our investigation of the efficiency of the Čerenkov tanks suggested that the index was between 2% and 5% lower. A direct measurement with a refractometer indicated that the constant in Eq. (15) should be lower by 4%. The same measurement technique applied to nitrogen, CO_2, and argon gave the standard values quoted in the literature. A measurement with an interferometer[42] agreed with our results. A calculation based on molar refractivity[43] indicated that the proportionality factor of Eq. (15) should be lower by 6%. Combining these pieces of evidence we feel that the constant in Eq. (15) should be 0.2086 ± 0.0044.

For typical operating conditions (electron arm at 0.82 atm, hadron arm at 6.46 atm) the cone angle was 42 mrad for left-arm electrons and for right-arm pions with a momentum of 1.21 GeV/c. The inefficiency of the counters for these particles was 0.3%. There was, in addition, an inefficiency of (0.2 ± 0.2)% which did not depend upon the cone angle. On the basis of these measurements we set in the data analysis a low-momentum cutoff of

TABLE III. Definition of the bins used to analyze the experiment. All the angles are in the virtual-photon–hadron center-of-mass system and are expressed in degrees.

Bin	θ range	ϕ range	Bin	θ range	ϕ range
1	$0 \le \theta \le 1.2$	all	30	$8.4 \le \theta \le 9.6$	$0 \le \lvert\phi\rvert \le 30$
2	$1.2 \le \theta \le 2.4$	$0 \le \lvert\phi\rvert \le 60$	31		$150 \le \lvert\phi\rvert \le 180$
3		$0 \le \lvert\phi\rvert \le 30$	32	$9.6 \le \theta \le 10.8$	$0 \le \lvert\phi\rvert \le 30$
4		$120 \le \lvert\phi\rvert \le 180$	33		$150 \le \lvert\phi\rvert \le 180$
5		$150 \le \lvert\phi\rvert \le 180$	34	$10.8 \le \theta \le 12.0$	$0 \le \lvert\phi\rvert \le 30$
6		$60 \le \phi \le 120$	35		$150 \le \lvert\phi\rvert \le 180$
7		$-60 \le \phi \le -120$	36	$12.0 \le \theta \le 13.2$	$0 \le \lvert\phi\rvert \le 30$
8	$2.4 \le \theta \le 3.6$	$0 \le \lvert\phi\rvert \le 60$	37		$150 \le \lvert\phi\rvert \le 180$
9		$0 \le \lvert\phi\rvert \le 30$	38	$13.2 \le \theta \le 14.4$	$0 \le \lvert\phi\rvert \le 30$
10		$120 \le \lvert\phi\rvert \le 180$	39		$150 \le \lvert\phi\rvert \le 180$
11		$150 \le \lvert\phi\rvert \le 180$	40	$14.4 \le \theta \le 15.6$	$0 \le \lvert\phi\rvert \le 30$
12		$60 \le \phi \le 120$	41		$150 \le \lvert\phi\rvert \le 180$
13		$-60 \le \phi \le -120$	42	$15.6 \le \theta \le 16.8$	$0 \le \lvert\phi\rvert \le 30$
14	$3.6 \le \theta \le 4.8$	$0 \le \lvert\phi\rvert \le 60$	43		$150 \le \lvert\phi\rvert \le 180$
15		$0 \le \lvert\phi\rvert \le 30$	44	$16.8 \le \theta \le 18.0$	$0 \le \lvert\phi\rvert \le 30$
16		$120 \le \lvert\phi\rvert \le 180$	45		$150 \le \lvert\phi\rvert \le 180$
17		$150 \le \lvert\phi\rvert \le 180$	46	$18.0 \le \theta \le 19.2$	$0 \le \lvert\phi\rvert \le 30$
18		$60 \le \phi \le 120$	47		$150 \le \lvert\phi\rvert \le 180$
19		$-60 \le \phi \le -120$	48	$19.2 \le \theta \le 20.4$	$0 \le \lvert\phi\rvert \le 30$
20	$4.8 \le \theta \le 6.0$	$0 \le \phi \le 60$	49		$150 \le \lvert\phi\rvert \le 180$
21		$0 \le \phi \le 30$	50	$20.4 \le \theta \le 21.6$	$0 \le \lvert\phi\rvert \le 30$
22		$120 \le \lvert\phi\rvert \le 180$	51		$150 \le \lvert\phi\rvert \le 180$
23		$150 \le \lvert\phi\rvert \le 180$	52	$21.6 \le \theta \le 22.8$	$0 \le \lvert\phi\rvert \le 30$
24	$6.0 \le \theta \le 7.2$	$0 \le \lvert\phi\rvert \le 60$	53		$150 \le \lvert\phi\rvert \le 180$
25		$0 \le \lvert\phi\rvert \le 30$	54	$22.8 \le \theta \le 24.0$	$0 \le \lvert\phi\rvert \le 30$
26		$120 \le \lvert\phi\rvert \le 180$	55		$150 \le \lvert\phi\rvert \le 180$
27		$150 \le \lvert\phi\rvert \le 180$	56	$24.0 \le \theta \le 25.2$	$0 \le \lvert\phi\rvert \le 30$
28	$7.2 \le \theta \le 8.4$	$0 \le \lvert\phi\rvert \le 30$	57		$150 \le \lvert\phi\rvert \le 180$
29		$150 \le \lvert\phi\rvert \le 180$			

1.23 GeV/c on the hadron arm to minimize particle misidentification.

VII. DATA REDUCTION

A. Chamber Reconstruction

The spark chambers were not surveyed but were securely clamped in prescribed positions on the jig plate. The chamber frames had accurately milled bottom and outer edges, and the fiducial wires were located with respect to these edges to an accuracy of 0.1 mm. The nominal x and y first fiducial positions were adjusted by not more than 0.25 mm by least-squares fits to real tracks in the chambers, thus minimizing the effect of misalignments and nonlinearities. The knowledge of the x and y fiducials was used to deduce the u and v fiducials.

The chamber-reconstruction algorithm first found lines in each of the four coordinates x, y, u, and v. This was a loose procedure designed to fit as many lines as possible. The line-fitting procedure took all combinations of sparks (scalar readings from a single plane) in the first and fifth chamber modules and connected them with straight lines. For each trial line, the interior modules were searched for sparks within a distance of 5 mm (x and y) or 7 mm (u and v) of the trial line. If any were found, a least-squares fit was made to the three or more sparks and the resulting coordinates of the line were entered in a table of lines. If more than one spark in a chamber was eligible for inclusion in the fit, the one closest to the trial line was used. Once included in one line, a spark was removed from consideration for inclusion in other lines. The whole process was repeated for the five other combinations of exterior modules (first and fourth, second and fifth, first and third, second and fourth, and third and fifth). Up to six lines were tabulated for each coordinate.

These lines were then combined in fours, if possible, or in pairs to form trial three-dimensional "reconstructions." Using trial reconstructions the chamber data were refitted into three-dimensional lines without regard to how the lines were fit originally. A reconstruction was considered to be made if ten or more (out of a possible 20) sparks were found within the 5-mm gate with the

TABLE IV. The corrections applied to entire data points. The percent systematic uncertainties are shown in parentheses below the correction factors.

Data point	1a	1b	2	3a	3b	4	5	6	7	8	9	10	11	12
Chamber dead time [a]	1.138 (1.6)	1.184 (0.8)	1.473 (1.0)	1.475 (1.0)	1.364 (0.9)	1.390 (1.0)	1.155 (1.0)	1.135 (1.0)	1.163 (0.9)	1.080 (0.8)	1.063 (0.8)	1.150 (0.9)	1.109 (0.9)	1.036 (0.7)
Special hardware problems [a] (events lost)	1.027 (0.0)	1.273 (0.0)	1.007 (0.0)	1.000 (0.0)	1.001 (0.0)	1.000 (0.0)	1.000 (0.0)	1.001 (0.0)	1.000 (0.0)	1.008 (0.8)	1.000 (0.0)	1.000 (0.0)	1.000 (0.0)	1.001 (0.0)
Ambiguous events	1.015 (0.0)	1.016 (0.0)	1.046 (0.0)	1.032 (0.0)	1.019 (0.0)	1.022 (0.0)	1.018 (0.0)	1.016 (0.0)	1.019 (0.0)	1.014 (0.0)	1.008 (0.0)	1.016 (0.0)	1.017 (0.0)	1.007 (0.0)
Scintillation counter efficiencies	1.000 (0.4)	1.000 (0.2)	1.000 (0.2)	1.000 (0.2)	1.000 (0.2)	1.000 (0.2)	1.000 (0.2)	1.000 (0.2)	1.000 (0.2)	1.000 (0.2)	1.000 (0.2)	1.000 (0.2)	1.000 (0.2)	1.000 (0.2)
Scintillation counter dead times	1.008 (0.4)	1.011 (0.4)	1.012 (0.4)	1.016 (0.5)	1.012 (0.4)	1.013 (0.4)	1.016 (0.5)	1.011 (0.4)	1.012 (0.4)	1.011 (0.4)	1.013 (0.4)	1.009 (0.3)	1.011 (0.4)	1.010 (0.3)
Chamber efficiencies	1.000 (0.2)	1.001 (0.2)	1.004 (0.2)	1.011 (0.3)	1.002 (0.2)	1.003 (0.2)	1.002 (0.2)	1.001 (0.2)	1.002 (0.2)	1.002 (0.2)	1.000 (0.2)	1.001 (0.2)	1.000 (0.2)	1.000 (0.2)
Integrator calibration	0.985 (1.0)	0.984 (1.0)	0.982 (1.0)	0.982 (1.0)	0.981 (1.0)	0.981 (1.0)	0.980 (1.0)	0.979 (1.0)	0.977 (1.0)	0.979 (1.0)	0.976 (1.0)	0.976 (1.0)	0.976 (1.0)	0.973 (1.0)
Faraday-cup efficiency	1.000 (1.3)	1.000 (1.3)	1.000 (1.3)	1.000 (1.3)	1.000 (1.3)	1.000 (1.3)	1.000 (1.3)	1.000 (1.3)	1.000 (1.3)	1.000 (1.3)	1.000 (1.3)	1.000 (1.3)	1.000 (1.3)	1.000 (1.3)
Target length and density	1.008 (0.5)	1.008 (0.5)	1.008 (0.5)	1.008 (0.5)	1.008 (0.5)	1.008 (0.5)	1.008 (0.5)	1.008 (0.5)	1.008 (0.5)	1.008 (0.5)	1.008 (0.5)	1.008 (0.5)	1.008 (0.5)	1.008 (0.5)
Monte Carlo acceptance	1.000 (0.5)	1.000 (0.5)	1.000 (0.5)	1.000 (0.5)	1.000 (0.5)	1.000 (0.5)	1.000 (0.5)	1.000 (0.5)	1.000 (0.5)	1.000 (0.5)	1.000 (0.5)	1.000 (0.5)	1.000 (0.5)	1.000 (0.5)
Arm-to-arm randoms subtraction	1.000 (0.9)	1.000 (0.2)	1.000 (0.2)	1.000 (0.4)	1.000 (0.3)	1.000 (0.4)	1.000 (0.3)	1.000 (0.4)	1.000 (0.2)	1.000 (0.2)	1.000 (0.2)	1.000 (0.3)	1.000 (0.2)	1.000 (0.4)
Left-arm Čerenkov efficiency	1.005 (0.2)	1.005 (0.2)	1.005 (0.2)	1.005 (0.2)	1.005 (0.2)	1.005 (0.2)	1.005 (0.2)	1.005 (0.2)	1.005 (0.2)	1.005 (0.2)	1.005 (0.2)	1.005 (0.2)	1.005 (0.2)	1.005 (0.2)
Čerenkov counter dead times	1.003 (0.1)	1.004 (0.1)	1.006 (0.2)	1.007 (0.2)	1.006 (0.2)	1.006 (0.2)	1.008 (0.2)	1.006 (0.2)	1.006 (0.2)	1.006 (0.2)	1.007 (0.2)	1.005 (0.2)	1.005 (0.2)	1.006 (0.2)
Absorption losses, no misidentification	1.019 (0.6)	1.019 (0.6)	1.015 (0.5)	1.015 (0.5)	1.015 (0.5)	1.015 (0.5)	1.015 (0.5)	1.015 (0.5)	1.015 (0.5)	1.015 (0.5)	1.015 (0.5)	1.015 (0.5)	1.015 (0.5)	1.015 (0.5)
Enlarged counters	1.000 (0.0)	1.000 (0.0)	1.028 (0.5)	1.022 (0.5)	1.000 (0.0)	1.000 (0.0)	1.000 (0.0)	1.000 (0.0)	1.000 (0.0)	1.000 (0.0)	1.000 (0.0)	1.000 (0.0)	1.000 (0.0)	1.000 (0.0)
Resolution in missing mass	1.009 (0.5)	1.009 (0.5)	1.009 (0.5)	1.009 (0.5)	1.009 (0.5)	1.009 (0.5)	1.009 (0.5)	1.009 (0.5)	1.009 (0.5)	1.009 (0.5)	1.009 (0.5)	1.009 (0.5)	1.009 (0.5)	1.009 (0.5)
Magnet-pole scattering	0.962 (1.9)	0.962 (1.9)	0.960 (2.0)	0.968 (1.6)	0.972 (1.4)	0.972 (1.4)	0.981 (1.0)	0.981 (1.0)	0.970 (1.5)	0.964 (1.8)	0.966 (1.7)	0.978 (1.1)	0.969 (1.5)	0.965 (1.8)
Net correction	1.184 (2.9)	1.534 (1.9)	1.595 (2.0)	1.587 (1.9)	1.404 (1.9)	1.436 (2.0)	1.203 (2.1)	1.171 (2.2)	1.189 (2.3)	1.101 (2.6)	1.069 (2.5)	1.175 (2.1)	1.124 (2.4)	1.034 (2.7)

[a] Both of these categories include small numbers of events lost in the handling.

additional restrictions that both sparks of a chamber had to count for either to be used and that there had to be at least one x-y pair and one u-v pair. Each reconstruction was least-squares-fitted and χ^2 values were calculated for the x and y directions assuming a 0.75-mm resolution. The χ^2 per degree of freedom was typically 1.8; events with χ^2 per degree of freedom greater than 5.0 were not included in the final analysis.

B. Determination of Physical Variables

After reconstruction, each line was intersected with the momentum focal surface to obtain the momentum; and transfer matrices were used to obtain the three target production variables (two angles and a horizontal position). Then the ray was traced forward through the magnet system and the trajectory was checked at the entrance, exit, and interior of each magnet. If the trajectory was beyond any preset limit it was tagged and later rejected.

For the ray tracing, the quadrupoles were considered to have ideal quadrupole fields. The optics were treated exactly in momentum and to first order in geometrical parameters. Ray tracing through the bending magnet was done using the exact formulas for an effective length model of the magnet; the horizontal focusing of the fringe field was included.

Magnetization curves for all six magnets were precisely measured. Effective lengths were determined (as functions of the fields) by requiring that we obtain the correct missing mass and focal surface in single-arm elastic ep scattering measurements made for each spectrometer at momenta centered in the momentum acceptance. The resulting lengths were in agreement with directly measured values. Once these parameters were determined, the accuracy of the entire locus of foci was confirmed by checking the missing-mass peak position for elastic scattering at other momenta within the momentum acceptance.

C. Aperture Definition and Resolution

The aperture of the spectrometers was defined by three conditions on each apparent trajectory: (1) that it passed through the trigger counters, (2) that it passed through relatively aberration-free regions of magnetic field, and (3) that it originated in the target.

The magnetic field aberrations were studied by plotting the apparent missing mass for elastically scattered electrons as a function of the location of the trajectory, and by studying the apparent distributions of particles at magnet entrances and

TABLE V. Values of the bin-dependent corrections for central bins for each data point. The percent systematic uncertainties are listed in parentheses. The bin numbers are explained in Table III.

Data point	1	2	3a	3b	4	5	6	7	8	9	10	11	12
Bin	1	1	1	1	1	1	38	1	39	1	28	29	1
Radiative correction	1.423 (2.0)	1.405 (2.0)	1.431 (2.0)	1.422 (2.0)	1.396 (2.0)	1.437 (2.0)	1.443 (2.0)	1.424 (2.0)	1.405 (2.0)	1.429 (2.0)	1.434 (2.0)	1.414 (2.0)	1.426 (2.0)
Pion decay	1.085 (0.4)	1.109 (0.5)	1.076 (0.4)	1.076 (0.4)	1.078 (0.4)	1.053 (0.3)	1.075 (0.4)	1.074 (0.4)	1.075 (0.4)	1.067 (0.3)	1.075 (0.4)	1.073 (0.4)	1.062 (0.3)
Target empty	0.994 (0.2)	0.994 (0.2)	0.994 (0.2)	0.994 (0.2)	0.995 (0.2)	0.994 (0.2)	0.990 (0.4)	0.994 (0.2)	0.990 (0.4)	0.992 (0.3)	0.993 (0.3)	0.993 (0.3)	0.990 (0.4)
Good events excluded by target cuts	1.006 (0.5)	1.007 (0.5)	1.005 (0.5)	1.006 (0.5)	1.006 (0.5)	1.006 (0.5)	1.007 (0.5)	1.006 (0.5)	1.006 (0.5)	1.006 (0.5)	1.007 (0.5)	1.006 (0.5)	1.006 (0.5)
Pions misidentified as protons	1.023 (0.5)	1.038 (0.8)	1.018 (0.4)	1.018 (0.4)	1.019 (0.4)	1.016 (0.3)	1.018 (0.4)	1.018 (0.4)	1.018 (0.4)	1.016 (0.3)	1.018 (0.4)	1.017 (0.3)	1.015 (0.3)
Pion-pair contamination	0.976 (1.2)	0.990 (0.5)	0.949 (2.5)	0.997 (0.2)	0.986 (0.7)	0.946 (2.5)	0.969 (0.8)	0.999 (0.1)	1.000 (0.0)	1.000 (0.0)	0.998 (0.1)	1.000 (0.0)	1.000 (0.0)
Net correction factor	1.542 (2.1)	1.603 (1.9)	1.486 (2.6)	1.553 (1.9)	1.513 (2.0)	1.454 (2.6)	1.525 (2.0)	1.555 (1.9)	1.531 (1.9)	1.546 (1.9)	1.566 (1.9)	1.541 (1.9	1.531 (1.9)

exits. One criterion for an acceptable aperture was that aberrations did not alter the apparent missing mass by more than the rms resolution. The second criterion was that the particle distributions agreed with those predicted by a Monte Carlo calculation, which included the effect of multiple scattering by using a Gaussian approximation and which then computed apparent momenta and production variables. Multiple scattering was found not to affect significantly the overall spectrometer acceptance.

The momentum resolution was dominated by multiple scattering and the observed values agreed with Monte Carlo predictions. The average rms resolution for good trajectories was 10 MeV/c. The angular resolution was less than 1 mrad.

Cuts were imposed on reconstructed lines at trigger counter locations; the same cuts were used in all Monte Carlo simulations. Cuts on the apparent horizontal target positron were selected so as to exclude less than 1% of the Monte Carlo events.

D. Event-Selection Criteria

An $e\pi^+$ event was required to have fired the Čerenkov counter on the hadron spectrometer and to have one valid trajectory through each spectrometer satisfying the aperture requirements outlined above. Most ambiguities (multitrajectory events) were resolved by discarding any trajectories for which the expected hodoscope counter bit was not set.

E. Acceptance Normalization Check

To test our knowledge of the aperture and other experimental parameters, we measured single-arm elastic electron scattering at several different times during the data taking. Data were col-

TABLE VI. The bins and the center-of-mass virtual-photoproduction cross sections for the reaction $\gamma^* + p \to \pi^+ + n$. The uncertainties are statistical only.

Bins		Kinematic averages							Results	
θ (deg)	ϕ (deg)	θ (deg)	W (GeV)	$-k^2$ (GeV^2)	ϵ	cosϕ	cos2ϕ	$-t$ (GeV^2)	Correction factor	$\frac{d\sigma}{d\Omega_\pi}\left(\frac{\mu b}{sr}\right)$
		(a) That portion of data point 1 taken during one month (1a)								
0.0–1.2	$0 \le \lvert\phi\rvert \le 180$	0.82	2.043	0.289	0.916	0.077	−0.133	0.006	1.825	11.77 ± 2.77
1.2–2.4	$0 \le \lvert\phi\rvert \le 60$	1.92	2.019	0.299	0.921	0.833	0.436	0.008	1.832	11.39 ± 2.82
1.2–2.4	$0 \le \lvert\phi\rvert \le 30$	1.94	2.014	0.301	0.921	0.951	0.812	0.008	1.832	9.36 ± 4.01
1.2–2.4	$120 \le \lvert\phi\rvert \le 180$	1.80	2.075	0.285	0.910	−0.804	0.353	0.006	1.812	9.05 ± 2.75
1.2–2.4	$150 \le \lvert\phi\rvert \le 180$	1.71	2.081	0.284	0.909	−0.954	0.822	0.006	1.814	7.31 ± 3.63
1.2–2.4	$60 \le \phi \le 120$	1.93	2.033	0.285	0.919	0.055	−0.849	0.007	1.826	8.00 ± 3.72
1.2–2.4	$-60 \le \phi \le -120$	1.88	2.057	0.298	0.913	0.017	−0.824	0.007	1.821	6.93 ± 3.11
2.4–3.6	$0 \le \lvert\phi\rvert \le 60$	3.03	1.991	0.292	0.926	0.849	0.486	0.009	1.833	12.66 ± 2.38
2.4–3.6	$0 \le \lvert\phi\rvert \le 30$	3.02	1.985	0.295	0.927	0.961	0.850	0.009	1.834	11.40 ± 3.17
2.4–3.6	$120 \le \lvert\phi\rvert \le 180$	2.90	2.104	0.286	0.903	−0.805	0.346	0.007	1.807	6.14 ± 1.72
2.4–3.6	$150 \le \lvert\phi\rvert \le 180$	2.93	2.116	0.289	0.900	−0.945	0.788	0.007	1.805	7.38 ± 2.36
2.4–3.6	$60 \le \phi \le 120$	3.05	2.042	0.292	0.916	0.143	−0.773	0.008	1.824	11.89 ± 3.36
2.4–3.6	$-60 \le \phi \le -120$	2.97	2.052	0.295	0.914	0.029	−0.847	0.008	1.823	11.44 ± 3.35
3.6–4.8	$0 \le \lvert\phi\rvert \le 60$	4.18	1.980	0.305	0.927	0.841	0.451	0.012	1.841	11.91 ± 2.08
3.6–4.8	$0 \le \lvert\phi\rvert \le 30$	4.20	1.972	0.306	0.929	0.952	0.815	0.012	1.845	12.52 ± 2.73
3.6–4.8	$120 \le \lvert\phi\rvert \le 180$	4.24	2.123	0.277	0.899	−0.844	0.464	0.009	1.800	5.09 ± 1.33
3.6–4.8	$150 \le \lvert\phi\rvert \le 180$	4.30	2.129	0.275	0.898	−0.959	0.841	0.009	1.800	6.05 ± 1.84
3.6–4.8	$60 \le \phi \le 120$	4.19	2.051	0.287	0.915	−0.006	−0.825	0.010	1.822	12.26 ± 3.48
3.6–4.8	$-60 \le \phi \le -120$	4.04	2.058	0.291	0.913	−0.002	−0.797	0.010	1.821	6.79 ± 3.89
4.8–7.2	$0 \le \lvert\phi\rvert \le 60$	4.03	1.943	0.310	0.934	0.894	0.629	0.016	1.856	12.79 ± 1.52
4.8–7.2	$0 \le \lvert\phi\rvert \le 30$	6.07	1.935	0.312	0.935	0.959	0.841	0.016	1.856	12.43 ± 1.84
4.8–7.2	$120 \le \lvert\phi\rvert \le 180$	5.99	2.172	0.273	0.887	−0.902	0.649	0.014	1.792	2.76 ± 0.81
4.8–7.2	$150 \le \lvert\phi\rvert \le 180$	6.03	2.181	0.274	0.885	−0.952	0.818	0.014	1.790	2.08 ± 0.90
7.2–9.6	$0 \le \lvert\phi\rvert \le 30$	8.40	1.894	0.320	0.941	0.968	0.878	0.024	1.870	6.52 ± 1.44
7.2–9.6	$150 \le \lvert\phi\rvert \le 180$	8.28	2.231	0.262	0.872	−0.970	0.885	0.023	1.782	4.74 ± 1.19
9.6–12.0	$0 \le \lvert\phi\rvert \le 30$	10.60	1.851	0.322	0.947	0.975	0.904	0.031	1.886	6.62 ± 1.55
9.6–12.0	$150 \le \lvert\phi\rvert \le 180$	10.43	2.273	0.248	0.860	−0.975	0.902	0.035	1.770	4.39 ± 1.96
12.0–14.4	$0 \le \lvert\phi\rvert \le 30$	13.07	1.808	0.331	0.952	0.988	0.951	0.042	1.899	8.07 ± 1.71

lected on both spectrometers at different energies and angles. The data-reduction technique and corrections were similar to those used for analyzing the electroproduction data. The radiative corrections calculated by Tsai and target bremsstrahlung corrections given by Mo and Tsai [44] were used. We estimate a total possible systematic error of 3%.

Figure 12 shows a plot of the ratio of the electron scattering cross sections to those predicted by the usual dipole fit:

$$G_E = G_M/\mu_p = (1 - q^2/0.71)^{-2}.$$

Figure 12 also shows a similarly expressed fit to the world data for small-angle electron scattering.[45] Compared to this fit our hadron-arm points average about 2% low and our electron-arm points average about $1\frac{1}{2}$% high.

F. Randoms Coincidence Subtraction

Between 50% and 80% of the event triggers were due to accidental coincidences between particles in the two spectrometers. To separate these random coincidences from the true coincidences we made a timing measurement between the farthest upstream counter on each arm. The measurement was corrected for the differential light transit time in the counters and for the differential speed of the particles. The rms resolution was 0.55 nsec, which was sufficient to resolve the 2.1-nsec rf beam structure. Figure 13 shows a typical corrected $e\pi^+$ timing spectrum. Without making any cut on missing mass the data were divided into two sets on the basis of the timing measurement: a "reals" set containing events with less than a 2.1-nsec time-of-flight difference and a "randoms" set containing events with 2.1-

TABLE VI *(Continued)*

Bins		Kinematic averages							Results	
θ (deg)	ϕ (deg)	θ (deg)	W (GeV)	$-k^2$ (GeV^2)	ϵ	cosϕ	cos2ϕ	$-t$ (GeV^2)	Correction factor	$\frac{d\sigma}{d\Omega_\pi}\left(\frac{\mu b}{sr}\right)$
(b) That portion of data point 1 taken during a second month (1b)										
0.0–1.2	$0 \le \lvert\phi\rvert \le 180$	0.82	2.043	0.289	0.916	0.077	−0.133	0.006	2.365	11.65 ± 1.52
1.2–2.4	$0 \le \lvert\phi\rvert \le 60$	1.92	2.019	0.299	0.921	0.833	0.436	0.008	2.374	14.18 ± 1.66
1.2–2.4	$0 \le \lvert\phi\rvert \le 30$	1.94	2.014	0.301	0.921	0.951	0.812	0.008	2.374	14.85 ± 2.40
1.2–2.4	$120 \le \lvert\phi\rvert \le 180$	1.80	2.075	0.285	0.910	−0.804	0.353	0.006	2.348	5.62 ± 1.13
1.2–2.4	$150 \le \lvert\phi\rvert \le 180$	1.71	2.081	0.284	0.909	−0.954	0.822	0.006	2.351	5.76 ± 1.67
1.2–2.4	$60 \le \phi \le 120$	1.93	2.033	0.285	0.919	0.055	−0.849	0.007	2.367	6.84 ± 1.66
1.2–2.4	$-60 \le \phi \le -120$	1.88	2.057	0.298	0.913	0.017	−0.824	0.007	2.360	7.53 ± 1.56
2.4–3.6	$0 \le \lvert\phi\rvert \le 60$	3.03	1.991	0.292	0.926	0.849	0.486	0.009	2.376	11.34 ± 1.17
2.4–3.6	$0 \le \lvert\phi\rvert \le 30$	3.02	1.985	0.295	0.927	0.961	0.850	0.009	2.377	11.94 ± 1.64
2.4–3.6	$120 \le \lvert\phi\rvert \le 180$	2.90	2.104	0.286	0.903	−0.805	0.346	0.007	2.342	6.94 ± 0.94
2.4–3.6	$150 \le \lvert\phi\rvert \le 180$	2.93	2.116	0.289	0.900	−0.945	0.788	0.007	2.339	6.86 ± 1.31
2.4–3.6	$60 \le \phi \le 120$	3.05	2.042	0.292	0.916	0.143	−0.773	0.008	2.364	7.55 ± 1.40
2.4–3.6	$-60 \le \phi \le -120$	2.97	2.052	0.295	0.914	0.029	−0.847	0.008	2.363	8.44 ± 1.70
3.6–4.8	$0 \le \lvert\phi\rvert \le 60$	4.18	1.980	0.305	0.927	0.841	0.451	0.012	2.386	12.01 ± 1.07
3.6–4.8	$0 \le \lvert\phi\rvert \le 30$	4.20	1.972	0.306	0.929	0.952	0.815	0.012	2.392	10.48 ± 1.29
3.6–4.8	$120 \le \lvert\phi\rvert \le 180$	4.24	2.123	0.277	0.899	−0.844	0.464	0.009	2.334	7.87 ± 0.89
3.6–4.8	$150 \le \lvert\phi\rvert \le 180$	4.30	2.129	0.275	0.898	−0.959	0.841	0.009	2.334	7.42 ± 1.17
3.6–4.8	$60 \le \phi \le 120$	4.19	2.051	0.287	0.915	−0.006	−0.825	0.010	2.361	11.34 ± 1.80
3.6–4.8	$-60 \le \phi \le -120$	4.04	2.058	0.291	0.913	−0.002	−0.797	0.010	2.360	9.80 ± 1.98
4.8–7.2	$0 \le \lvert\phi\rvert \le 60$	6.03	1.943	0.310	0.934	0.894	0.629	0.016	2.406	10.88 ± 0.72
4.8–7.2	$0 \le \lvert\phi\rvert \le 30$	6.07	1.935	0.312	0.935	0.959	0.841	0.016	2.406	11.27 ± 0.87
4.8–7.2	$120 \le \lvert\phi\rvert \le 180$	5.99	2.172	0.273	0.887	−0.902	0.649	0.014	2.323	5.28 ± 0.54
4.8–7.2	$150 \le \lvert\phi\rvert \le 180$	6.03	2.181	0.274	0.885	−0.952	0.818	0.014	2.320	5.71 ± 0.65
7.2–9.6	$0 \le \lvert\phi\rvert \le 30$	8.40	1.894	0.320	0.941	0.968	0.878	0.024	2.424	9.80 ± 0.78
7.2–9.6	$150 \le \lvert\phi\rvert \le 180$	8.28	2.231	0.262	0.872	−0.970	0.885	0.023	2.310	3.79 ± 0.53
9.6–12.0	$0 \le \lvert\phi\rvert \le 30$	10.60	1.851	0.322	0.947	0.975	0.904	0.031	2.444	8.19 ± 0.81
9.6–12.0	$150 \le \lvert\phi\rvert \le 180$	10.43	2.273	0.248	0.860	−0.975	0.902	0.035	2.294	3.33 ± 0.85
12.4–14.4	$0 \le \lvert\phi\rvert \le 30$	13.07	1.808	0.331	0.952	0.988	0.951	0.042	2.461	6.90 ± 0.91
14.4–16.8	$0 \le \lvert\phi\rvert \le 30$	15.54	1.764	0.337	0.957	0.993	0.974	0.053	2.490	7.30 ± 1.10
16.8–19.2	$0 \le \lvert\phi\rvert \le 30$	18.22	1.742	0.364	0.958	0.994	0.977	0.069	2.502	4.33 ± 1.35
19.2–21.6	$0 \le \lvert\phi\rvert \le 30$	19.86	1.717	0.365	0.961	0.992	0.967	0.077	2.514	6.09 ± 2.59

to 6.3-nsec time differences. The two sets were analyzed identically. A randoms free spectrum was obtained by subtracting the randoms set weighted by approximately 0.5 from the reals set. Because of time-structure nonuniformities in the beam, the weighting factors differed from 0.5 by up to 10%. They were precisely determined by requiring that after the randoms subtraction was made there were no events left with missing mass squared in the unphysical region $(M_M)^2 < 0.64$ $(\text{GeV})^2$. For the $\pi^+ n$ final state, the typical randoms subtraction was 12%.

G. Missing-Mass Cuts

A typical randoms-subtracted, missing-mass-squared spectrum is shown in Fig. 14. The rms width of the neutron peak is about 0.03 GeV^2, which is what one would expect from the 10-MeV/c-momentum resolution of each of the spectrometers. The $\pi^+ n$ final state was selected by excluding all events further than 0.12 GeV^2 from the neutron mass squared.

H. Kinematic Constraint

Once an event had been determined to be in the $\pi^+ n$ final state, its parameters were over-determined by one measurement. We applied a least-squares adjustment to the magnitudes of the two measured momenta with the constraint that M_M equal the neutron mass. Constraining M_M reduced maximum possible errors in t and θ to ≤ 0.003 $(\text{GeV})^2$ and $\leq 0.6°$, respectively. The precise manner of imposing the constraint (e.g., by a least-squares fit) did not significantly affect any results.

TABLE VI *(Continued)*

Bins		Kinematic averages							Results	
θ (deg)	ϕ (deg)	θ (deg)	W (GeV)	$-k^2$ (GeV^2)	ϵ	$\cos\phi$	$\cos 2\phi$	$-t$ (GeV^2)	Correction factor	$\frac{d\sigma}{d\Omega_\pi}\left(\frac{\mu\text{b}}{\text{sr}}\right)$
				(c) Data point 2						
0.0–1.2	$0 \leq \lvert\phi\rvert \leq 180$	0.81	1.845	0.290	0.944	0.050	0.032	0.010	2.554	10.67 ± 1.43
1.2–2.4	$0 \leq \lvert\phi\rvert \leq 60$	1.85	1.813	0.290	0.949	0.843	0.457	0.011	2.581	13.32 ± 1.63
1.2–2.4	$0 \leq \lvert\phi\rvert \leq 30$	1.85	1.811	0.290	0.949	0.962	0.854	0.012	2.581	12.13 ± 2.17
1.2–2.4	$120 \leq \lvert\phi\rvert \leq 180$	1.84	1.867	0.287	0.941	−0.804	0.346	0.010	2.549	11.83 ± 1.68
1.2–2.4	$150 \leq \lvert\phi\rvert \leq 180$	1.86	1.872	0.286	0.940	−0.956	0.831	0.010	2.547	10.98 ± 2.39
1.2–2.4	$60 \leq \phi \leq 120$	1.93	1.846	0.296	0.943	0.065	−0.844	0.011	2.557	14.14 ± 2.38
1.2–2.4	$-60 \leq \phi \leq -120$	1.89	1.840	0.289	0.945	0.080	−0.811	0.011	2.558	16.52 ± 2.81
2.4–3.6	$0 \leq \lvert\phi\rvert \leq 60$	3.05	1.804	0.298	0.949	0.841	0.456	0.013	2.583	14.51 ± 1.42
2.4–3.6	$0 \leq \lvert\phi\rvert \leq 30$	3.04	1.798	0.299	0.950	0.951	0.811	0.013	2.586	17.06 ± 2.25
2.4–3.6	$120 \leq \lvert\phi\rvert \leq 180$	3.02	1.887	0.285	0.938	−0.819	0.387	0.010	2.531	12.32 ± 1.19
2.4–3.6	$150 \leq \lvert\phi\rvert \leq 180$	3.03	1.891	0.281	0.937	−0.954	0.824	0.010	2.531	11.41 ± 1.59
2.4–3.6	$60 \leq \phi \leq 120$	3.06	1.848	0.292	0.943	−0.016	−0.819	0.012	2.557	11.20 ± 1.71
2.4–3.6	$-60 \leq \phi \leq -120$	3.02	1.848	0.289	0.944	−0.076	−0.835	0.011	2.557	12.40 ± 1.79
3.6–4.8	$0 \leq \lvert\phi\rvert \leq 60$	4.21	1.784	0.293	0.952	0.830	0.423	0.015	2.589	14.34 ± 1.24
3.6–4.8	$0 \leq \lvert\phi\rvert \leq 30$	4.22	1.774	0.295	0.953	0.952	0.817	0.015	2.592	14.33 ± 1.71
3.6–4.8	$120 \leq \lvert\phi\rvert \leq 180$	4.22	1.909	0.283	0.934	−0.840	0.448	0.011	2.523	9.38 ± 0.91
3.6–4.8	$150 \leq \lvert\phi\rvert \leq 180$	4.23	1.916	0.281	0.933	−0.943	0.784	0.011	2.521	10.03 ± 1.36
3.6–4.8	$60 \leq \phi \leq 120$	4.14	1.849	0.295	0.943	0.042	−0.822	0.013	2.557	9.59 ± 1.51
3.6–4.8	$-60 \leq \phi \leq -120$	4.16	1.850	0.290	0.943	−0.055	−0.821	0.013	2.554	14.99 ± 1.86
4.8–7.2	$0 \leq \lvert\phi\rvert \leq 60$	5.98	1.761	0.303	0.955	0.870	0.548	0.019	2.616	14.88 ± 0.89
4.8–7.2	$0 \leq \lvert\phi\rvert \leq 30$	6.04	1.751	0.305	0.956	0.960	0.845	0.019	2.621	14.52 ± 1.15
4.8–7.2	$120 \leq \lvert\phi\rvert \leq 180$	6.00	1.936	0.277	0.930	−0.853	0.491	0.014	2.505	10.07 ± 0.60
4.8–7.2	$150 \leq \lvert\phi\rvert \leq 180$	6.05	1.947	0.276	0.928	−0.952	0.814	0.014	2.500	9.55 ± 0.78
7.2–9.6	$0 \leq \lvert\phi\rvert \leq 30$	8.34	1.721	0.311	0.959	0.957	0.834	0.026	2.647	13.87 ± 1.06
7.2–9.6	$150 \leq \lvert\phi\rvert \leq 180$	8.41	1.992	0.269	0.920	−0.958	0.839	0.021	2.460	7.87 ± 0.62
9.6–12.0	$0 \leq \lvert\phi\rvert \leq 30$	10.43	1.697	0.324	0.967	0.966	0.868	0.033	2.682	12.52 ± 1.39
9.6–12.0	$150 \leq \lvert\phi\rvert \leq 180$	10.68	2.032	0.261	0.912	−0.963	0.859	0.030	2.454	5.99 ± 0.54
12.0–14.4	$0 \leq \lvert\phi\rvert \leq 30$	12.44	1.684	0.340	0.961	0.970	0.881	0.041	2.688	6.42 ± 2.31
12.0–14.4	$150 \leq \lvert\phi\rvert \leq 180$	13.21	2.090	0.253	0.899	−0.979	0.918	0.045	2.431	6.00 ± 0.58
14.4–16.8	$150 \leq \lvert\phi\rvert \leq 180$	15.44	2.133	0.243	0.888	−0.987	0.947	0.062	2.416	3.84 ± 0.63
16.8–19.2	$150 \leq \lvert\phi\rvert \leq 180$	17.70	2.174	0.227	0.878	−0.986	0.946	0.083	2.404	2.24 ± 1.27

I. Determination of Uncorrected Cross Sections

The data were binned in terms of the angles in the virtual-photon–nucleon center-of-mass system. The data were sorted into θ-ϕ bins of 1.2° or 2.4° in θ, and 60° or 120° in ϕ. The size of the ϕ bins was near optimum for the separation of the interference terms B and D of Eq. (10). The θ bins were kept small to minimize the variation of W, k^2, and ϵ within each bin. Figure 15 shows the bins that were used for all the data points and the variation of the center-of-mass energy across the acceptance for data point 7. This correlation between center-of-mass production angle and the center-of-mass energy is typical. Table III gives the detailed identification of the bins.

The Monte Carlo program was used to calculate the electroproduction acceptance and the distributions of events for unit virtual-photoproduction cross sections in the center-of-mass frame. The output of the Monte Carlo program was binned and given a weight factor based on the integrated beam for each data point. The uncorrected cross sections were then calculated by dividing the observed events by the weighted results from the Monte Carlo program.

VIII. CORRECTIONS

A. Over-all Normalization Corrections

Numerous correction factors must be applied to the "cross sections" arrived at above. We shall now describe and tabulate these corrections.

Many of the corrections are entirely independent of the types and properties of the detected particles, and may be applied as over-all normalization factors for each data point. Most such corrections involve events which for one reason or another could not be analyzed. The remainder are related to the beam flux and target factors appearing in counting rate computations.

The largest normalization correction results from the chamber dead-time gate. This is essentially the ratio of scaled defining (counting room)

TABLE VI *(Continued)*

Bins		Kinematic averages							Results	
θ (deg)	ϕ (deg)	θ (deg)	W (GeV)	$-k^2$ (GeV^2)	ϵ	cosϕ	cos2ϕ	$-t$ (GeV^2)	Correction factors	$\frac{d\sigma}{d\Omega_\pi}\left(\frac{\mu b}{sr}\right)$
				(d) Data point 3a						
0.0–1.2	$0 \le \lvert\phi\rvert \le 180$	0.8	2.143	0.290	0.899			0.006	2.358	6.96 ± 0.97
1.2–2.4	$0 \le \lvert\phi\rvert \le 60$	1.9	2.105	0.294	0.907	0.833	0.428	0.007	2.344	13.05 ± 1.36
1.2–2.4	$0 \le \lvert\phi\rvert \le 30$	1.9	2.099	0.292	0.909	0.940	0.770	0.007	2.344	13.69 ± 1.97
1.2–2.4	$120 \le \lvert\phi\rvert \le 180$	1.9	2.179	0.284	0.890	−0.817	0.378	0.006	2.382	8.36 ± 1.10
1.2–2.4	$150 \le \lvert\phi\rvert \le 180$	1.8	2.182	0.284	0.889	−0.954	0.825	0.006	2.382	7.41 ± 1.48
1.2–2.4	$60 \le \lvert\phi\rvert \le 120$	1.9	2.143	0.287	0.899	0.018	−0.827	0.006	2.360	9.60 ± 1.18
2.4–3.6	$0 \le \lvert\phi\rvert \le 60$	3.0	2.086	0.298	0.911	0.855	0.501	0.009	2.348	11.46 ± 0.99
2.4–3.6	$0 \le \lvert\phi\rvert \le 30$	3.1	2.077	0.299	0.913	0.952	0.814	0.009	2.348	12.44 ± 1.39
2.4–3.6	$120 \le \lvert\phi\rvert \le 180$	3.0	2.207	0.279	0.883	−0.831	0.434	0.007	2.398	6.16 ± 0.77
2.4–3.6	$150 \le \lvert\phi\rvert \le 180$	3.0	2.211	0.276	0.882	−0.957	0.834	0.007	2.398	6.86 ± 1.10
2.4–3.6	$60 \le \lvert\phi\rvert \le 120$	3.0	2.152	0.292	0.896	0.011	−0.822	0.008	2.360	9.98 ± 1.04
3.6–4.8	$0 \le \lvert\phi\rvert \le 60$	4.3	2.060	0.305	0.916	0.879	0.581	0.012	2.346	10.63 ± 0.89
3.6–4.8	$0 \le \lvert\phi\rvert \le 30$	4.3	2.053	0.307	0.917	0.966	0.867	0.012	2.346	11.17 ± 1.15
3.6–4.8	$120 \le \lvert\phi\rvert \le 180$	4.2	2.231	0.275	0.877	−0.845	0.468	0.009	2.419	6.10 ± 0.70
3.6–4.8	$150 \le \lvert\phi\rvert \le 180$	4.3	2.247	0.276	0.872	−0.954	0.823	0.009	2.419	5.76 ± 0.87
3.6–4.8	$60 \le \lvert\phi\rvert \le 120$	4.1	2.139	0.293	0.899	0.138	−0.839	0.010	2.360	6.32 ± 0.99
4.8–7.2	$0 \le \lvert\phi\rvert \le 60$	6.0	2.027	0.310	0.922	0.904	0.664	0.016	2.349	11.39 ± 0.66
4.8–7.2	$0 \le \lvert\phi\rvert \le 30$	6.0	2.018	0.312	0.924	0.964	0.862	0.016	2.349	11.67 ± 0.78
4.8–7.2	$120 \le \lvert\phi\rvert \le 180$	5.9	2.272	0.266	0.865	−0.894	0.626	0.014	2.443	5.18 ± 0.46
4.8–7.2	$150 \le \lvert\phi\rvert \le 180$	6.0	2.285	0.265	0.862	−0.960	0.847	0.015	2.443	4.91 ± 0.51
7.2–9.6	$0 \le \lvert\phi\rvert \le 30$	8.3	1.975	0.321	0.931	0.971	0.888	0.024	2.361	9.87 ± 0.73
7.2–9.6	$150 \le \lvert\phi\rvert \le 180$	8.2	2.336	0.248	0.846	−0.964	0.860	0.024	2.434	3.46 ± 0.46
9.6–12.0	$0 \le \lvert\phi\rvert \le 30$	10.7	1.927	0.332	0.938	0.985	0.941	0.034	2.367	7.48 ± 0.73
9.6–12.0	$150 \le \lvert\phi\rvert \le 180$	10.6	2.392	0.236	0.828	−0.973	0.895	0.040	2.421	3.66 ± 0.68
12.0–14.4	$0 \le \lvert\phi\rvert \le 30$	13.0	1.878	0.334	0.945	0.990	0.962	0.044	2.377	4.78 ± 0.78
14.4–16.8	$0 \le \lvert\phi\rvert \le 30$	15.5	1.835	0.342	0.950	0.994	0.976	0.056	2.390	5.88 ± 1.03
16.8–19.2	$0 \le \lvert\phi\rvert \le 30$	17.7	1.807	0.362	0.953	0.995	0.982	0.069	2.405	5.65 ± 1.52

TABLE VI *(Continued)*

Bins		Kinematic Averages							Results	
θ (deg)	ϕ (deg)	θ (deg)	W (GeV)	$-k^2$ (GeV^2)	ϵ	$\cos\phi$	$\cos 2\phi$	$-t$ (GeV^2)	Correction Factor	$\frac{d\sigma}{d\Omega_\pi}\left(\frac{\mu b}{sr}\right)$
					(e) Data point 3b					
0.0– 1.2	$0 \leq \lvert\phi\rvert \leq 180$	0.8	2.147	0.294	0.880			0.006	2.180	8.05 ± 0.83
1.2– 2.4	$0 \leq \lvert\phi\rvert \leq 60$	1.8	2.115	0.298	0.888	0.830	0.424	0.007	2.188	11.07 ± 1.05
1.2– 2.4	$0 \leq \lvert\phi\rvert \leq 30$	1.9	2.111	0.300	0.889	0.951	0.812	0.007	2.188	11.31 ± 1.42
1.2– 2.4	$120 \leq \lvert\phi\rvert \leq 180$	1.8	2.184	0.290	0.869	−0.790	0.299	0.006	2.171	7.11 ± 0.85
1.2– 2.4	$150 \leq \lvert\phi\rvert \leq 180$	1.8	2.183	0.287	0.869	−0.957	0.834	0.006	2.171	5.32 ± 1.11
1.2– 2.4	$60 \leq \lvert\phi\rvert \leq 120$	1.9	2.148	0.297	0.879	0.058	−0.818	0.007	2.182	6.72 ± 0.79
2.4– 3.6	$0 \leq \lvert\phi\rvert \leq 60$	3.0	2.095	0.305	0.893	0.847	0.476	0.009	2.196	10.94 ± 0.81
2.4– 3.6	$0 \leq \lvert\phi\rvert \leq 30$	3.0	2.088	0.308	0.894	0.955	0.827	0.009	2.196	10.43 ± 1.03
2.4– 3.6	$120 \leq \lvert\phi\rvert \leq 180$	3.0	2.212	0.284	0.860	−0.840	0.450	0.007	2.163	5.82 ± 0.63
2.4– 3.6	$150 \leq \lvert\phi\rvert \leq 180$	3.0	2.220	0.283	0.858	−0.962	0.855	0.007	2.163	5.10 ± 0.78
2.4– 3.6	$60 \leq \lvert\phi\rvert \leq 120$	3.0	2.150	0.295	0.879	0.032	−0.816	0.008	2.182	9.12 ± 0.92
3.6– 4.8	$0 \leq \lvert\phi\rvert \leq 60$	4.2	2.072	0.312	0.898	0.879	0.577	0.012	2.200	11.99 ± 0.79
3.6– 4.8	$0 \leq \lvert\phi\rvert \leq 30$	4.2	2.064	0.314	0.900	0.959	0.842	0.012	2.200	12.50 ± 1.03
3.6– 4.8	$120 \leq \lvert\phi\rvert \leq 180$	4.2	2.236	0.278	0.853	−0.842	0.462	0.009	2.156	5.00 ± 0.54
3.6– 4.8	$150 \leq \lvert\phi\rvert \leq 180$	4.3	2.247	0.277	0.849	−0.949	0.804	0.009	2.156	4.70 ± 0.67
3.6– 4.8	$60 \leq \lvert\phi\rvert \leq 120$	4.1	2.155	0.294	0.877	0.031	−0.803	0.010	2.182	9.93 ± 1.16
4.8– 7.2	$0 \leq \lvert\phi\rvert \leq 60$	5.9	2.035	0.319	0.923	0.923	0.722	0.016	2.215	11.01 ± 0.55
4.8– 7.2	$0 \leq \lvert\phi\rvert \leq 30$	6.0	2.029	0.320	0.907	0.963	0.856	0.017	2.215	11.49 ± 0.64
4.8– 7.2	$120 \leq \lvert\phi\rvert \leq 180$	6.0	2.282	0.269	0.838	−0.921	0.714	0.015	2.146	4.38 ± 0.43
4.8– 7.2	$150 \leq \lvert\phi\rvert \leq 180$	6.1	2.289	0.269	0.835	−0.963	0.856	0.015	2.146	4.33 ± 0.47
7.2– 9.6	$0 \leq \lvert\phi\rvert \leq 30$	8.4	1.979	0.329	0.918	0.972	0.892	0.025	2.203	9.96 ± 0.62
7.2– 9.6	$150 \leq \lvert\phi\rvert \leq 180$	8.4	2.343	0.255	0.815	−0.966	0.867	0.025	2.134	4.20 ± 0.60
9.6–12.0	$0 \leq \lvert\phi\rvert \leq 30$	10.6	1.936	0.340	0.925	0.984	0.939	0.034	2.191	7.71 ± 0.64
12.0–14.4	$0 \leq \lvert\phi\rvert \leq 30$	13.2	1.886	0.346	0.934	0.922	0.968	0.046	2.175	5.63 ± 0.65
14.4–16.8	$0 \leq \lvert\phi\rvert \leq 30$	15.5	1.842	0.354	0.940	0.997	0.986	0.057	2.166	4.14 ± 0.71
					(f) Data point 4					
0.0– 1.2	$0 \leq \lvert\phi\rvert \leq 180$	0.8	2.147	0.176	0.853			0.003	2.173	7.42 ± 0.65
1.2– 2.4	$0 \leq \lvert\phi\rvert \leq 60$	1.9	2.111	0.183	0.865	0.835	0.435	0.004	2.192	9.52 ± 0.77
1.2– 2.4	$0 \leq \lvert\phi\rvert \leq 30$	1.9	2.104	0.185	0.867	0.955	0.828	0.004	2.192	9.34 ± 1.07
1.2– 2.4	$120 \leq \lvert\phi\rvert \leq 180$	1.9	2.192	0.174	0.836	−0.830	0.420	0.003	2.153	5.49 ± 0.58
1.2– 2.4	$150 \leq \lvert\phi\rvert \leq 180$	1.8	2.197	0.173	0.834	−0.952	0.814	0.003	2.153	5.19 ± 0.80
1.2– 2.4	$60 \leq \lvert\phi\rvert \leq 120$	1.9	2.154	0.178	0.850	0.035	−0.819	0.003	2.176	6.18 ± 0.70
2.4– 3.6	$0 \leq \lvert\phi\rvert \leq 60$	3.0	2.086	0.187	0.873	0.865	0.535	0.005	2.205	9.57 ± 0.64
2.4– 3.6	$0 \leq \lvert\phi\rvert \leq 30$	3.0	2.078	0.187	0.876	0.958	0.839	0.005	2.205	9.83 ± 0.84
2.4– 3.6	$120 \leq \lvert\phi\rvert \leq 180$	3.0	2.217	0.168	0.826	−0.832	0.426	0.004	2.139	3.59 ± 0.43
2.4– 3.6	$150 \leq \lvert\phi\rvert \leq 180$	3.0	2.233	0.168	0.819	−0.950	0.810	0.004	2.139	3.19 ± 0.53
2.4– 3.6	$60 \leq \lvert\phi\rvert \leq 120$	3.0	2.148	0.178	0.852	0.069	−0.805	0.005	2.176	8.40 ± 0.83
3.6– 4.8	$0 \leq \lvert\phi\rvert \leq 60$	4.2	2.055	0.191	0.882	0.905	0.664	0.007	2.222	10.86 ± 0.67
3.6– 4.8	$0 \leq \lvert\phi\rvert \leq 30$	4.2	2.049	0.192	0.884	0.964	0.862	0.007	2.222	11.78 ± 0.84
3.6– 4.8	$120 \leq \lvert\phi\rvert \leq 180$	4.1	2.234	0.163	0.819	−0.807	0.359	0.006	2.134	3.35 ± 0.47
3.6– 4.8	$150 \leq \lvert\phi\rvert \leq 180$	4.0	2.255	0.160	0.810	−0.959	0.841	0.006	2.134	2.28 ± 0.47
3.6– 4.8	$60 \leq \lvert\phi\rvert \leq 120$	4.0	2.148	0.176	0.852	0.085	−0.798	0.007	2.176	9.53 ± 1.28
4.8– 7.2	$0 \leq \lvert\phi\rvert \leq 60$	5.9	2.016	0.197	0.893	0.937	0.767	0.011	2.236	11.09 ± 0.51
4.8– 7.2	$0 \leq \lvert\phi\rvert \leq 30$	6.0	2.009	0.197	0.895	0.965	0.867	0.011	2.236	10.71 ± 0.54
4.8– 7.2	$120 \leq \lvert\phi\rvert \leq 180$	5.8	2.300	0.154	0.790	−0.937	0.763	0.011	2.115	3.07 ± 0.42
4.8– 7.2	$150 \leq \lvert\phi\rvert \leq 180$	5.8	2.304	0.153	0.788	−0.953	0.818	0.011	2.115	3.09 ± 0.44
7.2– 9.6	$0 \leq \lvert\phi\rvert \leq 30$	8.3	1.954	0.206	0.907	0.981	0.926	0.021	2.266	9.34 ± 0.57
7.2– 9.6	$150 \leq \lvert\phi\rvert \leq 180$	8.0	2.359	0.142	0.761	−0.967	0.871	0.018	2.104	2.76 ± 0.86
9.6–12.0	$0 \leq \lvert\phi\rvert \leq 30$	10.7	1.897	0.211	0.921	0.991	0.963	0.026	2.292	7.56 ± 0.64
12.0–14.4	$0 \leq \lvert\phi\rvert \leq 30$	12.9	1.853	0.218	0.930	0.995	0.981	0.034	2.323	5.76 ± 0.77
14.4–16.8	$0 \leq \lvert\phi\rvert \leq 30$	15.1	1.815	0.228	0.937	0.998	0.992	0.043	2.335	7.10 ± 1.42

triggers to computer triggers. A small adjustment to this ratio was necessitated by the failure of the floor trigger circuitry to register some extreme out-of-time accidentals which were registered by the counting room circuitry. The correction is typically <1.17, but ranges up to 1.48. The systematic uncertainty due to it is 1.0% or less.

Corrections with essentially no systematic uncertainties were made for other triggering, computer, and tape-handling losses, and for events rejected because of multiple line identification. Small corrections were applied for chamber inefficiency and for scintillation trigger counter dead times in coincidence signals. Accidental counts in these counters were automatically eliminated by counter-position cuts in the data analysis program. A correction was also made for miscalibration of the charge-collecting integrator. Finally, allowances were made for systematic uncertainties in counter efficiencies, Faraday-cup calibration, target properties, Monte Carlo acceptance calculations, and the subtraction of accidental arm-to-arm coincidences.

Several small effects involving misidentification

TABLE VI *(Continued)*

Bins		Kinematic averages							Results	
θ (deg)	ϕ (deg)	θ (deg)	W (GeV)	$-k^2$ (GeV^2)	ϵ	cosϕ	cos2ϕ	$-t$ (GeV^2)	Correction factor	$\frac{d\sigma}{d\Omega_\pi}\left(\frac{\mu b}{sr}\right)$
				(g) Data point 5						
0.0–1.2	$0 \leq \lvert\phi\rvert \leq 180$	0.81	2.501	0.296	0.735	0.082	0.077	0.003	1.749	4.88±0.32
1.2–2.4	$0 \leq \lvert\phi\rvert \leq 60$	1.86	2.458	0.309	0.756	0.848	0.479	0.004	1.759	6.51±0.37
1.2–2.4	$0 \leq \lvert\phi\rvert \leq 30$	1.88	2.451	0.311	0.759	0.956	0.831	0.004	1.761	6.51±0.51
1.2–2.4	$120 \leq \lvert\phi\rvert \leq 180$	1.85	2.546	0.282	0.712	−0.812	0.364	0.004	1.723	3.31±0.29
1.2–2.4	$150 \leq \lvert\phi\rvert \leq 180$	1.85	2.554	0.280	0.707	−0.954	0.822	0.004	1.719	2.74±0.36
1.2–2.4	$60 \leq \phi \leq 120$	1.86	2.504	0.293	0.733	0.009	−0.830	0.004	1.747	5.18±0.53
1.2–2.4	$-60 \leq \phi \leq -120$	1.81	2.501	0.296	0.735	0.059	−0.820	0.004	1.747	5.74±0.62
2.4–3.6	$0 \leq \lvert\phi\rvert \leq 60$	3.02	2.427	0.316	0.770	0.870	0.551	0.007	1.812	8.05±0.38
2.4–3.6	$0 \leq \lvert\phi\rvert \leq 30$	3.03	2.418	0.319	0.774	0.960	0.845	0.007	1.812	8.37±0.52
2.4–3.6	$120 \leq \lvert\phi\rvert \leq 180$	3.02	2.577	0.272	0.694	−0.847	0.477	0.006	1.714	2.27±0.21
2.4–3.6	$150 \leq \lvert\phi\rvert \leq 180$	3.00	2.585	0.268	0.690	−0.969	0.880	0.006	1.713	1.86±0.24
2.4–3.6	$60 \leq \phi \leq 120$	2.99	2.495	0.296	0.738	0.063	−0.818	0.006	1.746	6.27±0.61
2.4–3.6	$-60 \leq \phi \leq -120$	2.97	2.503	0.301	0.733	0.056	−0.820	0.006	1.747	4.59±0.62
3.6–4.8	$0 \leq \lvert\phi\rvert \leq 60$	4.21	2.396	0.324	0.784	0.896	0.637	0.010	1.812	7.91±0.36
3.6–4.8	$0 \leq \lvert\phi\rvert \leq 30$	4.24	2.387	0.327	0.788	0.963	0.858	0.010	1.815	8.12±0.46
3.6–4.8	$120 \leq \lvert\phi\rvert \leq 180$	4.13	2.610	0.261	0.675	−0.903	0.651	0.009	1.693	2.31±0.22
3.6–4.8	$150 \leq \lvert\phi\rvert \leq 180$	4.15	2.618	0.257	0.670	−0.957	0.835	0.009	1.691	2.19±0.24
3.6–4.8	$60 \leq \phi \leq 120$	4.01	2.489	0.296	0.741	0.107	−0.793	0.009	1.746	5.36±1.09
3.6–4.8	$-60 \leq \phi \leq -120$	3.96	2.473	0.292	0.750	0.227	−0.717	0.008	1.747	4.15±1.43
4.8–6.0	$0 \leq \lvert\phi\rvert \leq 60$	5.38	2.362	0.335	0.798	0.938	0.772	0.014	1.820	7.26±0.38
4.8–6.0	$0 \leq \lvert\phi\rvert \leq 30$	5.40	2.357	0.337	0.800	0.967	0.874	0.014	1.820	7.01±0.40
4.8–6.0	$120 \leq \lvert\phi\rvert \leq 180$	5.34	2.658	0.251	0.644	−0.958	0.843	0.014	1.687	2.29±0.24
4.8–6.0	$150 \leq \lvert\phi\rvert \leq 180$	5.34	2.660	0.250	0.643	−0.969	0.882	0.014	1.687	2.30±0.25
6.0–7.2	$0 \leq \lvert\phi\rvert \leq 60$	6.56	2.330	0.345	0.811	0.966	0.869	0.019	1.827	6.97±0.41
6.0–7.2	$0 \leq \lvert\phi\rvert \leq 30$	6.57	2.329	0.345	0.811	0.969	0.880	0.019	1.827	6.97±0.43
6.0–7.2	$120 \leq \lvert\phi\rvert \leq 180$	6.65	2.697	0.235	0.619	−0.976	0.907	0.021	1.673	1.70±0.23
6.0–7.2	$150 \leq \lvert\phi\rvert \leq 180$	6.65	2.697	0.235	0.619	−0.976	0.907	0.021	1.673	1.70±0.23
7.2–8.4	$0 \leq \lvert\phi\rvert \leq 30$	7.81	2.294	0.356	0.824	0.984	0.936	0.024	1.830	7.48±0.48
7.2–8.4	$150 \leq \lvert\phi\rvert \leq 180$	7.69	2.715	0.227	0.607	−0.985	0.940	0.028	1.666	1.98±0.33
8.4–9.6	$0 \leq \lvert\phi\rvert \leq 30$	8.98	2.260	0.361	0.836	0.990	0.960	0.030	1.834	5.55±0.43
8.4–9.6	$150 \leq \lvert\phi\rvert \leq 180$	8.71	2.742	0.215	0.589	−0.992	0.966	0.036	1.661	1.80±0.51
9.6–10.8	$0 \leq \lvert\phi\rvert \leq 30$	10.16	2.233	0.372	0.845	0.992	0.970	0.036	1.841	5.41±0.48
9.6–10.8	$150 \leq \lvert\phi\rvert \leq 180$	10.26	2.784	0.208	0.556	−0.997	0.988	0.051	1.643	2.06±1.54
10.8–12.0	$0 \leq \lvert\phi\rvert \leq 30$	11.39	2.204	0.378	0.855	0.995	0.981	0.044	1.847	5.60±0.55
12.0–13.2	$0 \leq \lvert\phi\rvert \leq 30$	12.51	2.176	0.383	0.862	0.997	0.987	0.050	1.859	4.69±0.55
13.2–14.4	$0 \leq \lvert\phi\rvert \leq 30$	13.76	2.153	0.396	0.868	0.998	0.994	0.059	1.863	4.31±0.63
14.4–15.6	$0 \leq \lvert\phi\rvert \leq 30$	15.00	2.122	0.408	0.876	0.999	0.996	0.067	1.866	3.94±0.71
15.6–16.8	$0 \leq \lvert\phi\rvert \leq 30$	15.96	2.112	0.420	0.878	0.999	0.995	0.075	1.873	2.79±0.96
16.8–18.0	$0 \leq \lvert\phi\rvert \leq 30$	17.41	2.077	0.419	0.888	0.999	0.998	0.085	1.747	1.99±1.30

of $e\pi$ events as other types may be included among normalization corrections. These are Čerenkov counter dead times and inefficiency of the electron-arm Čerenkov counter. Other such misidentification effects will be considered in Sec. VIII C.

B. Corrections Related to Aperture Definition

Monte Carlo simulations, including multiple scattering, were used to compute the percentages of good events excluded by horizontal target position cuts. We added $(0.5 \pm 0.5)\%$ to the two-arm totals to allow for limitations of the Gaussian multiple-scattering formulas.

An unexpected fraction of the accepted hadrons, and about a five time smaller fraction of the accepted electrons, did not appear to originate from the target; rather, they seemed to have entered the acceptance after scattering in the poles of the bending magnet. A correction was made to account for those particles which were scattered off the magnet poles but were not excluded by the target position cuts. We estimated the total percentages of such events on the hadron arm by examining the apparent horizontal distributions of particles at the target and at the bending magnet entrance. Outside the regions of valid particle positions as determined by the Monte Carlo program these distributions were approximately the same for all data points. The percentages of contamination thus depended mainly on the target-position cuts, and including a small allowance for the electron arm ranged from 4.8% to 10.1%.

By examining the missing-mass spectra of events known to be invalid—those outside the target cuts—we found the contamination within our missing-mass cuts to be 0.4 ± 0.2 times the percentages described above. The uncertainty estimate allows for all approximations made, and is also large enough to include a small bin dependence of this correction.

C. Hadron Absorption

Absorption of hadrons via nuclear interactions in the hadron spectrometer caused some $e\pi$ events to be lost entirely, and others to be misidentified as ep events. Test runs performed with a lead absorber just upstream of the last trigger counter indicated a loss of $(11 \pm 11)\%$ of those events undergoing inelastic interactions in the lead. We assume that this was true for all absorbers beyond the middle of the third chamber, and that any inelastic interaction earlier in the system resulted in losing the event. The total absorptive loss is then $(1.5 \pm 0.5)\%$.

The misidentification probability was determined by analyzing ep events as if they were $e\pi$ events and looking for a $\pi^+ n$ peak. This method automatically took into account any effects due to pion decay and Čerenkov counter inefficiency. The resulting correction decreases from 4.5% at 1.3 GeV to 1.5% above 2.4 GeV. One point deter-

TABLE VI *(Continued)*

Bins		Kinematic averages							Results	
θ (deg)	ϕ (deg)	θ (deg)	W (GeV)	$-k^2$ (GeV^2)	ϵ	$\cos\phi$	$\cos 2\phi$	$-t$ (GeV^2)	Correction factor	$\frac{d\sigma}{d\Omega_\pi}\left(\frac{\mu b}{sr}\right)$
				(h) Data point 6						
2.4–3.6	$0 \le \lvert\phi\rvert \le 60$	3.22	2.400	0.320	0.783	0.916	0.696	0.008	1.759	9.31 ± 1.46
2.4–3.6	$0 \le \lvert\phi\rvert \le 30$	3.20	2.397	0.320	0.784	0.961	0.850	0.008	1.759	10.38 ± 1.86
3.6–4.8	$0 \le \lvert\phi\rvert \le 60$	4.23	2.381	0.329	0.790	0.958	0.839	0.010	1.760	6.79 ± 0.83
3.6–4.8	$0 \le \lvert\phi\rvert \le 30$	4.24	2.379	0.329	0.791	0.967	0.874	0.011	1.760	7.25 ± 0.88
4.8–6.0	$0 \le \lvert\phi\rvert \le 30$	5.40	2.354	0.334	0.802	0.970	0.885	0.014	1.765	6.85 ± 0.65
6.0–7.2	$0 \le \lvert\phi\rvert \le 30$	6.60	2.324	0.347	0.813	0.979	0.917	0.019	1.766	8.00 ± 0.62
7.2–8.4	$0 \le \lvert\phi\rvert \le 30$	7.81	2.295	0.354	0.823	0.984	0.938	0.025	1.768	6.79 ± 0.53
8.4–9.6	$0 \le \lvert\phi\rvert \le 30$	9.01	2.263	0.363	0.835	0.988	0.954	0.031	1.771	5.53 ± 0.44
9.6–10.8	$0 \le \lvert\phi\rvert \le 30$	10.20	2.234	0.370	0.844	0.989	0.958	0.037	1.776	5.93 ± 0.44
10.8–12.0	$0 \le \lvert\phi\rvert \le 30$	11.40	2.206	0.380	0.853	0.993	0.972	0.044	1.779	5.68 ± 0.44
12.0–13.2	$0 \le \lvert\phi\rvert \le 30$	12.55	2.178	0.385	0.862	0.994	0.975	0.051	1.784	4.37 ± 0.37
13.2–14.4	$0 \le \lvert\phi\rvert \le 30$	13.78	2.147	0.395	0.870	0.994	0.977	0.059	1.785	4.20 ± 0.36
14.4–15.6	$0 \le \lvert\phi\rvert \le 30$	14.98	2.125	0.402	0.876	0.994	0.976	0.068	1.785	3.52 ± 0.32
15.6–16.8	$0 \le \lvert\phi\rvert \le 30$	16.17	2.100	0.408	0.882	0.995	0.981	0.076	1.786	3.89 ± 0.36
16.8–18.0	$0 \le \lvert\phi\rvert \le 30$	17.43	2.069	0.414	0.890	0.995	0.979	0.085	1.791	3.37 ± 0.36
18.0–19.2	$0 \le \lvert\phi\rvert \le 30$	18.55	2.042	0.419	0.896	0.997	0.988	0.093	1.798	3.08 ± 0.34
19.2–20.4	$0 \le \lvert\phi\rvert \le 30$	19.77	2.021	0.425	0.901	0.997	0.990	0.102	1.801	2.23 ± 0.32
20.4–21.6	$0 \le \lvert\phi\rvert \le 30$	21.01	1.994	0.431	0.907	0.998	0.990	0.112	1.809	2.42 ± 0.34

mined from the lead absorber test agreed with this determination.

D. Pion Decay

Pions which decayed in the apparatus could be lost or appear with the wrong momentum. A Monte Carlo simulation was made in which the pion was allowed to decay at random points along the arm weighted by the decay probability. The fraction of $\pi^+ n$ events lost comes to a constant, 0.697 ± 0.035, times the momentum-dependent probability of pion decay in the 12.7-m path length of the apparatus.

E. Pion-Pair Contamination

For some data points, a considerable number of pion-pair events were accepted by the spectrometers. There were four circumstances under which a $\pi\pi$ event could fire the left-arm Čerenkov counter, and thus count as an $e\pi$ event: a simul-

TABLE VI *(Continued)*

Bins		Kinematic averages							Results	
θ (deg)	ϕ (deg)	θ (deg)	W (GeV)	$-k^2$ (GeV^2)	ϵ	$\cos\phi$	$\cos 2\phi$	$-t$ (GeV^2)	Correction factor	$\frac{d\sigma}{d\Omega_\pi}\left(\frac{\mu b}{sr}\right)$
				(i) Data point 7						
0.0–1.2	all	0.81	2.150	0.396	0.870	0.042	0.040	0.010	1.848	8.98 ± 0.68
1.2–2.4	$0 \le \lvert\phi\rvert \le 60$	1.84	2.118	0.402	0.878	0.848	0.480	0.012	1.855	10.07 ± 0.76
1.2–2.4	$0 \le \lvert\phi\rvert \le 30$	1.84	2.114	0.404	0.879	0.963	0.858	0.012	1.855	10.27 ± 1.04
1.2–2.4	$120 \le \lvert\phi\rvert \le 180$	1.85	2.184	0.389	0.860	−0.812	0.363	0.010	1.840	8.77 ± 0.70
1.2–2.4	$150 \le \lvert\phi\rvert \le 180$	1.85	2.189	0.386	0.859	−0.949	0.804	0.010	1.840	7.80 ± 0.94
1.2–2.4	$60 \le \phi \le 120$	1.77	2.149	0.395	0.870	0.053	−0.816	0.011	1.848	8.79 ± 0.94
1.2–2.4	$-60 \le \phi \le -120$	1.82	2.155	0.400	0.868	0.063	−0.820	0.011	1.848	7.82 ± 0.94
2.4–3.6	$0 \le \lvert\phi\rvert \le 60$	3.00	2.100	0.408	0.883	0.845	0.470	0.014	1.858	11.09 ± 0.63
2.4–3.6	$0 \le \lvert\phi\rvert \le 30$	3.01	2.092	0.410	0.885	0.953	0.818	0.014	1.861	10.81 ± 0.82
2.4–3.6	$120 \le \lvert\phi\rvert \le 180$	3.01	2.205	0.382	0.854	−0.826	0.410	0.011	1.836	7.09 ± 0.51
2.4–3.6	$150 \le \lvert\phi\rvert \le 180$	3.04	2.214	0.379	0.851	−0.954	0.822	0.011	1.834	6.51 ± 0.66
2.4–3.6	$60 \le \phi \le 120$	2.99	2.156	0.397	0.868	−0.007	−0.832	0.012	1.847	8.68 ± 0.87
2.4–3.6	$-60 \le \phi \le -120$	2.93	2.151	0.398	0.869	0.056	−0.816	0.012	1.848	10.14 ± 1.15
3.6–4.8	$0 \le \lvert\phi\rvert \le 60$	4.20	2.077	0.414	0.888	0.877	0.576	0.017	1.863	11.01 ± 0.60
3.6–4.8	$0 \le \lvert\phi\rvert \le 30$	4.23	2.070	0.416	0.890	0.961	0.852	0.017	1.865	11.52 ± 0.76
3.6–4.8	$120 \le \lvert\phi\rvert \le 180$	4.19	2.230	0.376	0.846	−0.863	0.529	0.013	1.831	6.53 ± 0.46
3.6–4.8	$150 \le \lvert\phi\rvert \le 180$	4.20	2.239	0.374	0.843	−0.959	0.844	0.013	1.829	6.09 ± 0.55
3.6–4.8	$60 \le \phi \le 120$	4.15	2.149	0.394	0.870	0.074	−0.822	0.014	1.847	9.16 ± 1.07
3.6–4.8	$-60 \le \phi \le -120$	4.13	2.144	0.394	0.871	0.102	−0.806	0.014	1.847	10.43 ± 1.48
4.8–6.0	$0 \le \lvert\phi\rvert \le 60$	5.40	2.055	0.421	0.893	0.911	0.677	0.020	1.869	10.71 ± 0.58
4.8–6.0	$0 \le \lvert\phi\rvert \le 30$	5.41	2.049	0.423	0.895	0.960	0.845	0.020	1.871	10.68 ± 0.67
4.8–6.0	$120 \le \lvert\phi\rvert \le 180$	5.40	2.256	0.366	0.838	−0.902	0.651	0.015	1.825	5.40 ± 0.40
4.8–6.0	$150 \le \lvert\phi\rvert \le 180$	5.42	2.263	0.365	0.835	−0.958	0.837	0.015	1.823	5.16 ± 0.46
6.0–7.2	$0 \le \lvert\phi\rvert \le 60$	6.54	2.032	0.426	0.899	0.934	0.759	0.024	1.874	10.21 ± 0.60
6.0–7.2	$0 \le \lvert\phi\rvert \le 30$	6.56	2.027	0.427	0.900	0.969	0.881	0.024	1.875	9.90 ± 0.64
6.0–7.2	$120 \le \lvert\phi\rvert \le 180$	6.56	2.288	0.359	0.826	−0.941	0.779	0.019	1.819	5.33 ± 0.45
6.0–7.2	$150 \le \lvert\phi\rvert \le 180$	6.58	2.292	0.359	0.825	−0.966	0.870	0.019	1.819	4.97 ± 0.45
7.2–8.4	$0 \le \lvert\phi\rvert \le 30$	7.80	2.006	0.432	0.904	0.966	0.869	0.029	1.886	8.77 ± 0.60
7.2–8.4	$150 \le \lvert\phi\rvert \le 180$	7.75	2.315	0.352	0.817	−0.968	0.875	0.025	1.814	4.59 ± 0.44
8.4–9.6	$0 \le \lvert\phi\rvert \le 30$	9.02	1.981	0.439	0.909	0.975	0.903	0.034	1.886	9.77 ± 0.66
8.4–9.6	$150 \le \lvert\phi\rvert \le 180$	9.00	2.345	0.341	0.806	−0.982	0.932	0.031	1.806	4.21 ± 0.45
9.6–10.8	$0 \le \lvert\phi\rvert \le 30$	10.15	1.958	0.441	0.914	0.983	0.934	0.040	1.893	7.68 ± 0.61
9.6–10.8	$150 \le \lvert\phi\rvert \le 180$	10.18	2.369	0.334	0.796	−0.984	0.936	0.039	1.802	3.44 ± 0.45
10.8–12.0	$0 \le \lvert\phi\rvert \le 30$	11.38	1.938	0.452	0.917	0.988	0.951	0.046	1.896	6.75 ± 0.64
10.8–12.0	$150 \le \lvert\phi\rvert \le 180$	11.42	2.399	0.323	0.784	−0.991	0.964	0.049	1.798	4.82 ± 0.63
12.0–13.2	$0 \le \lvert\phi\rvert \le 30$	12.54	1.914	0.450	0.922	0.992	0.967	0.052	1.895	6.08 ± 0.66
13.2–14.4	$0 \le \lvert\phi\rvert \le 30$	13.78	1.893	0.458	0.925	0.992	0.970	0.059	1.897	5.08 ± 0.63
14.4–15.6	$0 \le \lvert\phi\rvert \le 30$	14.96	1.872	0.463	0.928	0.995	0.982	0.066	1.900	4.88 ± 0.66
15.6–16.8	$0 \le \lvert\phi\rvert \le 30$	16.18	1.853	0.471	0.931	0.995	0.981	0.074	1.901	3.52 ± 0.65
16.8–18.0	$0 \le \lvert\phi\rvert \le 30$	17.31	1.835	0.476	0.934	0.997	0.986	0.081	1.904	3.56 ± 0.74

taneous accidental count in the Čerenkov counter, the production of a knockon electron, a decay muon with sufficient momentum, and a pion with sufficient momentum (typically >3.6 GeV). The first three effects caused misidentification of 1–2% of $\pi\pi$ events; their sum was measured as a function of momentum by considering only those events within the acceptance of the electron-arm shower counter. The fourth effect could be very large at some data points and its determination required using parametrized Čerenkov counter efficiency curves.

For data points 3b–12 $\pi\pi$ data were collected and the total $\pi\pi$ contamination was computed from

TABLE VI *(Continued)*

Bins		Kinematic averages							Results	
θ (deg)	ϕ (deg)	θ (deg)	W (GeV)	$-k^2$ (GeV^2)	ϵ	cosϕ	cos2ϕ	$-t$ (GeV^2)	Correction factors	$\frac{d\sigma}{d\Omega_\pi}\left(\frac{\mu b}{sr}\right)$
				(j) Data point 8						
0.0–1.2	$0 \leq \lvert\phi\rvert \leq 180$	0.80	1.908	0.451	0.922	−0.069	−0.031	0.021	1.757	11.05± 0.98
1.2–2.4	$0 \leq \lvert\phi\rvert \leq 60$	1.85	1.881	0.455	0.927	0.832	0.425	0.023	1.765	9.90± 1.01
1.2–2.4	$0 \leq \lvert\phi\rvert \leq 30$	1.82	1.878	0.455	0.928	0.945	0.789	0.023	1.765	10.91± 1.52
1.2–2.4	$120 \leq \lvert\phi\rvert \leq 180$	1.88	1.933	0.448	0.918	−0.827	0.412	0.020	1.749	10.21± 0.89
1.2–2.4	$150 \leq \lvert\phi\rvert \leq 180$	1.91	1.939	0.448	0.917	−0.957	0.835	0.020	1.745	9.25± 1.15
1.2–2.4	$60 \leq \phi \leq 120$	1.81	1.908	0.457	0.922	0.028	−0.843	0.022	1.755	13.36± 1.60
1.2–2.4	$-60 \leq \phi \leq -120$	1.85	1.906	0.453	0.923	−0.021	−0.854	0.022	1.757	10.96± 1.42
2.4–3.6	$0 \leq \lvert\phi\rvert \leq 60$	3.04	1.867	0.461	0.929	0.828	0.414	0.026	1.772	11.08± 0.87
2.4–3.6	$0 \leq \lvert\phi\rvert \leq 30$	3.05	1.860	0.462	0.930	0.953	0.821	0.026	1.773	10.89± 1.21
2.4–3.6	$120 \leq \lvert\phi\rvert \leq 180$	3.02	1.949	0.445	0.915	−0.852	0.489	0.020	1.741	9.73± 0.66
2.4–3.6	$150 \leq \lvert\phi\rvert \leq 180$	3.00	1.952	0.445	0.914	−0.952	0.814	0.020	1.741	10.12± 0.92
2.4–3.6	$60 \leq \phi \leq 120$	2.91	1.909	0.449	0.922	−0.007	−0.821	0.022	1.757	10.88± 1.23
2.4–3.6	$-60 \leq \phi \leq -120$	2.98	1.909	0.452	0.922	0.025	−0.822	0.023	1.757	12.74± 1.60
3.6–4.8	$0 \leq \lvert\phi\rvert \leq 60$	4.23	1.848	0.465	0.932	0.868	0.542	0.029	1.776	9.82± 0.78
3.6–4.8	$0 \leq \lvert\phi\rvert \leq 30$	4.28	1.841	0.466	0.933	0.960	0.845	0.029	1.779	10.02± 1.01
3.6–4.8	$120 \leq \lvert\phi\rvert \leq 180$	4.26	1.968	0.438	0.911	−0.846	0.475	0.021	1.736	10.48± 0.61
3.6–4.8	$150 \leq \lvert\phi\rvert \leq 180$	4.25	1.977	0.438	0.910	−0.958	0.838	0.021	1.733	9.60± 0.75
3.6–4.8	$60 \leq \phi \leq 120$	4.17	1.913	0.453	0.921	−0.028	−0.814	0.024	1.752	11.46± 1.47
3.6–4.8	$-60 \leq \phi \leq -120$	3.98	1.912	0.448	0.922	−0.055	−0.784	0.024	1.754	14.30± 2.30
4.8–6.0	$0 \leq \lvert\phi\rvert \leq 60$	5.38	1.832	0.471	0.934	0.907	0.665	0.032	1.782	10.50± 0.86
4.8–6.0	$0 \leq \lvert\phi\rvert \leq 30$	5.41	1.827	0.472	0.935	0.958	0.840	0.033	1.783	9.97± 0.96
4.8–6.0	$120 \leq \lvert\phi\rvert \leq 180$	5.38	1.989	0.437	0.907	−0.885	0.598	0.023	1.729	8.54± 0.50
4.8–6.0	$150 \leq \lvert\phi\rvert \leq 180$	5.41	1.995	0.435	0.906	−0.960	0.847	0.023	1.726	8.37± 0.59
6.0–7.2	$0 \leq \lvert\phi\rvert \leq 60$	6.55	1.814	0.476	0.937	0.952	0.818	0.036	1.790	9.85± 0.95
6.0–7.2	$0 \leq \lvert\phi\rvert \leq 30$	6.56	1.812	0.476	0.937	0.966	0.868	0.036	1.790	9.94± 1.00
6.0–7.2	$120 \leq \lvert\phi\rvert \leq 180$	6.58	2.009	0.429	0.903	−0.904	0.658	0.025	1.721	8.17± 0.46
6.0–7.2	$150 \leq \lvert\phi\rvert \leq 180$	6.60	2.014	0.426	0.902	−0.961	0.851	0.025	1.721	7.74± 0.52
7.2–8.4	$0 \leq \lvert\phi\rvert \leq 30$	7.76	1.795	0.488	0.939	0.968	0.877	0.042	1.797	7.44± 0.95
7.2–8.4	$150 \leq \lvert\phi\rvert \leq 180$	7.80	2.036	0.424	0.897	−0.961	0.848	0.028	1.718	6.99± 0.45
8.4–9.6	$150 \leq \lvert\phi\rvert \leq 180$	9.02	2.055	0.416	0.893	−0.964	0.860	0.032	1.713	6.49± 0.41
9.6–10.8	$150 \leq \lvert\phi\rvert \leq 180$	10.19	2.076	0.411	0.888	−0.966	0.867	0.037	1.706	5.75± 0.36
10.8–12.0	$150 \leq \lvert\phi\rvert \leq 180$	11.38	2.100	0.407	0.882	−0.967	0.874	0.044	1.701	5.32± 0.34
12.0–13.2	$150 \leq \lvert\phi\rvert \leq 180$	12.58	2.122	0.400	0.877	−0.971	0.888	0.051	1.692	4.50± 0.30
13.2–14.4	$150 \leq \lvert\phi\rvert \leq 180$	13.76	2.146	0.394	0.870	−0.975	0.901	0.059	1.687	4.29± 0.30
14.4–15.6	$150 \leq \lvert\phi\rvert \leq 180$	15.02	2.172	0.388	0.863	−0.980	0.923	0.069	1.682	3.70± 0.29
15.6–16.8	$150 \leq \lvert\phi\rvert \leq 180$	16.22	2.196	0.382	0.856	−0.985	0.941	0.081	1.676	3.52± 0.28
16.8–18.0	$150 \leq \lvert\phi\rvert \leq 180$	17.36	2.219	0.377	0.849	−0.987	0.948	0.093	1.670	3.31± 0.28
18.0–19.2	$150 \leq \lvert\phi\rvert \leq 180$	18.59	2.246	0.367	0.840	−0.990	0.961	0.107	1.664	3.26± 0.30
19.2–20.4	$150 \leq \lvert\phi\rvert \leq 180$	19.82	2.270	0.360	0.832	−0.992	0.967	0.123	1.661	2.38± 0.25
20.4–21.6	$150 \leq \lvert\phi\rvert \leq 180$	20.90	2.295	0.355	0.823	−0.992	0.966	0.139	1.658	1.51± 0.22
21.6–22.8	$150 \leq \lvert\phi\rvert \leq 180$	22.19	2.323	0.348	0.813	−0.994	0.978	0.159	1.650	1.95± 0.25
22.8–24.0	$150 \leq \lvert\phi\rvert \leq 180$	23.27	2.343	0.339	0.806	−0.995	0.979	0.177	1.648	1.33± 0.21
24.0–25.2	$150 \leq \lvert\phi\rvert \leq 180$	24.50	2.376	0.333	0.792	−0.997	0.987	0.201	1.643	1.15± 0.21
25.2–26.4	$150 \leq \lvert\phi\rvert \leq 180$	25.73	2.405	0.327	0.779	−0.996	0.986	0.227	1.637	0.97± 0.21

the probabilities of misidentification. The corrections for points 1 and 2 were determined by using the shower counter on the electron arm and information from the other data points. For high left-arm momenta at data point 6, the correction was too large to be made safely, and the affected bins were discarded. Elsewhere, corrections of 0–9% were applied.

F. Target-Empty Rates

The target-empty rate was measured only for data point 3b, where it was found to constitute $(0.65 \pm 0.25)\%$ of the total rate within the $\pi^+ n$ missing-mass cuts. For other data points, a crude Fermi model was utilized to compute cross sections for the aluminum target windows. For point 3b, the predictions were in agreement with the measurements.

G. Radiative Corrections

The purpose of radiative corrections is to account for the effects of the low-energy photons that accompany any physical process. The radiative correction gives the proportion of the events missed due to any energy loss greater than some cutoff. In terms of observed and "nonradiative" cross sections this is written as

$$\sigma_{\text{obs}} = \sigma_{\text{theor}}(1 + \delta) . \tag{16}$$

The calculation of δ must include a sum over the number of radiated photons as well as integrals over their direction and energy.

The basic calculation is described by Meister and Yennie.[46] They include terms for radiation from hadron lines, which can become significant at GeV energies. Bartl and Urban (BU)[47] used more accurate kinematical expressions and ap-

TABLE VI *(Continued)*

Bins		Kinematic averages							Results	
θ (deg)	ϕ (deg)	θ (deg)	W (GeV)	$-k^2$ (GeV^2)	ϵ	cosϕ	cos2ϕ	$-t$ (GeV^2)	Correction factor	$\frac{d\sigma}{d\Omega_\pi}\left(\frac{\mu b}{sr}\right)$
				(k) Data point 9						
0.0– 1.2	$0 \le \lvert\phi\rvert \le 180$	0.8	2.150	0.795	0.830			0.033	1.653	7.25 ± 0.69
1.2– 2.4	$0 \le \lvert\phi\rvert \le 60$	1.9	2.122	0.812	0.837	0.856	0.506	0.037	1.658	7.05 ± 0.73
1.2– 2.4	$0 \le \lvert\phi\rvert \le 30$	1.9	2.118	0.815	0.838	0.969	0.879	0.037	1.658	7.28 ± 1.01
1.2– 2.4	$120 \le \lvert\phi\rvert \le 180$	1.9	2.179	0.777	0.821	−0.846	0.468	0.031	1.651	6.19 ± 0.68
1.2– 2.4	$150 \le \lvert\phi\rvert \le 180$	1.9	2.183	0.775	0.820	−0.954	0.824	0.031	1.651	6.59 ± 0.99
1.2– 2.4	$60 \le \lvert\phi\rvert \le 120$	1.8	2.150	0.793	0.830	0.016	−0.827	0.034	1.654	7.48 ± 0.79
2.4– 3.6	$0 \le \lvert\phi\rvert \le 60$	3.0	2.105	0.820	0.842	0.877	0.576	0.040	1.663	6.30 ± 0.57
2.4– 3.6	$0 \le \lvert\phi\rvert \le 30$	3.0	2.100	0.825	0.843	0.971	0.886	0.041	1.663	6.90 ± 0.80
2.4– 3.6	$120 \le \lvert\phi\rvert \le 180$	3.0	2.192	0.775	0.817	−0.818	0.390	0.032	1.646	5.55 ± 0.53
2.4– 3.6	$150 \le \lvert\phi\rvert \le 180$	3.0	2.199	0.769	0.815	−0.951	0.812	0.031	1.646	5.19 ± 0.69
2.4– 3.6	$60 \le \lvert\phi\rvert \le 120$	3.0	2.151	0.799	0.829	−0.014	−0.810	0.036	1.654	6.24 ± 0.71
3.6– 4.8	$0 \le \lvert\phi\rvert \le 60$	4.2	2.087	0.830	0.847	0.876	0.575	0.045	1.665	6.66 ± 0.55
3.6– 4.8	$0 \le \lvert\phi\rvert \le 30$	4.2	2.082	0.835	0.848	0.957	0.835	0.046	1.665	7.06 ± 0.70
3.6– 4.8	$120 \le \lvert\phi\rvert \le 180$	4.2	2.214	0.760	0.810	−0.865	0.537	0.032	1.643	5.88 ± 0.53
3.6– 4.8	$150 \le \lvert\phi\rvert \le 180$	4.2	2.220	0.757	0.808	−0.954	0.824	0.032	1.643	5.80 ± 0.66
3.6– 4.8	$60 \le \lvert\phi\rvert \le 120$	4.1	2.145	0.800	0.831	0.054	−0.795	0.038	1.654	8.22 ± 1.06
4.8– 7.2	$0 \le \lvert\phi\rvert \le 60$	5.9	2.059	0.843	0.854	0.917	0.702	0.053	1.669	6.29 ± 0.37
4.8– 7.2	$0 \le \lvert\phi\rvert \le 30$	6.0	2.052	0.846	0.856	0.966	0.871	0.054	1.669	6.09 ± 0.42
4.8– 7.2	$120 \le \lvert\phi\rvert \le 180$	5.9	2.248	0.742	0.799	−0.929	0.741	0.035	1.636	5.78 ± 0.36
4.8– 7.2	$150 \le \lvert\phi\rvert \le 180$	5.9	2.252	0.740	0.798	−0.962	0.856	0.035	1.636	5.69 ± 0.41
7.2– 9.6	$0 \le \lvert\phi\rvert \le 30$	8.4	2.012	0.866	0.865	0.971	0.887	0.068	1.675	5.70 ± 0.40
7.2– 9.6	$150 \le \lvert\phi\rvert \le 180$	8.2	2.299	0.716	0.781	−0.977	0.910	0.043	1.631	4.39 ± 0.36
9.6–12.0	$0 \le \lvert\phi\rvert \le 30$	10.7	1.975	0.883	0.874	0.983	0.933	0.085	1.684	4.88 ± 0.40
9.6–12.0	$150 \le \lvert\phi\rvert \le 180$	10.8	2.351	0.685	0.761	−0.988	0.953	0.059	1.623	2.99 ± 0.31
12.0–14.4	$0 \le \lvert\phi\rvert \le 30$	13.0	1.939	0.903	0.881	0.990	0.959	0.103	1.691	3.57 ± 0.37
12.0–14.4	$150 \le \lvert\phi\rvert \le 180$	13.1	2.397	0.661	0.741	−0.994	0.977	0.078	1.615	2.31 ± 0.31
14.4–16.8	$0 \le \lvert\phi\rvert \le 30$	15.5	1.901	0.923	0.888	0.994	0.976	0.126	1.702	3.86 ± 0.44
14.4–16.8	$150 \le \lvert\phi\rvert \le 180$	15.4	2.437	0.635	0.723	−0.996	0.984	0.103	1.610	1.84 ± 0.34
16.8–19.2	$0 \le \lvert\phi\rvert \le 30$	17.8	1.866	0.941	0.894	0.997	0.987	0.149	1.709	2.61 ± 0.41
16.8–19.2	$150 \le \lvert\phi\rvert \le 180$	17.6	2.470	0.625	0.707	−0.998	0.991	0.132	1.604	0.90 ± 0.34
19.2–21.6	$0 \le \lvert\phi\rvert \le 30$	20.3	1.826	0.951	0.902	0.996	0.984	0.174	1.722	2.14 ± 0.43
21.6–24.0	$0 \le \lvert\phi\rvert \le 30$	22.4	1.797	0.961	0.906	0.999	0.994	0.194	1.728	2.57 ± 0.60
24.0–31.2	$0 \le \lvert\phi\rvert \le 30$	26.1	1.747	0.991	0.913	0.999	0.996	0.243	1.745	1.95 ± 0.75

plied this work to coincidence experiments. They defined energy apertures for two detected particles and averaged the radiative corrections for the larger aperture over the other aperture. The BU calculation also averages over the effects of the angular apertures for the two particles; these effects were insignificant for this experiment.

In our case the pion-energy aperture was dominant and the resulting δ was averaged over the aperture in scattered electron energy E' (or in c.m. energy W). The averaging was done for a fixed missing-mass cut, rather than for a fixed pion-energy cutoff, since this corresponded to our method of data reduction. This kind of cut meant in practice that there was very little variation of δ across the E' aperture.

Radiation from interactions of the incident or scattered electrons with other nuclei in the target and windows also results in a significant correction; it is similar to δ and can be combined with it. In this case radiation from the hadrons is unimportant since their masses make their radiation lengths very long. This target bremsstrahlung correction is discussed for single-particle experiments by Mo and Tsai [44]; their results were used for our experiment by making the appropriate kinematic substitutions.

The radiative correction is slightly affected by the momentum resolution of the apparatus. Values for δ were adjusted by folding the radiative tail with a Gaussian resolution function.

Our missing-mass-squared cutoff of 0.12 GeV^2 above the center of the neutron peak resulted in a correction $(1+\delta)^{-1}$ to the cross sections of about

TABLE VI *(Continued)*

Bins		Kinematic averages							Results	
θ (deg)	ϕ (deg)	θ (deg)	W (GeV)	$-k^2$ (GeV^2)	ϵ	cosϕ	cos2ϕ	$-t$ (GeV^2)	Correction factor	$\frac{d\sigma}{d\Omega_\pi}\left(\frac{\mu b}{sr}\right)$
					(l) Data point 10					
0.0– 1.2	$0\leq\|\phi\|\leq180$	0.78	2.311	0.354	0.818	0.025	0.024	0.006	1.811	8.26 ± 0.78
1.2– 2.4	$0\leq\|\phi\|\leq60$	1.82	2.273	0.363	0.831	0.846	0.474	0.008	1.816	9.79 ± 0.84
1.2– 2.4	$0\leq\|\phi\|\leq30$	1.83	2.268	0.362	0.833	0.952	0.815	0.008	1.816	10.62 ± 1.20
1.2– 2.4	$120\leq\|\phi\|\leq180$	1.80	2.348	0.343	0.803	−0.864	0.533	0.006	1.802	5.42 ± 0.68
1.2– 2.4	$150\leq\|\phi\|\leq180$	1.80	2.355	0.345	0.800	−0.966	0.869	0.006	1.800	6.19 ± 1.01
1.2– 2.4	$60\leq\phi\leq120$	1.80	2.304	0.355	0.820	0.046	−0.834	0.007	1.811	7.01 ± 1.12
1.2– 2.4	$-60\leq\phi\leq-120$	1.75	2.312	0.356	0.817	0.057	−0.816	0.007	1.811	7.98 ± 1.48
2.4– 3.6	$0\leq\|\phi\|\leq60$	3.03	2.244	0.370	0.841	0.887	0.607	0.010	1.822	8.20 ± 0.66
2.4– 3.6	$0\leq\|\phi\|\leq30$	3.03	2.238	0.371	0.843	0.960	0.848	0.010	1.822	8.93 ± 0.86
2.4– 3.6	$120\leq\|\phi\|\leq180$	2.98	2.367	0.329	0.797	−0.836	0.448	0.008	1.799	4.17 ± 0.59
2.4– 3.6	$150\leq\|\phi\|\leq180$	3.01	2.377	0.328	0.793	−0.968	0.877	0.008	1.797	3.34 ± 0.66
2.4– 3.6	$60\leq\phi\leq120$	2.99	2.314	0.348	0.817	−0.009	−0.833	0.008	1.811	6.75 ± 1.19
2.4– 3.6	$-60\leq\phi\leq-120$	2.84	2.285	0.364	0.827	0.284	−0.833	0.009	1.813	4.31 ± 1.70
3.6– 4.8	$0\leq\|\phi\|\leq60$	4.21	2.217	0.376	0.850	0.917	0.702	0.013	1.827	9.63 ± 0.66
3.6– 4.8	$0\leq\|\phi\|\leq30$	4.22	2.212	0.378	0.852	0.961	0.850	0.013	1.827	10.45 ± 0.80
3.6– 4.8	$120\leq\|\phi\|\leq180$	4.27	2.394	0.324	0.785	−0.916	0.703	0.010	1.791	5.14 ± 0.84
3.6– 4.8	$150\leq\|\phi\|\leq180$	4.24	2.396	0.322	0.785	−0.963	0.858	0.010	1.791	5.25 ± 0.97
3.6– 4.8	$60\leq\phi\leq120$	3.89	2.282	0.358	0.828	0.159	−0.753	0.011	1.813	8.03 ± 2.88
4.8– 6.0	$0\leq\|\phi\|\leq60$	5.40	2.192	0.383	0.858	0.933	0.754	0.017	1.832	9.14 ± 0.62
4.8– 6.0	$0\leq\|\phi\|\leq30$	5.43	2.187	0.384	0.859	0.962	0.852	0.017	1.832	8.96 ± 0.68
6.0– 7.2	$0\leq\|\phi\|\leq60$	6.58	2.166	0.391	0.865	0.958	0.840	0.021	1.837	8.56 ± 0.59
6.0– 7.2	$0\leq\|\phi\|\leq30$	6.61	2.164	0.392	0.866	0.967	0.872	0.021	1.837	8.54 ± 0.61
7.2– 8.4	$0\leq\|\phi\|\leq30$	7.77	2.137	0.398	0.873	0.972	0.892	0.026	1.843	7.65 ± 0.55
8.4– 9.6	$0\leq\|\phi\|\leq30$	9.02	2.110	0.406	0.880	0.979	0.917	0.032	1.846	7.81 ± 0.57
9.6–10.8	$0\leq\|\phi\|\leq30$	10.22	2.084	0.413	0.887	0.981	0.927	0.038	1.851	8.46 ± 0.61
10.8–12.0	$0\leq\|\phi\|\leq30$	11.41	2.059	0.418	0.892	0.987	0.947	0.044	1.845	7.86 ± 0.59
12.0–13.2	$0\leq\|\phi\|\leq30$	12.60	2.036	0.425	0.897	0.989	0.959	0.051	1.813	6.07 ± 0.54
13.2–14.4	$0\leq\|\phi\|\leq30$	13.84	2.011	0.430	0.903	0.991	0.965	0.058	1.799	4.98 ± 0.52
14.4–15.6	$0\leq\|\phi\|\leq30$	15.04	1.989	0.438	0.907	0.994	0.975	0.066	1.783	3.92 ± 0.52
15.6–16.8	$0\leq\|\phi\|\leq30$	16.26	1.963	0.444	0.912	0.996	0.983	0.073	1.771	3.47 ± 0.53
16.8–18.0	$0\leq\|\phi\|\leq30$	17.42	1.938	0.448	0.917	0.997	0.990	0.081	1.781	3.28 ± 0.55
18.0–19.2	$0\leq\|\phi\|\leq30$	18.47	1.925	0.462	0.919	0.997	0.987	0.089	1.775	2.70 ± 0.57
19.2–20.4	$0\leq\|\phi\|\leq30$	19.87	1.895	0.456	0.925	0.998	0.992	0.098	1.775	3.39 ± 0.62
20.4–21.6	$0\leq\|\phi\|\leq30$	20.90	1.877	0.463	0.928	0.998	0.991	0.105	1.774	3.44 ± 0.67

1.4; roughly 1.3 for radiation and 1.1 for target bremsstrahlung. The inclusion of hadron radiation had an effect of about 12% on δ and about 5% on σ.

An independent calculation from the Meister-Yennie formulas gave δ's smaller by about 10%, with about half the hadron part of the BU δ. Since this calculation certainly makes some bad approximations, we assigned a generous systematic error due to the radiative corrections of half of the difference between calculations, or about 2% of σ.

Kinematic effects from the radiated photon energy and from terms in the matrix elements proportional to this energy (non-infrared-divergent photons associated with particles having spin) have a negligible effect on our results. They have been estimated, using approximate formulas from Meister and Yennie, to result in errors in σ and the radiative tail shape of less than 1%.

H. Other Effects

No correction was made for ep events misidentified as $e\pi$ events. This effect was $\lesssim$0.3% in the

TABLE VI *(Continued)*

Bins		Kinematic averages							Results	
θ (deg)	ϕ (deg)	θ (deg)	W (GeV)	$-k^2$ (GeV^2)	ϵ	cosϕ	cos2ϕ	$-t$ (GeV^2)	Correction factor	$\frac{d\sigma}{d\Omega_\pi}\left(\frac{\mu b}{sr}\right)$
				(m) Data point 11						
0.0– 1.2	0≤|ϕ|≤180	0.81	2.020	0.426	0.901	−0.053	0.056	0.015	1.772	11.06 ± 0.90
1.2– 2.4	0≤|ϕ|≤ 60	1.85	1.991	0.434	0.907	0.838	0.449	0.017	1.780	12.18 ± 1.03
1.2– 2.4	0≤|ϕ|≤30	1.86	1.986	0.433	0.908	0.951	0.812	0.017	1.780	14.14 ± 1.62
1.2– 2.4	120≤|ϕ|≤180	1.84	2.048	0.423	0.895	−0.831	0.427	0.014	1.766	10.00 ± 0.83
1.2– 2.4	150≤|ϕ|≤180	1.85	2.052	0.421	0.894	−0.953	0.821	0.014	1.764	10.51 ± 1.16
1.2– 2.4	60≤ ϕ ≤120	1.86	2.020	0.429	0.901	0.009	−0.807	0.016	1.772	12.48 ± 1.49
1.2– 2.4	−60≤ ϕ ≤−120	1.91	2.019	0.428	0.901	0.030	−0.803	0.016	1.772	9.87 ± 1.26
2.4– 3.6	0≤|ϕ|≤60	3.04	1.975	0.437	0.910	0.849	0.482	0.019	1.785	12.34 ± 0.86
2.4– 3.6	0≤|ϕ|≤30	3.05	1.970	0.440	0.911	0.952	0.815	0.019	1.786	12.34 ± 1.14
2.4– 3.6	120≤|ϕ|≤180	3.02	2.066	0.415	0.891	−0.827	0.413	0.015	1.760	9.24 ± 0.63
2.4– 3.6	150≤|ϕ|≤180	3.05	2.074	0.416	0.889	−0.952	0.815	0.015	1.758	8.61 ± 0.81
2.4– 3.6	60≤ ϕ ≤120	3.01	2.023	0.428	0.900	0.001	−0.802	0.017	1.772	10.92 ± 1.22
2.4– 3.6	−60≤ ϕ ≤−120	2.99	2.022	0.430	0.900	−0.005	−0.786	0.017	1.772	8.86 ± 1.19
3.6– 4.8	0≤|ϕ|≤60	4.22	1.957	0.444	0.914	0.873	0.561	0.022	1.788	11.62 ± 0.77
3.6– 4.8	0≤|ϕ|≤30	4.23	1.949	0.446	0.915	0.962	0.853	0.022	1.788	11.59 ± 0.98
3.6– 4.8	120≤|ϕ|≤180	4.20	2.087	0.408	0.886	−0.852	0.491	0.016	1.754	8.98 ± 0.56
3.6– 4.8	150≤|ϕ|≤180	4.22	2.095	0.406	0.884	−0.962	0.853	0.016	1.752	8.06 ± 0.67
3.6– 4.8	60≤ ϕ ≤120	4.11	2.023	0.425	0.900	−0.020	−0.785	0.018	1.769	9.77 ± 1.20
3.6– 4.8	−60≤ ϕ ≤−120	4.14	2.025	0.427	0.900	−0.023	−0.791	0.019	1.770	12.41 ± 1.73
4.8– 6.0	0≤|ϕ|≤60	5.37	1.935	0.450	0.917	0.911	0.682	0.025	1.796	10.63 ± 0.77
4.8– 6.0	0≤|ϕ|≤30	5.39	1.930	0.450	0.919	0.959	0.844	0.026	1.797	11.07 ± 0.92
4.8– 6.0	120≤|ϕ|≤180	5.40	2.111	0.406	0.880	−0.877	0.570	0.018	1.747	7.83 ± 0.49
4.8– 6.0	150≤|ϕ|≤180	5.43	2.119	0.404	0.877	−0.955	0.827	0.018	1.747	8.05 ± 0.63
6.0– 7.2	0≤|ϕ|≤60	6.59	1.917	0.457	0.920	0.938	0.768	0.030	1.804	10.37 ± 0.83
6.0– 7.2	0≤|ϕ|≤30	6.60	1.913	0.457	0.921	0.963	0.856	0.030	1.804	9.67 ± 0.85
6.0– 7.2	120≤|ϕ|≤180	6.57	2.135	0.400	0.873	−0.902	0.653	0.021	1.743	6.55 ± 0.44
6.0– 7.2	150≤|ϕ|≤180	6.57	2.141	0.397	0.872	−0.958	0.837	0.021	1.741	6.41 ± 0.49
7.2– 8.4	0≤|ϕ|≤30	7.74	1.890	0.457	0.926	0.970	0.883	0.034	1.814	9.94 ± 0.89
7.2– 8.4	150≤|ϕ|≤180	7.78	2.163	0.389	0.866	−0.964	0.861	0.025	1.735	5.65 ± 0.45
8.4– 9.6	0≤|ϕ|≤30	8.92	1.872	0.467	0.928	0.977	0.910	0.039	1.819	7.80 ± 0.85
8.4– 9.6	150≤|ϕ|≤180	9.01	2.190	0.385	0.858	−0.963	0.856	0.031	1.729	5.01 ± 0.41
9.6–10.8	0≤|ϕ|≤30	10.18	1.851	0.469	0.931	0.985	0.941	0.045	1.827	9.24 ± 0.97
9.6–10.8	150≤|ϕ|≤180	10.19	2.212	0.376	0.851	−0.970	0.886	0.037	1.723	5.20 ± 0.43
10.8–12.0	0≤|ϕ|≤30	11.38	1.831	0.475	0.934	0.988	0.952	0.051	1.832	6.23 ± 0.88
10.8–12.0	150≤|ϕ|≤180	11.41	2.240	0.374	0.842	−0.978	0.913	0.045	1.717	4.86 ± 0.43
12.0–13.2	150≤|ϕ|≤180	12.61	2.269	0.365	0.832	−0.983	0.934	0.054	1.713	3.39 ± 0.36
13.2–14.4	150≤|ϕ|≤180	13.70	2.291	0.361	0.825	−0.987	0.949	0.063	1.707	2.63 ± 0.34
14.4–15.6	150≤|ϕ|≤180	14.96	2.321	0.349	0.814	−0.991	0.965	0.076	1.703	3.51 ± 0.41
15.6–16.8	150≤|ϕ|≤180	16.13	2.349	0.348	0.802	−0.992	0.969	0.089	1.695	2.29 ± 0.36

worst case. Events due to bremsstrahlung in the target followed by photoproduction and elastic electron scattering constitute only a small background and show up with the wrong missing mass.

I. Summary of Corrections and Systematic Uncertainties

Table IV summarizes all those corrections which were applied as over-all factors for each data point. These include magnet pole scattering, absorption without misidentification, and resolution. Table V summarizes typical values of corrections which had to be applied on a bin-by-bin basis.

Several bins at points 3a and 5 and a few at point 10 had large corrections for $\pi\pi$ contamination with uncertainties of up to 2–3%. The other largest systematic uncertainties are due to radiation (≈2%), magnet-pole scattering (1.0–2.0%), Faraday-cup efficiency (1.3%), integrator calibration (1.0%), and the trigger normalization (0.7–1.0%). Other sources of uncertainties which could be 0.5% or greater are the misidentification of π's as p's (0.3–0.9%), decay in flight (0.2–0.7%), good events lost due to target cuts (0.5%), absorption losses (0.5–0.6%), Monte Carlo acceptance (0.5%), missing-mass resolution (0.5%), target length (0.5%), and target-empty rates (0.2–0.5%). Two uncertainties of less than 1% arise from uncertainties in the kinematic variables for which cross sections are quoted. These result from the energy and momentum calibrations, and from the use of nonzero bin sizes.

TABLE VI *(Continued)*

Bins		Kinematic averages							Results	
θ (deg)	ϕ (deg)	θ (deg)	W (GeV)	$-k^2$ (GeV^2)	ϵ	cosϕ	cos2ϕ	$-t$ (GeV^2)	Correction factor	$\frac{d\sigma}{d\Omega_\pi}\left(\frac{\mu b}{sr}\right)$
				(n) Data point 12						
0– 1.2	0≤|ϕ|≤180	0.7	2.152	1.188	0.788			0.065	1.583	3.82 ± 0.54
1.2– 2.4	0≤|ϕ|≤60	1.8	2.122	1.202	0.797	0.890	0.612	0.070	1.588	2.89 ± 0.49
1.2– 2.4	0≤|ϕ|≤30	1.7	2.121	1.202	0.798	0.949	0.803	0.070	1.588	4.22 ± 0.84
1.2– 2.4	120≤|ϕ|≤180	1.8	2.177	1.170	0.780	−0.819	0.391	0.061	1.582	3.32 ± 0.52
1.2– 2.4	150≤|ϕ|≤180	1.8	2.180	1.166	0.779	−0.962	0.853	0.060	1.582	3.08 ± 0.70
1.2– 2.4	60≤|ϕ|≤120	1.9	2.153	1.191	0.787	0.018	−0.829	0.066	1.584	4.10 ± 0.68
2.4– 3.6	0≤|ϕ|≤60	3.0	2.110	1.226	0.799	0.847	0.477	0.076	1.590	3.50 ± 0.46
2.4– 3.6	0≤|ϕ|≤30	3.0	2.106	1.228	0.800	0.953	0.820	0.077	1.590	3.47 ± 0.60
2.4– 3.6	120≤|ϕ|≤180	3.0	2.196	1.150	0.774	−0.842	0.453	0.059	1.578	3.53 ± 0.49
2.4– 3.6	150≤|ϕ|≤180	3.0	2.202	1.150	0.772	−0.945	0.789	0.059	1.578	3.31 ± 0.63
2.4– 3.6	60≤|ϕ|≤120	3.0	2.147	1.192	0.789	0.047	−0.801	0.068	1.584	3.25 ± 0.55
3.6– 4.8	0≤|ϕ|≤60	4.2	2.090	1.237	0.805	0.899	0.647	0.083	1.593	4.55 ± 0.49
3.6– 4.8	0≤|ϕ|≤30	4.2	2.085	1.240	0.807	0.965	0.867	0.084	1.593	5.11 ± 0.67
3.6– 4.8	120≤|ϕ|≤180	4.3	2.219	1.138	0.766	−0.903	0.653	0.059	1.576	3.83 ± 0.46
3.6– 4.8	150≤|ϕ|≤180	4.3	2.223	1.135	0.765	−0.957	0.835	0.059	1.576	4.22 ± 0.60
3.6– 4.8	60≤|ϕ|≤120	4.0	2.148	1.197	0.787	0.067	−0.830	0.071	1.584	4.39 ± 0.86
4.8– 7.2	0≤|ϕ|≤60	5.9	2.063	1.259	0.812	0.914	0.687	0.095	1.595	3.73 ± 0.32
4.8– 7.2	0≤|ϕ|≤30	6.0	2.057	1.262	0.814	0.958	0.840	0.096	1.595	3.48 ± 0.35
4.8– 7.2	120≤|ϕ|≤180	6.0	2.250	1.111	0.756	−0.939	0.772	0.061	1.569	3.44 ± 0.31
4.8– 7.2	150≤|ϕ|≤180	6.0	2.253	1.111	0.755	−0.963	0.857	0.061	1.569	3.52 ± 0.36
7.2– 9.6	0≤|ϕ|≤30	8.4	2.019	1.292	0.823	0.976	0.907	0.116	1.601	3.06 ± 0.32
7.2– 9.6	150≤|ϕ|≤180	8.6	2.297	1.069	0.739	−0.981	0.925	0.068	1.564	2.99 ± 0.31
9.6–12.0	0≤|ϕ|≤30	10.7	1.980	1.322	0.832	0.982	0.928	0.139	1.606	2.14 ± 0.29
9.6–12.0	150≤|ϕ|≤180	10.8	2.341	1.031	0.723	−0.985	0.941	0.080	1.557	2.09 ± 0.28
12.0–14.4	0≤|ϕ|≤30	13.1	1.946	1.349	0.840	0.991	0.965	0.165	1.612	1.76 ± 0.27
12.0–14.4	150≤|ϕ|≤180	13.2	2.391	0.995	0.701	−0.995	0.979	0.099	1.551	1.97 ± 0.29
14.4–16.8	0≤|ϕ|≤30	15.4	1.912	1.364	0.848	0.992	0.970	0.191	1.620	1.47 ± 0.28
14.4–16.8	150≤|ϕ|≤180	15.8	2.439	0.995	0.680	−0.997	0.987	0.128	1.545	1.19 ± 0.26
16.8–19.2	0≤|ϕ|≤30	17.9	1.875	1.396	0.854	0.995	0.979	0.225	1.624	1.88 ± 0.36
16.8–19.2	150≤|ϕ|≤180	18.0	2.481	0.902	0.662	−0.998	0.992	0.157	1.537	0.69 ± 0.23
19.2–21.6	0≤|ϕ|≤30	20.3	1.836	1.430	0.861	0.997	0.989	0.263	1.634	2.34 ± 0.44
19.2–21.6	150≤|ϕ|≤180	20.3	2.517	0.861	0.644	−0.999	0.997	0.195	1.530	1.06 ± 0.43
21.6–24.0	0≤|ϕ|≤30	22.6	1.805	1.437	0.868	0.998	0.999	0.295	1.641	1.17 ± 0.38
24.0–28.0	0≤|ϕ|≤30	27.4	1.735	1.486	0.879	0.993	0.995	0.378	1.660	1.20 ± 0.32

A conservative estimate of the over-all systematic uncertainty is ≈5–6% for most bins. Most of the possible errors are the same for all data points and all bins and thus do not affect the shapes of the distributions presented below. Others, such as errors in the corrections for π decay and π misidentification as p, are bin-dependent but probably not point-dependent. Only a few possible errors, such as those due to magnet-pole scattering, $\pi\pi$ contamination, and bin sizes, are likely to vary significantly from point to point and bin to bin.

IX. RESULTS

A. Cross Sections

Tables VI(a) through VI(n) summarize the corrected center-of-mass virtual-photoproduction cross sections. The kinematic averages were determined by weighting the relevant parameters with the measured cross sections. In the section that follows, these cross sections will be interpolated to obtain cross sections with fixed values of k^2, ϵ, and W, and will be compared with Berends' theory. The k^2 dependence of the data will be used to determine the pion form factor.

B. Angular Distributions

The tabulated virtual-photoproduction cross sections are spread over an extended region of kinematic parameters. Figure 16 illustrates the region covered by three of the five angular distribution data points. This is a plot of W versus the horizontal projection of θ. As was pointed out in Sec. III, ϵ and to a lesser extent k^2 are highly correlated with W. These correlations are approximately the same for all data points of the angular scan, because the beam energy and electron-arm angle are approximately the same for all. Thus W in Fig. 16 represents the parameter set (W, k^2, ϵ).

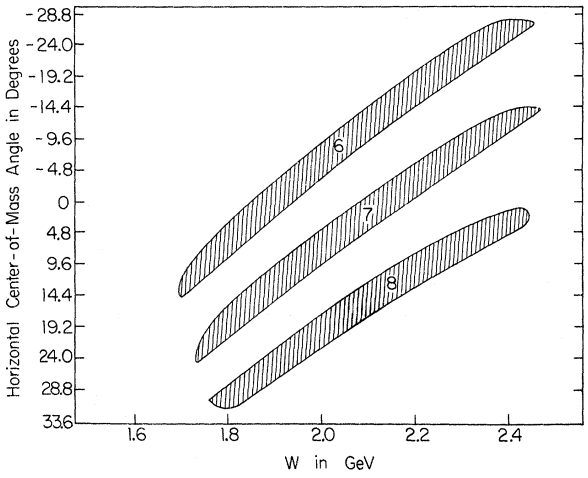

FIG. 16. A diagram showing the correlation between the projection of the center-of-mass polar angle θ on the electron scattering plane and the total center-of-mass energy W for angular scan data points 6, 7, and 8.

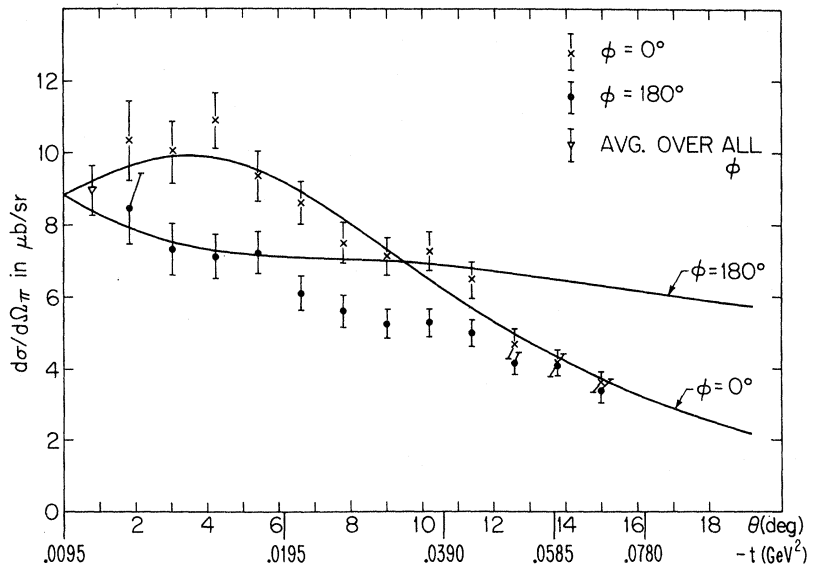

FIG. 17. A plot of the interpolated $\phi = 0°$ and $\phi = 180°$ center-of-mass virtual-photoproduction cross sections for $W = 2.15$ GeV, $k^2 = -0.396$ GeV^2 and $\epsilon = 0.87$ versus θ and t. The solid curves are Berends' theory with $F_\pi = F_1^V = 0.566$. The uncertainties include only the statistical errors.

TABLE VII. The π^+n center-of-mass virtual-photoproduction cross sections (in μb/sr) for $\phi = 0$ and $\phi = 180°$ and the angular distribution for the transverse-scalar interference term, D (in μb/sr). Values at $\theta = 0.8°$ are averages over all ϕ. The uncertainties are statistical only.

W (GeV)		2.15			2.31			2.02		1.91
k^2 (GeV^2)		−0.396			−0.354			−0.426		−0.451
ϵ		0.870			0.818			0.901		0.922
θ (deg)	$d\sigma/d\Omega_\pi$ $\phi = 0$	$d\sigma/d\Omega_\pi$ $\phi = 180°$	D	$d\sigma/d\Omega_\pi$ $\phi = 0$	$d\sigma/d\Omega_\pi$ $\phi = 180°$	D	$d\sigma/d\Omega_\pi$ $\phi = 0$	$d\sigma/d\Omega_\pi$ $\phi = 180°$	D	$d\sigma/d\Omega_\pi$ $\phi = 0$
0.8		8.97 ± 0.68			8.25 ± 0.78			11.05 ± 0.91		11.04 ± 0.99
1.8	10.38 ± 1.09	8.50 ± 1.00	1.03 ± 0.85	9.72 ± 1.04	6.58 ± 0.99	1.83 ± 0.86	13.15 ± 1.47	10.07 ± 1.17	1.67 ± 1.05	11.80 ± 1.54
3.0	10.09 ± 0.84	7.37 ± 0.73	1.50 ± 0.64	8.72 ± 0.72	4.53 ± 0.67	2.43 ± 0.58	11.75 ± 1.02	9.20 ± 0.86	1.38 ± 0.74	11.43 ± 1.17
4.2	10.93 ± 0.79	7.18 ± 0.62	2.07 ± 0.57	9.09 ± 0.61	5.59 ± 0.74	2.03 ± 0.57	11.57 ± 0.86	8.95 ± 0.72	1.42 ± 0.62	10.99 ± 0.99
5.4	9.39 ± 0.68	7.30 ± 0.59	1.14 ± 0.31	7.46 ± 0.47	4.12 ± 0.50	1.94 ± 0.41	10.76 ± 0.74	8.18 ± 0.60	1.39 ± 0.53	10.83 ± 0.92
6.6	8.65 ± 0.61	6.18 ± 0.49	1.37 ± 0.44	7.43 ± 0.40	4.68 ± 0.45	1.60 ± 0.36	9.86 ± 0.66	7.57 ± 0.52	1.23 ± 0.46	9.67 ± 0.85
7.8	7.54 ± 0.56	5.68 ± 0.45	1.02 ± 0.40	6.98 ± 0.38	4.53 ± 0.43	1.43 ± 0.34	8.60 ± 0.61	7.04 ± 0.44	0.85 ± 0.42	9.76 ± 0.85
9.0	7.18 ± 0.55	5.32 ± 0.41	1.02 ± 0.39	4.81 ± 0.47	4.34 ± 0.44	0.27 ± 0.38	9.14 ± 0.64	6.75 ± 0.41	1.30 ± 0.42	8.45 ± 0.79
10.2	7.31 ± 0.53	5.35 ± 0.39	1.08 ± 0.37		4.10 ± 0.44		8.06 ± 0.61			8.41 ± 0.77
11.4	6.48 ± 0.50	5.05 ± 0.37	0.79 ± 0.35		4.85 ± 0.53		7.50 ± 0.64			6.60 ± 0.71
12.6	4.69 ± 0.41	4.22 ± 0.31	0.26 ± 0.29		3.07 ± 0.37		6.08 ± 0.60			6.08 ± 0.66
13.8	4.16 ± 0.36	4.16 ± 0.30	0.00 ± 0.26		2.41 ± 0.35		4.93 ± 0.55			5.07 ± 0.62
15.0	3.38 ± 0.32	3.66 ± 0.28	−0.16 ± 0.24		3.52 ± 0.40		3.83 ± 0.50			4.58 ± 0.62
16.2					2.60 ± 0.33		3.65 ± 0.49			3.49 ± 0.59
17.4							3.33 ± 0.43			3.36 ± 0.61
18.6							2.99 ± 0.43			2.56 ± 0.56
19.8							2.24 ± 0.32			3.27 ± 0.59
21.0										3.17 ± 0.58

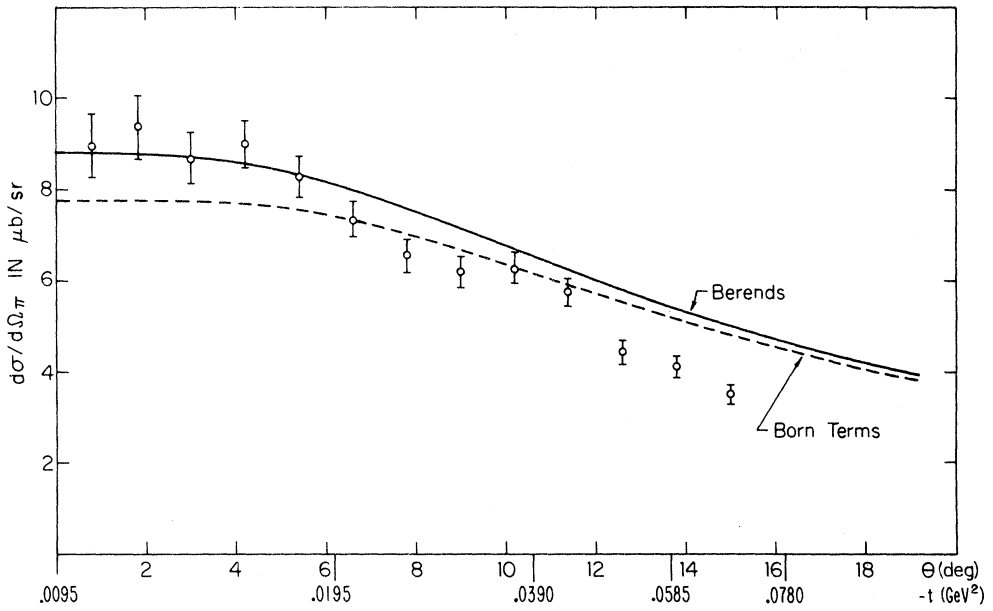

FIG. 18. A plot of the average of the $\phi = 0°$ and $\phi = 180°$ virtual-photoproduction cross section for $W = 2.15$ GeV, $k^2 = -0.396$ GeV^2 and $\epsilon = 0.87$ versus θ and t. This average is equal to $A + \epsilon B + \epsilon C$. The solid curve is Berends' theory with $F_\pi = F_1^V = 0.566$. The dashed curve is the generalized Born approximation with $F_\pi = F_1^V$. The uncertainties include only the statistical errors.

The data of Table VI could of course be compared directly with the predictions of any model. However, it is far more enlightening to combine these data in order to display detailed angular distributions with other parameters held constant. This may be done by interpolating cross sections in each θ-ϕ bin between parameter sets, effectively along horizontal lines in Fig. 16. The most significant change between the same θ-ϕ bin for adjacent data points is that in W. We have utilized a linear interpolation in W between adjacent data points (the order is 6, 10, 7, 11, 8). The spread of results for any plausible smooth interpolating curves is considerably smaller than the statistical

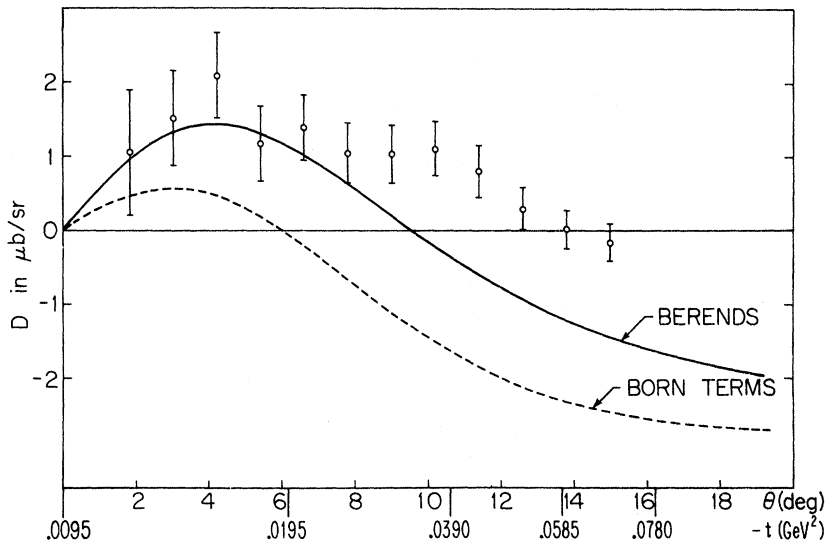

FIG. 19. A plot of the transverse-scalar interference term D for $W = 2.15$ GeV and $k^2 = -0.396$ GeV^2 versus θ and t. The solid curve is Berends' theory with $F_\pi = F_1^V = 0.566$. The dashed curve is the generalized Born approximation with $F_\pi = F_1^V$. The uncertainties include only the statistical errors.

uncertainties of the measured cross sections.

Angular distributions have been computed for four parameter sets: $(W, k^2, \epsilon) = (2.31, -0.354, 0.818)$, $(2.15, -0.396, 0.870)$, $(2.02, -0.426, 0.901)$, and $(1.91, -0.451, 0.922)$. (W is in GeV and k^2 is in GeV^2.) For the first of these, some data from data point 5 were used for several bins in which statistics are better than for point 6. (Points 5 and 6 were run under identical conditions except for nominal momenta. They are in statistical agreement in their region of overlap.) The four distributions are not entirely uncoupled, but collectively they are a fair representation of the data.

Whenever ϕ bins near both 0° and 180° were available for the same W, k^2, ϵ, and θ, we adjusted $\langle\cos\phi\rangle$ to ±1.0 in Eq. (10) so as to obtain the physically interesting $\phi = 0°$ and $\phi = 180°$ cross sections and the transverse-scalar interference term. It was also necessary to adjust $\langle\cos 2\phi\rangle$ to 1.0. We used only ±30° ϕ bins, for which $\langle\cos 2\phi\rangle$ is between 0.8 and 1.0; and carried out the adjustment by assuming the validity of Berends' model (with $F_\pi = F_1^V$) for term B of Eq. (10). The *largest* such adjustment was −0.08 μb/sr, which would be negligible even if it were wrong by a factor of 2. Thus our results remain model-independent.

Table VII presents the results, with statistical

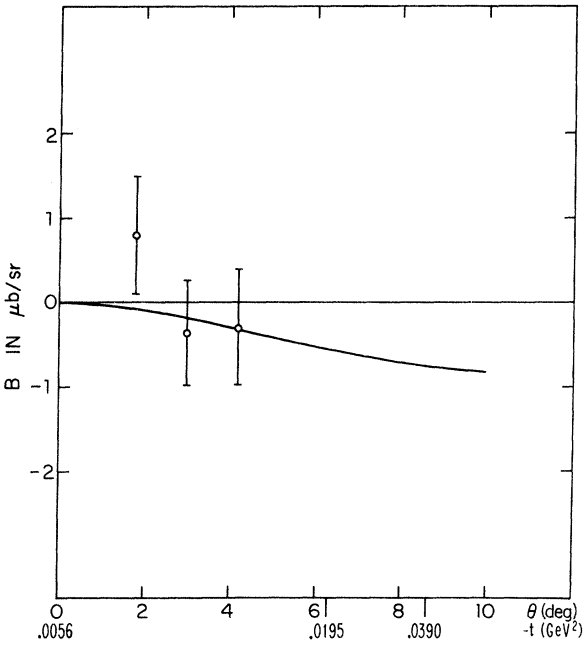

FIG. 20. A plot of the transverse-transverse interference term B for $W = 2.15$ GeV and $k^2 = -0.396$ GeV^2 versus θ and t. The solid curve is Berends' theory with $F_\pi = F_1^V = 0.566$. The uncertainties include only the statistical errors.

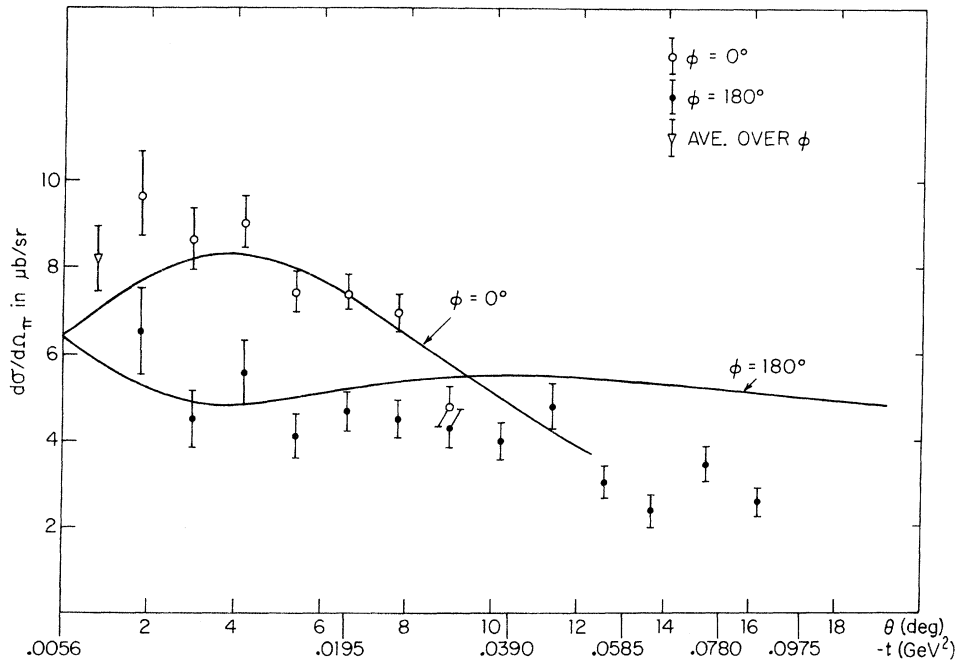

FIG. 21. A plot of the interpolated $\phi = 0°$ and $\phi = 180°$ center-of-mass virtual-photoproduction cross sections for $W = 2.31$ GeV, $k^2 = -0.354$ GeV^2 and $\epsilon = 0.818$ versus θ and t. The solid curves are Berends' theory with $F_\pi = F_1^V = 0.596$. The uncertainties include only the statistical errors.

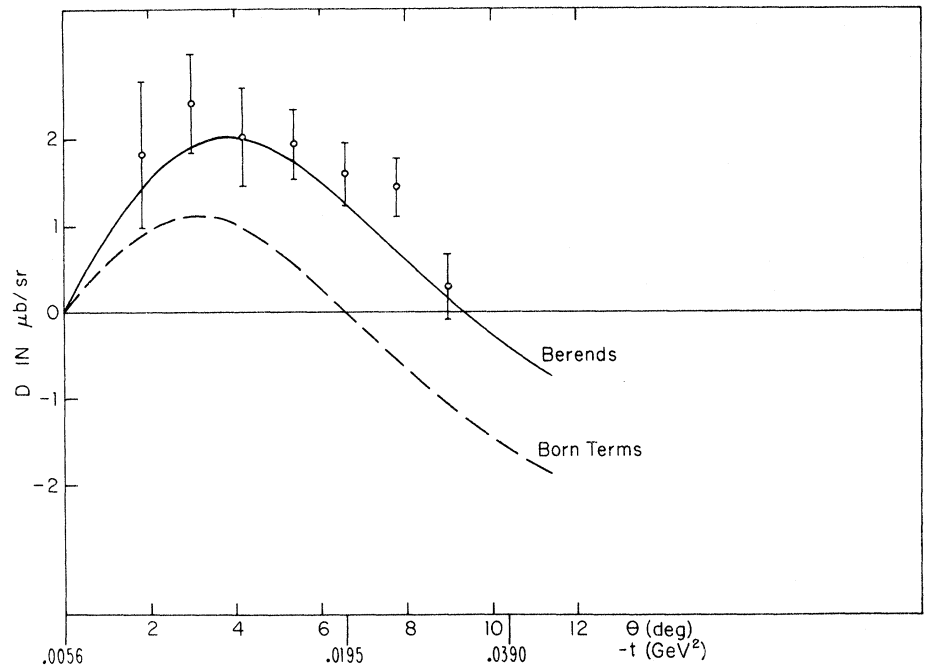

FIG. 22. A plot of the transverse-scalar interference term D for $W=2.31$ GeV and $k^2=-0.354$ GeV^2 versus θ and t. The solid curve is Berends' theory with $F_\pi=F_1^V=0.596$. The dashed curve is the generalized Born approximation with $F_\pi=F_1^V$. The uncertainties include only the statistical errors.

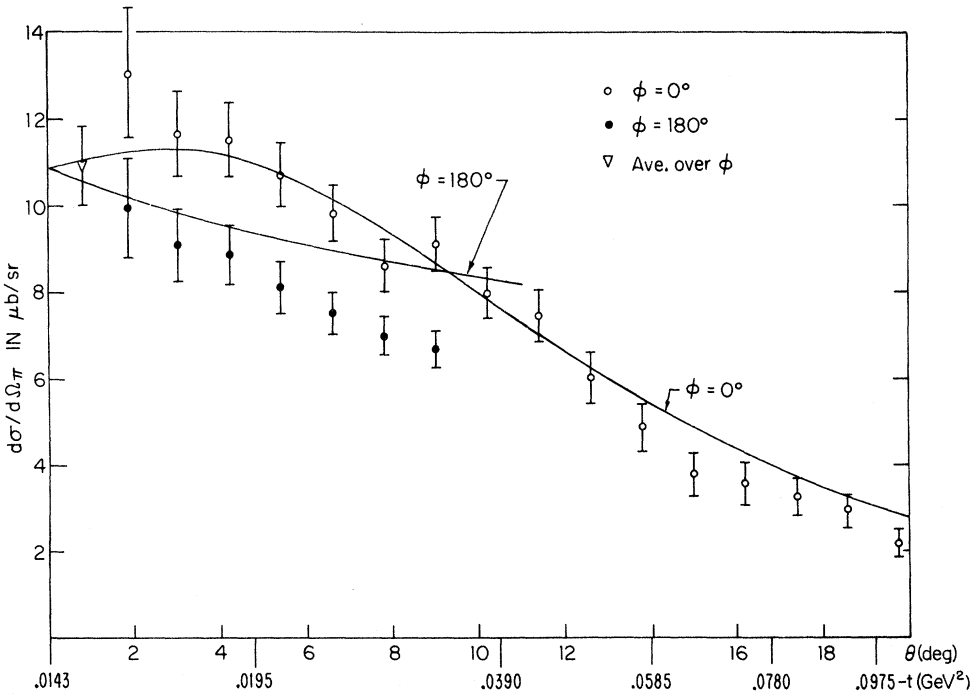

FIG. 23. A plot of the interpolated $\phi=0°$ and $\phi=180°$ center-of-mass virtual-photoproduction cross sections for $W=2.02$ GeV, $k^2=-0.426$ GeV^2, and $\epsilon=0.901$ versus θ and t. The solid curves are Berends' theory with $F_\pi=F_1^V=0.547$. The uncertainties include only the statistical errors.

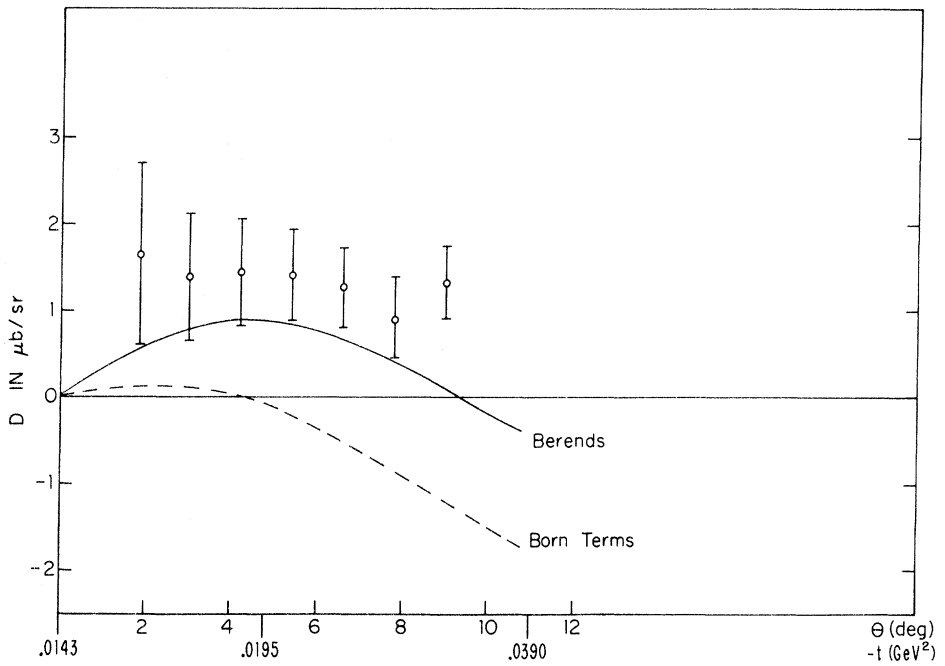

FIG. 24. A plot of the transverse-scalar interference term D for $W=2.02$ GeV and $k^2=-0.426$ GeV^2. The solid curve is Berends' theory with $F_\pi=F_1^V=0.547$. The dashed curve is the generalized Born approximation with $F_\pi=F_1^V$. The uncertainties include only the statistical errors.

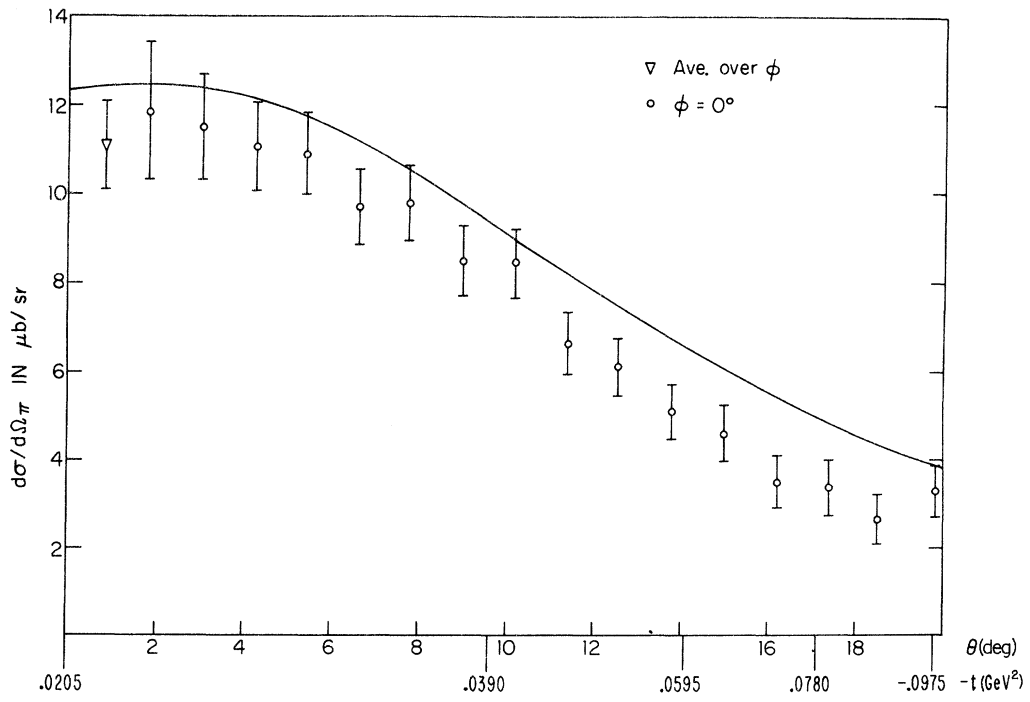

FIG. 25. A plot of the interpolated $\phi=0°$ center-of-mass virtual-photoproduction cross sections for $W=1.91$ GeV, $k^2=-0.451$ GeV^2 and $\epsilon=0.922$. The solid curve is Berends' theory with $F_\pi=F_1^V=0.531$. The uncertainties include only the statistical errors.

uncertainties. The adjustment of $\langle\cos 2\phi\rangle$ to 1.0 has been made even for unpaired bins (except for $W=1.91$ GeV). The adjustment of $\langle\cos\phi\rangle$ to ± 1.0 has not been made for these bins. However (except for $W=1.91$), unpaired values of $\langle\cos\phi\rangle$ are all within 0.02 of ± 1.0; so that the correction is almost certainly <0.04 μb/sr, and can safely be ignored.

C. Comparison of Angular Distributions to Berends' Predictions

If Berends' model is correct anywhere, it should be correct at small values of t. It is thus natural to adjust the value of F_π for a best fit to our small-t data. By successively trying to fit the data over wider ranges of θ, one can determine at what θ (and t) the model can no longer provide a reasonable fit. The fits have been made to the $\phi=0°$ and $\phi=180°$ cross sections from Table VII.

For the $W=2.15$-GeV distribution, Berends' model works well for $\theta \lesssim 6°$ ($-t \lesssim m_\pi^2$) if $F_\pi = 0.575 \pm 0.025$; χ^2 per degree of freedom is <0.5. This fit, and thus the model, begins to fail for larger θ, with the failure setting in first for $\phi=180°$ and becoming appreciable once $\theta \gtrsim 9°$. $F_\pi = F_1^V$ ($=0.566$ for $k^2=-0.396$ GeV^2) provides a fit nearly as good as the best fit.[36]

The generalized Born approximation alone does not provide any successful fit. (For θ up to 6°, χ^2 per degree of freedom is 2.8 at best.) The average of the $\phi=0°$ and $\phi=180°$ cross sections can be reproduced approximately; but any F_π which works reasonably well near $\theta=0°$ leads to a gross underestimation of the transverse-scalar interference term.

The same conclusions may be drawn for the $W=2.02$-GeV distribution. For the $W=2.31$-GeV distribution, no fit is really good in the small-angle region, but again $F_\pi = F_1^V$ is very close to the best fit. The angular distributions will not be used to deduce or check a functional form for

TABLE VIII. The measured and extrapolated cross sections (in μb/sr) for the central bins of the W scan. Berends' theory with $F_\pi = F_1^V$ was used to extrapolate the cross sections to a common value of ϵ. The uncertainties are statistical only.

W (GeV)	ϵ	$\frac{d\sigma}{d\Omega_\pi}$ (measured)	$\frac{d\sigma}{d\Omega_\pi}$ (scaled to $\epsilon=0.90$)	$\cos\phi$	$\cos 2\phi$
		$0 \le \theta \le 2.4°$, $k^2=-0.29$ GeV^2			
1.84	0.94	12.76 ± 0.83	12.32 ± 0.80	...	...
2.05	0.92	9.71 ± 0.61	9.59 ± 0.60	...	...
2.14	0.89	8.72 ± 0.35	8.81 ± 0.35	...	...
2.50	0.73	5.03 ± 0.17	5.66 ± 0.19	...	...
		$2.4° \le \theta \le 4.8°$, $\phi \approx 0$, $k^2=-0.30$ GeV^2			
1.79	0.95	14.41 ± 0.94	13.85 ± 0.90	0.83	0.44
1.98	0.93	11.83 ± 0.70	11.58 ± 0.69	0.84	0.47
2.07	0.91	11.34 ± 0.44	11.29 ± 0.44	0.86	0.55
2.41	0.78	7.98 ± 0.26	8.84 ± 0.29	0.87	0.60
		$2.4° \le \theta \le 4.8°$, $\phi \approx 180°$, $k^2=-0.28$ GeV^2			
1.90	0.94	10.61 ± 0.73	10.32 ± 0.71	−0.83	0.42
2.12	0.90	6.94 ± 0.55	6.94 ± 0.55	−0.83	0.41
2.22	0.86	5.65 ± 0.32	5.79 ± 0.33	−0.84	0.45
2.60	0.68	2.28 ± 0.15	2.70 ± 0.17	−0.88	0.58
		$4.8° \le \theta \le 9.6°$, $\phi \approx 0$, $k^2=-0.31$ GeV^2			
1.74	0.96	14.46 ± 0.68	13.83 ± 0.65	0.91	0.67
1.92	0.94	10.38 ± 0.47	10.08 ± 0.46	0.92	0.73
2.01	0.92	10.74 ± 0.32	10.49 ± 0.31	0.94	0.79
2.31	0.82	6.82 ± 0.30	7.43 ± 0.33	0.97	0.87
		$4.8° \le \theta \le 9.6°$, $\phi \approx 180°$, $k^2=-0.26$ GeV^2			
1.96	0.93	9.16 ± 0.44	8.97 ± 0.41	−0.90	0.63
2.20	0.88	4.40 ± 0.33	4.52 ± 0.34	−0.93	0.75
2.31	0.85	4.42 ± 0.24	4.61 ± 0.25	−0.94	0.78
2.71	0.61	1.92 ± 0.20	2.45 ± 0.26	−0.98	0.91

$F_\pi(k^2)$; the k^2 scan for $\theta = 0°$ is better equipped to do that. Hence, for simplicity, the following plots all display the theoretical predictions with $F_\pi = F_1^V$. All conclusions will be the same as if some "best fit" values were used.

Figure 17 shows the $\phi = 0°$ and $\phi = 180°$ cross sections for $W = 2.15$ GeV. The data in this and other angular distribution plots are (apart from the negligible $\langle \cos 2\phi \rangle$ adjustment) entirely model-independent. Figure 18 shows the average of these cross sections ($A + B\epsilon + C\epsilon$), while Fig. 19 shows the transverse-scalar interference term (D). Berends' model begins to fail for both of these at $t \approx -m_\pi^2$. The Born terms alone could (with an adjusted F_π) describe the average up to the same t; however, they cannot account at all for the observed interference term. Figure 19 is a clear demonstration of the improvements attainable by adding dispersion terms. Of course, it also shows that Berends' model does not go far enough. Perhaps the most mysterious feature of these plots is that Berends' model successfully describes the $\phi = 0°$ cross sections up to the largest θ (or $-t$) measured; but fails badly for the $\phi = 180°$ cross sections beyond $t = -m_\pi^2$.

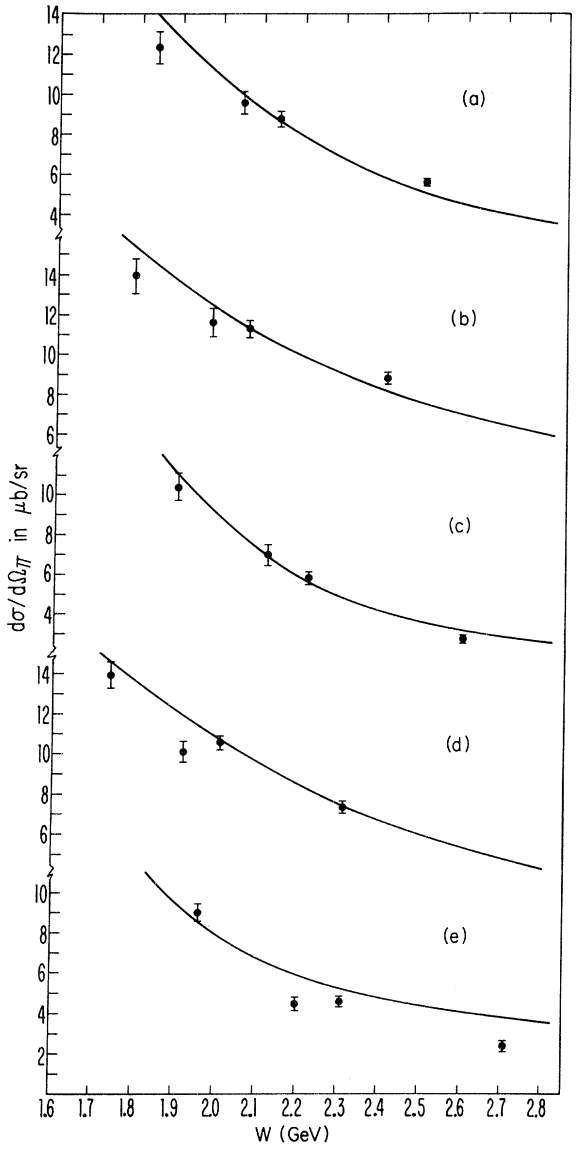

FIG. 26. W dependence of the virtual-photoproduction cross section. Berends' theory with $F_\pi = F_1^V$ has been used to extrapolate the measured cross sections to a common value of $\epsilon = 0.9$. The curves show the theory with $F_\pi = F_1^V$. (a) $0° \le \theta \le 2.4°$, $k^2 = -0.29$ GeV^2; (b) $2.4° \le \theta \le 4.8°$, $\phi \approx 0°$, $k^2 = -0.30$ GeV^2; (c) $2.4° \le \theta \le 4.8°$, $\phi \approx 180°$, $k^2 = -0.28$ GeV^2; (d) $4.8° \le \theta \le 9.6°$, $\phi \approx 0°$, $k^2 = -0.31$ GeV^2; (e) $4.8° \le \theta \le 9.6°$, $\phi \approx 180°$, $k^2 = -0.26$ GeV^2.

Figure 20 shows the transverse polarization term (B) for the same W. We can say little more than that there is no gross inconsistency with the theory.

Figure 21 shows the $\phi = 0°$ and $\phi = 180°$ cross sections and Fig. 22 shows the transverse-scalar interference term for $W = 2.31$ GeV. Figures 23 and 24 are the analogous plots for $W = 2.02$ GeV. The 2.02-GeV data support the same conclusions as those drawn from the 2.15-GeV data. At $W = 2.31$, the theory is low at the smallest θ, then works reasonably well out to $t \approx -m_\pi^2$, and finally fails in the same way as at the other W's.

Figure 25 shows a $\phi = 0°$ distribution for $W = 1.91$ GeV. The small $\langle \cos\phi \rangle$ and $\langle \cos 2\phi \rangle$ corrections have not been applied. Berends' model with $F_\pi = F_1^V$ predicts values that are somewhat high; this is even more striking in comparisons to photoproduction data near this W.

TABLE IX. The measured and extrapolated cross sections for the region $\theta \le 2.4°$ for the k^2 scan. The cross sections were calculated by averaging over bins 1, 2, 4, 6, and 7. Berends' theory with $F_\pi = F_1^V$ was used to extrapolate the cross sections to a common value of $\epsilon = 0.85$. For these data the mean W was 2.15 GeV. The uncertainties are statistical only.

$-k^2$ (GeV^2)	ϵ	$-t$ (GeV^2)	$\frac{d\sigma}{d\Omega_\pi}$ (μb/sr)	$\frac{d\sigma}{d\Omega_\pi}$ extrapolated
0.176	0.853	0.003	7.15 ± 0.34	7.14 ± 0.34
0.294	0.880	0.006	8.22 ± 0.45	8.05 ± 0.44
0.396	0.870	0.011	9.05 ± 0.35	8.90 ± 0.34
0.795	0.830	0.034	6.99 ± 0.37	7.13 ± 0.38
1.188	0.788	0.066	3.54 ± 0.28	3.77 ± 0.30

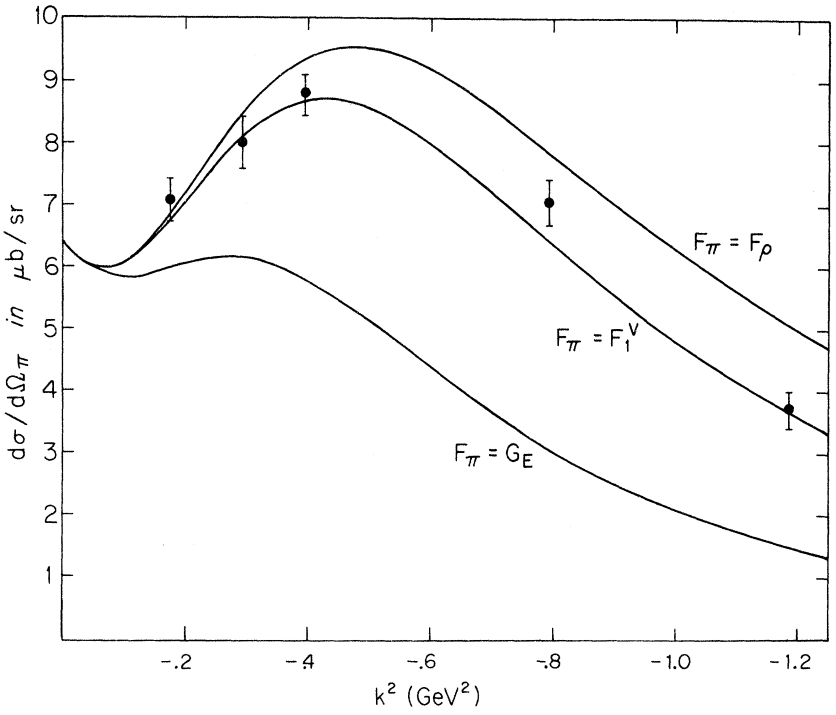

FIG. 27. The k^2 dependence of the forward virtual-photoproduction cross section for $W = 2.15$ GeV, $0° \leq \theta \leq 2.4°$, $0° \leq |\phi| \leq 180°$, and $\epsilon = 0.85$. Berends' theory with $F_\pi = F_1^V$ was used to extrapolate the measured cross sections to a common value of $\epsilon = 0.85$. The solid curves show the prediction of Berends' theory with $F_\pi = F_\rho$, F_1^V and G_E^p. The uncertainties include statistical errors only.

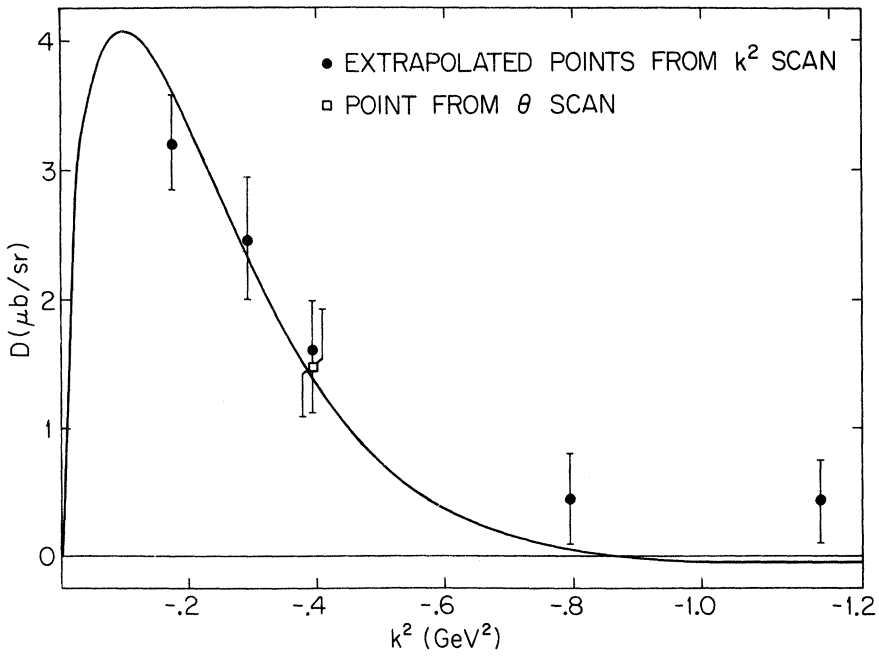

FIG. 28. The k^2 dependence of the transverse-scalar interference term D for $W = 2.15$ GeV and $2.4° \leq \theta \leq 4.8°$. Berends' theory with $F_\pi = F_1^V$ was used to extrapolate the measured cross sections to a common value of W and ϵ. The solid curve shows the prediction of Berends' theory with $F_\pi = F_1^V$. The uncertainties include the statistical errors only.

TABLE X. The determination of the transverse-scalar interference term, D, for the k^2 scan. The cross sections are given for the region $2.4° \leq \theta \leq 4.8°$. For each data point, the first line gives the average of bins 8 and 14, the second line gives the average of bins 10 and 16, and the third line gives the nominal values to which the adjustments were made. The uncertainties are statistical only.

Data Point	W (GeV)	k^2 (GeV^2)	ϵ	cosϕ	cos2ϕ	$\frac{d\sigma}{d\Omega_\pi}\left(\frac{\mu b}{sr}\right)$ Measured	Adjusted	$D\left(\frac{\mu b}{sr}\right)$
4	2.070	−0.189	0.878	0.885	0.600	10.21 ± 0.47	9.17 ± 0.41	
	2.226	−0.166	0.822	−0.820	0.392	3.47 ± 0.32	4.26 ± 0.39	
	2.150	−0.176	0.853					3.24 ± 0.37
3b	2.083	−0.308	0.896	0.863	0.526	11.46 ± 0.57	10.57 ± 0.53	
	2.224	−0.281	0.856	−0.841	0.456	5.41 ± 0.42	6.72 ± 0.51	
	2.150	−0.294	0.880					2.48 ± 0.48
7	2.088	−0.411	0.886	0.861	0.523	11.08 ± 0.44	10.28 ± 0.41	
	2.218	−0.379	0.850	−0.831	0.470	6.82 ± 0.34	7.92 ± 0.39	
	2.150	−0.396	0.870					1.62 ± 0.37
9	2.096	−0.825	0.844	0.876	0.576	6.48 ± 0.40	6.53 ± 0.40	
	2.203	−0.768	0.814	−0.842	0.464	5.72 ± 0.38	5.80 ± 0.38	
	2.150	−0.795	0.830					0.46 ± 0.36
12	2.110	−1.232	0.802	0.873	0.562	4.04 ± 0.34	4.23 ± 0.36	
	2.208	−1.144	0.770	−0.872	0.553	3.69 ± 0.33	3.59 ± 0.32	
	2.150	−1.188	0.788					0.43 ± 0.32

In all of these plots, error bars are statistical only. Most systematic uncertainties do not affect the *shapes* of the angular distributions; all points in one distribution are effectively at the same momenta. Shape uncertainties amount to only ≈2–2.5%. An over-all normalization uncertainty of ≈6% could imply an error of up to 3% (≈0.02) in the fit values of F_π.

To summarize, Berends' model with $F_\pi = F_1^V$ provides a good description of the data for $W \gtrsim 2$

TABLE XI. The determination of the transverse-transverse interference term, B, for the k^2 scan. The cross sections are given for the region $2.4° \leq \theta \leq 4.8°$. For each data point, the first line gives the average of bins 9 and 15, the second line gives the average of bins 11 and 17, and the third line gives the average of bins 12 and 13 and 18 and 19 in addition to the nominal values to which the adjustments were made.

Data point	W (GeV)	k^2 (GeV^2)	ϵ	cosϕ	cos2ϕ	$\frac{d\sigma}{d\Omega_\pi}\left(\frac{\mu b}{sr}\right)$ Measured	Adjusted	$B\left(\frac{\mu b}{sr}\right)$
4	2.064	−0.189	0.880	0.961	0.850	10.81 ± 0.60	9.64 ± 0.54	
	2.244	−0.164	0.814	−0.954	0.826	2.74 ± 0.36	3.72 ± 0.49	
	2.150	−0.176	0.853	0.074	−0.800	8.97 ± 0.76		−1.47 ± 0.61
3b	2.076	−0.311	0.897	0.957	0.835	11.47 ± 0.73	10.52 ± 0.67	
	2.234	−0.282	0.854	−0.956	0.830	4.91 ± 0.52	6.19 ± 0.66	
	2.150	−0.294	0.880	0.032	−0.809	9.55 ± 0.74		−0.79 ± 0.61
7	2.081	−0.413	0.888	0.957	0.853	11.21 ± 0.57	10.45 ± 0.53	
	2.227	−0.376	0.847	−0.956	0.833	6.32 ± 0.44	7.59 ± 0.36	
	2.150	−0.396	0.870	0.040	−0.822	9.49 ± 0.56		−0.30 ± 0.47
9	2.091	−0.830	0.846	0.964	0.861	6.98 ± 0.53	7.05 ± 0.54	
	2.210	−0.763	0.812	−0.952	0.818	5.50 ± 0.48	5.65 ± 0.49	
	2.150	−0.795	0.830	0.020	−0.805	7.23 ± 0.64		−0.65 ± 0.54
12	2.096	−1.234	0.804	0.959	0.844	4.30 ± 0.46	4.50 ± 0.48	
	2.212	−1.142	0.768	−0.951	0.812	3.76 ± 0.44	3.66 ± 0.43	
	2.150	−1.188	0.788	0.057	−0.816	3.82 ± 0.52		0.20 ± 0.47

GeV and $-t \lesssim m_\pi^2$ (except for the one problem discussed for $W = 2.31$ GeV). In particular, it does quite well, especially compared to Born terms alone, in predicting the transverse-scalar interference term. For $-t \gtrsim m_\pi^2$, the model is still successful for $\phi = 0°$ data, but fails for $\phi = 180°$. These conclusions are not sensitive either to possible systematic errors in our data or to small adjustments of F_π in the model.

D. W Dependence

The measured and extrapolated cross sections for the central bins of the W scan are summarized in Table VIII. The cross sections were extrapolated to a fixed ϵ of 0.90 by multiplying the measured cross sections by the ratio of Berends' theory at $\epsilon = 0.90$ to Berends' theory at the ϵ of the measured cross sections. Most of the extrapolated cross sections are within 5% of the original measurements.

The extrapolated cross sections along with the predictions of Berends theory are displayed graphically in Fig. 26. Berends' theory was calculated assuming $F_\pi = F_1^V$. Forward π^+ photoproduction cross sections show resonance associated deviations from smoothness in the W range from 1.8 to 2.5 GeV. The measured electroproduction cross sections roughly follow the W dependence predicted by Berends. More data are necessary to determine if small resonance effects are present. Fixed-t dispersion-theory models predict that $W^2 d\sigma/d\Omega_\pi \to \text{const}$ as $W \to \infty$ for fixed k^2, ϵ, and t. In Berends' model for $-t > 0.015$ GeV^2 and $W = 2.5$ GeV, $W^2 d\sigma/d\Omega_\pi$ is within 7% of its infinite-energy limit.

E. k^2 Dependence

Table IX summarizes the k^2-scan cross sections for $\theta \leq 2.4°$. The cross sections were calculated by averaging over bins 1, 2, 4, 6, and 7. Table IX also summarizes the cross sections obtained by using Berends' model with $F_\pi = F_1^V$ to extrapolate to $\epsilon = 0.85$. Except for point 12 the adjustment was 2% or less and was not sensitive to the precise value of F_π used.

Since the five bins which were averaged do not have the same average kinematic variables, there is a second-order error made in combining them to obtain a central cross section. In order to

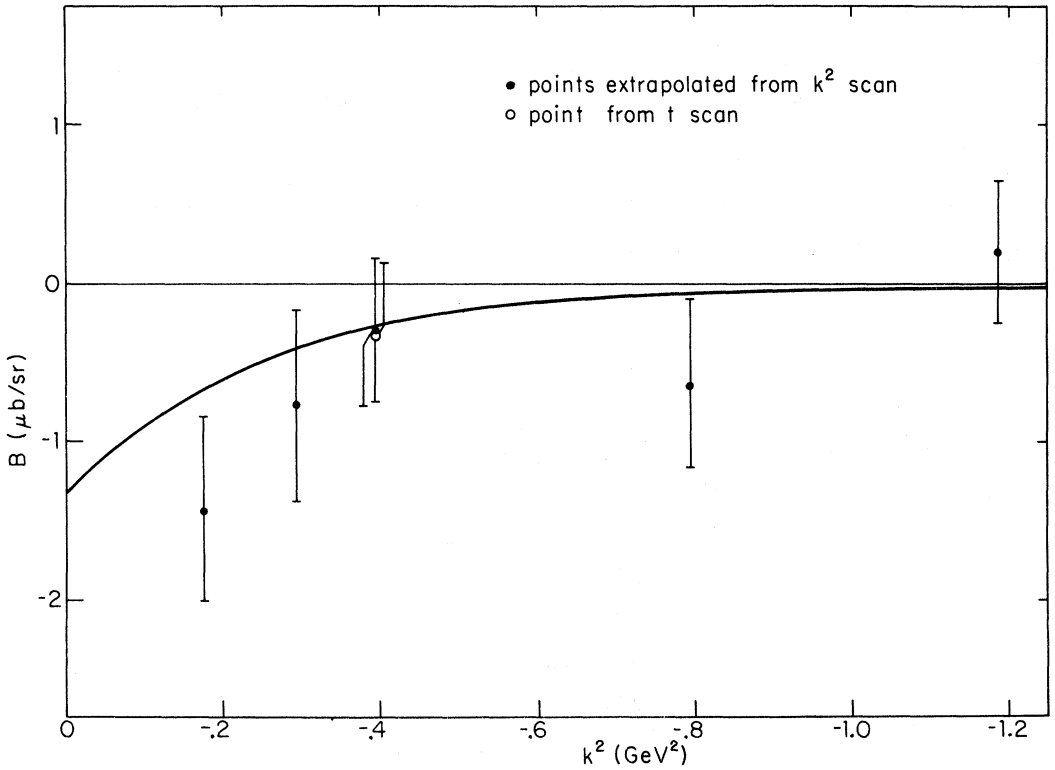

FIG. 29. The k^2 dependence of the transverse-transverse interference term B for $W = 2.15$ GeV and $2.4° \leq \theta \leq 4.8°$. Berends' theory with $F_\pi = F_1^V$ was used to extrapolate the measured cross sections to a common value of W and ϵ. The solid curve shows the prediction of Berends' theory with $F_\pi = F_1^V$. The uncertainties include the statistical errors only.

evaluate the size of this error, we compared the average of Berends' predictions for each bin with the integrated cross sections from $\theta = 0°$ to $\theta = 2.4°$ for the average kinematical variables of bin number 1. The difference was less than 0.5% in every case.

Figure 27 shows the forward-angle data together with the theoretical curves for three forms for F_π, G_E^p, F_1^V, and F_ρ, where

$$F_\rho = (1 - k^2/0.0585)^{-1}.$$

The cross section increases with $-k^2$ to a maximum near -0.4 GeV^2 and then decreases. This suggests a large scalar contribution since it is most plausible that the transverse component decreases with $-k^2$, while the scalar component must, at least initially, increase with $-k^2$. Figure 5 shows the predictions of Berends' model for the two components of the forward cross section with $F_\pi = F_1^V$. This form of the theory is in good agreement with the data.

In order to determine the transverse-transverse interference term B and the scalar-transverse interference term D, Berends' theory with $F_\pi = F_1^V$ was used to adjust the $2.4° \leq \theta \leq 4.8°$ data to central values of k^2, W, and ϵ. The procedure was to calculate the theory for each bin twice, once for the actual parameters and once for the central values of k^2, W, and ϵ, but for the actual values of $\langle\cos\phi\rangle$ and $\langle\cos 2\phi\rangle$. Then the ratio of the latter calculation to the former was multiplied by the measured cross section to obtain the adjusted cross section. Since the extrapolation is over small intervals it is not sensitive to the details of the model. The results of the adjustment are summarized in Tables X and XI.

Figure 28 shows the scalar-transverse interference term together with the predictions of Berends' theory with $F_\pi = F_1^V$. The theory agrees reasonably with the adjusted data. This gives evidence that the theoretical prediction for the relative proportion of transverse and scalar amplitudes is reasonable. The value of the minimum momentum transfer, $t_{\min}$, increases with $-k^2$ and the shape of the theoretical curve is a reflection of this variation. Thus the result that $D > 0$ for the small-angle k^2 scan may be related to the finding in the $W = 2.15$-GeV θ scan that $D < 0$ for $-t \leq 3m_\pi^2$.

Figure 29 shows the transverse-transverse interference term B. The extrapolations are of second order here since $\phi \approx 0°$ and $\phi \approx 180°$ bins are averaged. The major feature of B is that it is small, especially at large values of k^2. This is a model-independent indication of a large scalar component.

TABLE XII. Values for $F_\pi(k^2)$ derived from the $\theta \leq 2.4°$ data summarized in Table IX. Experimental statistical and systematic rms uncertainties are shown in the first and second sets of parentheses, respectively.

$-k^2$ (GeV)^2	$F_\pi(k^2)$
0.176	0.810 (0.044) (0.046)
0.294	0.641 (0.028) (0.026)
0.396	0.577 (0.016) (0.021)
0.795	0.400 (0.013) (0.012)
1.188	0.276 (0.014) (0.009)

F. Determination of the Pion Form Factor

We are justified in extracting the pion form factor from the data only if we have a model which describes correctly all aspects of the data. Berends' theory seems to satisfy this requirement. It agrees with the photoproduction data at $W = 2.15$ GeV. It predicts the smooth W dependence that is observed. It describes the angular distribution at $k^2 = -0.4$ (GeV)^2 for $-t \leq m_\pi^2$. It gives approximately the correct interference terms for the small-k^2 scan data. One serious problem is the inability of the theory to fit the angular distribution beyond $-t \approx m_\pi^2$, since $-t_{\min}$ for data points 9 and 12 is greater than m_π^2. The breakdown of the theory seen in the angular distribution could occur in such a way as to affect the small-angle k^2-scan predictions.

Table XII summarizes the model-dependent values of F_π that are derived from the forward-angle k^2-scan data. The form of Berends' theory used here assumes that the proton form factor is given by the dipole formula, and that the neutron electric form factor is zero for all k^2. The theory includes only the M_{1+}^3 multipole in the dispersion integrals. Figure 30 shows a plot of the pion form factor versus k^2. Also shown in Fig. 30 is the pion form factor obtained from an analysis by Berends and Gastmans[20] of the data of Driver *et al.*[17] and from an analysis by Devenish and Lyth[21] of the data of Sofair *et al.*[18,19] The solid lines in Fig. 30 correspond to F_ρ, F_1^V, and G_E^p.

Because of the magnitude of the over-all experimental and theoretical uncertainties, it is difficult to distinguish F_1^V from F_ρ. Moreover, finite-width corrections should be considered in constructing a ρ-dominated pion form factor.[48] It appears, however, that the charge form factor of the pion (F_π) is significantly larger than that of the proton (G_E^p).

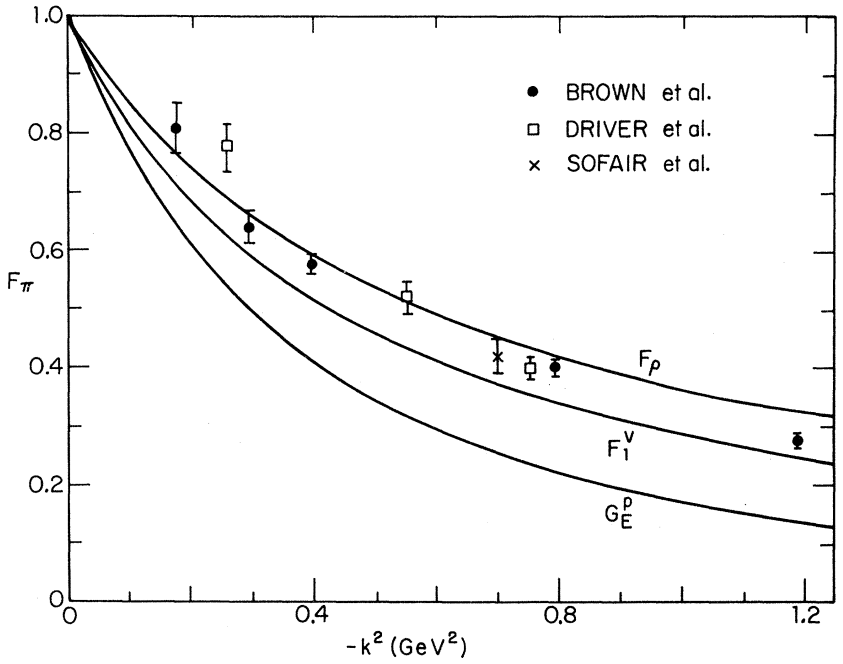

FIG. 30. The pion form factor determined using these data and Berends' theory. Also shown are the determinations from the measurements of Driver *et al.* and Sofair *et al.* The curve for F_1^V is taken from Ref. 20.

X. CONCLUSION

The near-forward data for the electroproduction reaction

$$e^- + p \rightarrow e^- + \pi^+ + n$$

show good agreement with a theory based on the generalized Born approximation corrected by using fixed-t dispersion relations. To this extent, the process is similar to the corresponding photoproduction reaction. As the photon mass squared $-k^2$ increases, the scalar term arising principally from one pion exchange becomes the dominant part of the cross section.

If one takes a specific model seriously, the measured cross sections can then be used to determine the pion form factor for spacelike k^2. Our forward k^2-scan data imply a form factor F_π consistent with either the isovector Dirac form factor F_1^V or the ρ form factor F_ρ. The principal uncertainties in the determination of F_π are due to the incompleteness of the dispersion-theory corrections, to the omission of any isoscalar contributions, and to the effect of the increase in the minimum momentum transfer as one goes to higher $-k^2$ for fixed W. There are also more subtle theoretical uncertainties arising from the use in the proposed dispersion models of the simplest possible pole term amplitudes consistent with gauge invariance and in the assumed behavior of the dispersion-theory subtraction constants.

More extensive electroproduction data for the higher nucleon resonances would reduce the uncertainties in the dispersion-theory corrections. Measurements of pion electroproduction at fixed large k^2 as a function of W would enable one to study the effect of the minimum momentum transfer on the extraction of F_π, and to determine the range of validity in W, t, and θ of a particular model. Corresponding cross sections for a deuterium target would allow one to correct for any small isoscalar contributions. A more precise theory could then be used with the extensive amount of data reported here to make an improved determination of the pion form factor.

ACKNOWLEDGMENTS

We gratefully acknowledge the support and cooperation of Professor Karl Strauch, the Director of the Cambridge Electron Accelerator, and the staff of the CEA laboratory. We are especially indebted to Dr. H. Winick, Dr. E. Patterson, Dr. R. Fessel, Dr. L. Law, Mr. M. Hoenig, Mr. A. Hansen, and Mr. D. Hay. We also wish to thank the Harvard Cyclotron Laboratory for their invaluable assistance. Here we are especially indebted to Mr. E. Sadowski, Mr. R. Burns, Mr. J. O'Kane, Mr. J. McElaney, Mr. A. Sansone, Mr. W. Sansone, Mr. R. Haggerty, and Mr. R. Wharton. We received invaluable theoretical assistance from Dr. F. Berends. Mr. D. Butler assisted with the data analysis.

*Research supported in part by the U. S. Atomic Energy Commission under Contract No. AT(11-1) 3064.

†This paper is based in part on theses submitted by three of the authors (A.M.E., G.J.F., and L.L.) to Harvard University in partial fulfillment of the requirements for the Doctor of Philosophy in Physics.

‡Present address: Center for Space Research, Massachusetts Institute of Technology, Cambridge, Massachusetts 02139.

§Present address: Physics Department, University of Michigan, Ann Arbor, Michigan 48104.

‖Present address: Physics Department, University of California, Santa Barbara, California 93106.

**Present address: Stanford Linear Accelerator Center, Stanford, California 94305.

††Present address: The Rockefeller University, New York, New York 10021.

‡‡Present address: Center for the Biology of Natural Systems, Washington University, St. Louis, Missouri 63130.

§§Present address: Genesee Valley Learning Center—Empire State College, State University of New York, Rochester, New York 14607.

[1]For a recent review of the SLAC-MIT data and references to the other publications see: H. Kendall, in *Proceedings of the 1971 International Symposium on Electron and Photon Interactions at High Energy,* edited by N. B. Mistry (Cornell Univ. Press, Ithaca, New York, 1972), p. 248.

[2]For interesting discussions of the implications of the SLAC-MIT data see articles by K. Wilson and J. Bjorken in *Proceedings of the 1971 International Symposium on Electron and Photon Interactions at High Energy,* edited by N. B. Mistry (Cornell Univ. Press, Ithaca, New York, 1972).

[3]For a summary of the present data on the individual electroproduction channels see K. Berkelman, in *Proceedings of the Sixteenth International Conference on High Energy Physics, National Accelerator Laboratory, Batavia, Ill., 1972,* edited by J. D. Jackson and A. Roberts (NAL, Batavia, Ill., 1973).

[4]W. R. Frazer, Phys. Rev. 115, 1763 (1959).

[5]H. Harari, in *Proceedings of the 1971 International Symposium on Electron and Photon Interactions at High Energy,* edited by N. B. Mistry (Cornell Univ. Press, Ithaca, New York, 1972), p. 300.

[6]K. Lübelsmeyer, in *Proceedings of the Fourth International Symposium on Electron and Photon Interactions at High Energy, 1969,* edited by B. W. Braben and R. E. Rand (Daresbury Nuclear Physics Laboratory, Daresbury, Lancashire, England, 1970), p. 45.

[7]R. Diebold, in *High Energy Physics,* edited by K.T. Mahanthappa, W. D. Walker, and W. E. Brittin (Colorado Associated Univ. Press, Boulder, 1970), p. 3.

[8]C. W. Akerlof, W. W. Ash, K. Berkelman, C. A. Lichtenstein, A. Ramanauskas, and R. H. Siemann, Phys. Rev. 163, 1482 (1967).

[9]C. Mistretta, J. A. Appel, R. J. Budnitz, L. Carroll, J. Chen, J. R. Dunning, Jr., M. Goitein, K. Hanson, D. C. Imrie, and R. Wilson, Phys. Rev. 184, 1487 (1969).

[10]S. Fubini, Y. Nambu, and V. Wataghin, Phys. Rev. 111, 329 (1958).

[11]R. Blankenbecler, S. Gartenhaus, R. Huft, and Y. Nambu, Nuovo Cimento 17, 775 (1960).

[12]P. Dennery, Phys. Rev. 124, 2000 (1961).

[13]N. Zagury, Phys. Rev. 145, 1112 (1966); 150, 1406(E) (1966).

[14]S. L. Adler, Ann. Phys. (N.Y.) 50, 189 (1968).

[15]C. N. Brown, C. R. Canizares, W. E. Cooper, A. M. Eisner, G. J. Feldman, C. A. Lichtenstein, L. Litt, W. Lockeretz, V. B. Montana, and F. M. Pipkin, Phys. Rev. Lett. 26, 987 (1971); 26, 991 (1971).

[16]Some of the material reported here is treated more extensively in the following theses submitted to Harvard University: A. M. Eisner, 1971 (unpublished); G. J. Feldman, 1971 (unpublished); L. Litt, 1971 (unpublished).

[17]C. Driver, K. Heinloth, K. Höhne, G. Hofmann, P. Karow, D. Schmidt, G. Specht, and J. Rathje, Phys. Lett. 35B, 77 (1971).

[18]P. S. Kummer, A. B. Clegg, F. Foster, G. Hughes, R. Siddle, J. Allison, B. Dickinson, E. Evangelides, M. Ibbotson, R. Lawson, R. S. Meaburn, H. E. Montgomery, W. J. Shuttleworth, and A. Sofair, Nuovo Cimento Lett. 1, 1026 (1971).

[19]A. Sofair, J. Allison, B. Dickinson, E. Evangelides, M. Ibbotson, R. Lawson, R. S. Meaburn, H. E. Montgomery, W. J. Shuttleworth, A. B. Clegg, F. Foster, G. Hughes, P. Kummer, and R. Siddle, Nucl. Phys. B42, 369 (1972).

[20]F. A. Berends and R. Gastmans, Phys. Rev. D 5, 204 (1972).

[21]R. C. E. Devenish and D. H. Lyth, Phys. Rev. D 5, 47 (1972); 6, 2067(E) (1972).

[22]W. Schmidt, DESY Report 71/22, 1971 (unpublished).

[23]For various treatment of the electroproduction kinematics see: J. K. Randolph, Harvard Cyclotron Memorandum (unpublished); C. W. Akerlof, W. W. Ash, K. Berkelman, and M. Tigner, Phys. Rev. Lett. 14, 1036 (1965); H. F. Jones, Nuovo Cimento 40A, 1018 (1965); N. Dombey, Rev. Mod. Phys. 41, 236 (1969), and also Ref. 8.

[24]For a convenient summary of the notation used by different groups see Ref. 21.

[25]We adapt a normalization convention introduced by L. N. Hand, Phys. Rev. 129, 1834 (1963).

[26]C. N. Brown, C. R. Canizares, W. E. Cooper, A. M. Eisner, G. J. Feldman, C. A. Lichtenstein, L. Litt, W. Lockeretz, V. B. Montana, and F. M. Pipkin, Phys. Rev. Lett. 27, 536 (1971).

[27]The π^0 production is treated in C. N. Brown, C. R. Canizares, W. E. Cooper, A. M. Eisner, G. J. Feldman, C. A. Lichtenstein, L. Litt, W. Lockeretz, V. B. Montana, and F. M. Pipkin, Phys. Rev. Lett. 27, 1611 (1971).

[28]The K^+ production is treated in C. N. Brown, C. R. Canizares, W. E. Cooper, A. M. Eisner, G. J. Feldman, C. A. Lichtenstein, L. Litt, W. Lockeretz, V. B. Montana, F. M. Pipkin, and N. Hicks, Phys. Rev. Lett. 28, 1086 (1972).

[29]Some material related to that reported here is described in the following theses submitted to Harvard University: C. R. Canizares, 1971 (unpublished); W. Lockeretz, 1971 (unpublished); V. B. Montana, 1971 (unpublished).

[30]J. Engels, G. Schwiderski, and W. Schmidt, Phys. Rev. 166, 1343 (1968).

[31]J. D. Jackson and C. Quigg, Phys. Lett. 29B, 236 (1969); 33B, 444(E) (1970); Nucl. Phys. B22, 301 (1970).

[32]F. A. Berends, Phys. Rev. D 1, 2590 (1970).

[33]R. Manweiler and W. Schmidt, Phys. Rev. D 3, 2752 (1971); Phys. Lett. 33B, 366 (1970).

[34]F. A. Berends and G. B. West, Phys. Rev. 188, 2538 (1969).

[35]G. Buschhorn, J. Carroll, R. D. Eandi, P. Heide, R. Hübner, W. Kern, V. Kötz, P. Schmüser, and H. J. Skronn, Phys. Rev. Lett. 17, 1027 (1966); 18, 571 (1967).

[36]F_1^V is the isovector Dirac nucleon form factor. In all evaluations of the Born terms and of Berends' model, we have assumed scaling and the usual dipole form: $G_E^p = G_M^p/\mu_p = G_M^n/\mu_n = (1-k^2/0.71)^{-2}$ and $G_E^n = 0$. This implies that $F_1^V = [1 - 3.7k^2/(4M^2 - k^2)]\, G_E^p$. These forms deviate from electron scattering results by up to 3% in our region of k^2.

[37]The use of Zagury's multipoles (Ref. 13) were implemented by F. A. Berends.

[38]B. H. Kellett and C. Verzegnassi, Nuovo Cimento 13A, 195 (1973).

[39]N. Dombey and B. J. Read, DESY Report 72/44, 1972 (unpublished).

[40]See: *The Cambridge Electron Accelerator: A Comprehensive Account,* CEA Report 1000, edited by W. A. Shurcliff (Cambridge Electron Accelerator, Cambridge, Mass., 1964).

[41]E. R. Hayes, R. A. Schluter, and A. Tamositis, Argonne National Laboratory Report No. ANL-6916, 1964 (unpublished).

[42]W. Traub, private communication.

[43]Refractive Index of Freon Compounds, Technical Bulletin B-32 (E. I. DuPont de Nemours and Company, Wilmington, Delaware).

[44]L. W. Mo and Y. S. Tsai, Rev. Mod. Phys. 41, 205 (1969). Generally the multiple-photon corrections neglected here must be included. See, for example, M. Breidenbach, Thesis, 1970 (MIT Report No. MIT-2098-635) (unpublished) and G. Miller, Thesis, 1971 (SLAC Report No. 129) (unpublished).

[45]Ch. Berger, V. Burkert, G. Knop, B. Langenbeck, and K. Rith, Phys. Lett. 35B, 87 (1971).

[46]N. Meister and D. R. Yennie, Phys. Rev. 130, 1210 (1963).

[47]A. Bartl and P. Urban, Acta. Phys. Austriaca 24, 139 (1966). See also P. Urban, *Topics in Applied Quantum Electrodynamics* (Springer-Verlag, New York, 1970), which corrects some misprints of this paper. The vertex and vacuum polarization corrections contribute a constant term $-\frac{28}{9}$, not $-\frac{46}{9}$. We are grateful to A. Bartl and F. Widder for communications concerning these calculations.

[48]See, M. Roos and J. Pišút, Nucl. Phys. B10, 563 (1969), and references therein. P. Curry and J. W. Moffat [Phys. Rev. 184, 1885 (1969)] have concluded that $F_\pi = F_1^V$ is consistent with the ρ dominance of F_π.